

UNIVERSIDADE DE LISBOA
FACULDADE DE CIÊNCIAS
DEPARTAMENTO DE FÍSICA



**Optimization of the diffusion-weighted MRI processing pipeline
for the longitudinal assessment of the brain microstructure in a
rat model of Alzheimer's disease**

Catarina Sofia Tristão Pereira

Mestrado Integrado em Engenharia Biomédica e Biofísica
Perfil em Radiações em Diagnóstico e Terapia

Dissertação orientada por:

Alexandre Andrade, PhD, Faculdade de Ciências da Universidade de Lisboa, Portugal
Ileana Jelescu, PhD, Centre d'Imagerie Biomédicale, École Polytechnique Fédérale de
Lausanne, Switzerland

Acknowledgements

Over the 10 months of this traineeship I could not be more thankful to Dr. Ileana Jelescu for hosting me at the Centre d'Imagerie Biomédicale (CIBM), École Polytechnique Fédérale de Lausanne (EPFL) in Switzerland. Her constant academic guidance and attention were such an inspiration for me and I will always remember that with profound gratitude. A special thank you to Yujian Diao for his company during scans and for his support in this project, and to Analina Silva, Stefan Mitrea and Mario Lepore for assistance with animal setup and monitoring.

I am extremely grateful to everyone at CIBM from whom I learned constantly and for creating such a welcoming and pleasant work environment. Thank you to Professor Rolf Gruetter for allowing me to have this amazing experience full of incredible opportunities, including attending the OHBM Annual Meeting 2019 in Rome, Italy. To all the friendships that came along with this experience, I thank you for making this year abroad even more special, in particular Jérémie Clément, Alice Radaelli, Thanh Phong Lê and Anne-Marie Clérc.

This work was supported by EPFL, the University of Lausanne (UNIL), the University of Geneva (UniGe), the Centre Hospitalier Universitaire Vaudois (CHUV), the Hôpitaux Universitaires de Genève (HUG) and the Leenaards and the Jeantet Foundations. The support of the Swiss-European Mobility Plan (Movetia) was crucial for funding my stay in Switzerland.

I would like to thank you to my internal supervisor Dr. Alexandre Andrade for all the guidance during the traineeship as well as throughout the last 5 years of the integrated BSc/MSc in Biomedical Engineering and Biophysics in Faculdade de Ciências da Universidade de Lisboa (FCUL). I greatly appreciated the academic preparation provided by the University of Lisbon, FCUL and the Institute of Biomedical Engineering and Biophysics (IBEB) that promotes knowledge exchange among students, maintains partnerships with institutions within the different areas of biomedicine and physics and encourages students to take up early professional experiences.

Lastly, I am thankful to my friends and family who in different ways have helped me engaging in this journey. A warm thank you to those with whom I have shared the most treasured moments in the past 5 years of college. Marta Marques and André Diogo thank you for your unconditional support, for studying together and going to London, and more importantly for the strong relationship we have built over both happy and stressful moments. We will certainly nourish our friendship from wherever we are. Thank you to one of my oldest friends Mariana Afonso for her advice and craziness, and to Frederico Roldão for making it all easier. I cannot thank you enough to my parents who provided the means to make this traineeship possible, for always being by my side and for all the patience and encouragement along the years.

This year in Switzerland was not always easy, but in the end it was the best experience I could have asked for both academically and personally. It was successful and prepared me for my future career and it would not have been possible without all the support and kindness.

Abstract

The mechanism that triggers Alzheimer’s disease (AD) is not well-established, with amyloid plaques, neurofibrillary tangles of tau protein, microgliosis and glucose hypometabolism all likely involved in the early cascade. One main advantage of animal models is the possibility to tease out the impact of each insult on the neurodegeneration. Following an intracerebroventricular (icv) injection of streptozotocin (STZ), rats and monkeys develop impaired brain glucose metabolism, i.e. “diabetes of the brain”. Numerous studies have reported AD-like features in icv-STZ animals, but this model has never been characterized in terms of Magnetic Resonance Imaging (MRI)-derived biomarkers beyond structural brain atrophy. White matter degeneration has been proposed as a promising biomarker for AD that well precedes cortical atrophy and correlates strongly with disease severity. Therefore, this project proposes a longitudinal study of white matter degeneration in icv-STZ rats using diffusion MRI. An existing image processing pipeline was primarily used to obtain preliminary results and propose an optimization strategy to improve it in terms of data quality and reliability. These strategies were tested and implemented in the pipeline when confirmed to be valuable, in order to achieve results as reproducible as possible and find the spatio-temporal pattern of brain degeneration in this animal model.

All experiments were approved by the local Service for Veterinary Affairs. Male Wistar rats (N=18) (236 ± 11 g) underwent a bilateral icv-injection of either streptozotocin (3 mg/kg, STZ group, N=10) or buffer (control group, CTL, N=8). Rats were scanned at four timepoints following surgery on a 14 T Varian system. Diffusion data were acquired using a semi-adiabatic SE-EPI PGSE sequence as follows: 4 ($b=0$ ms/ μm^2), 12 ($b=0.8$ ms/ μm^2), 16 ($b=1.3$ ms/ μm^2) and 30 ($b=2$ ms/ μm^2) directions; TE/TR=48/2500 ms, 9 coronal 1 mm slices, $\delta/\Delta=4/27$ ms, FOV=23x17 mm², matrix=128x64 and 4 shots.

The existing image processing pipeline included image denoising and eddy-correction. Moreover, diffusion and kurtosis tensors were calculated for each voxel, producing parametric maps of fractional anisotropy (FA), mean, axial and radial diffusivity (MD, AxD and RD) and mean, axial and radial kurtosis (MK, AK and RK). Additionally, the two-compartment WMTI-Watson model was further estimated to provide specificity to the microstructure assessment. The following metrics were derived from the model: volume water fraction f , parallel intra-axonal diffusivity D_a , parallel $D_{e,\parallel}$ and perpendicular extra-axonal diffusivities $D_{e,\perp}$ and dispersion of fiber orientations c_2 . Since the model allows for two mathematical solutions, the $D_a > D_{e,\parallel}$ solution was retained based on recent evidence. Considering previous findings, the corpus callosum, cingulum, fornix and fimbria were chosen as white matter regions of interest (ROIs) and automatically segmented using anatomical atlas-based registration. Mean diffusion metrics were calculated in each ROI for each dataset. CTL and STZ groups were compared using two-sided t -tests at each timepoint. Within-group longitudinal changes were assessed using one-way ANOVA. Because of the small cohort, statistical analysis excluded the last time point.

In the course of this project, strategies to optimize the existing pipeline were developed and tested. The existing brain atlas template was supplemented with white matter labels, rat brain extraction was semi-automated, and bias field correction of anatomical data was added before registration. Ventricle enlargement is typically reported in icv-STZ animals and normally constitutes an issue of misalignment in registration. In order to better match the label ROIs with the respective underlying tissue, several registration procedures were tested with different FA and color-coded FA template images. Color-coded FA-based registration dramatically improved the segmentation of the corpus callosum and the fimbria and reliability of diffusion metrics extracted from these regions. Moreover, additional fiber metrics were extracted from a newly developed tractography pipeline to compare with tensors metrics and finally, tensors metrics were evaluated in the gray matter for a more comprehensive spatio-temporal characterization of brain degeneration.

Results from statistical analysis were obtained after implementing the successful optimization strategies into the pipeline. There were few significant differences within groups over time. However, between-group differences at each time point were more pronounced. White matter microstructure alterations were consistent with previous studies of histology and cognitive performance of the icv-STZ model. Changes in tensors metrics indicate early axonal injury in the fimbria and fornix at 2 weeks after injection, a period of potential recovery at 6 weeks after injection and late axonal injury at 13 weeks in all ROIs. The WMTI-Watson biophysical model provided specificity to the underlying microstructure, by showing intra-axonal damage in the fimbria and corpus callosum as early as 2 weeks, followed by a recover period and definite axonal loss at 13 weeks after injection.

Results from tensors metrics and the WMTI-Watson model are not only complementary, they are consistent with each other and with previously-established trends for structural thickness, memory performance, amyloid deposition and inflammation. The icv-STZ model displays white matter changes in tracts reportedly affected by AD, while the degeneration is induced primarily by impaired brain glucose metabolism. The icv-STZ constitutes an excellent model to reproduce sporadic AD and should allow to further explore the hypothesis of AD being “type III diabetes”. The combination of diffusion information extracted from tensor imaging and biophysical modelling is a promising set of tools to assess white matter in the AD brain and might be the upcoming strategy to assess the human brain. Regarding future work, it will focus on estimating the correlation between microstructural alterations and functional connectivity (from resting-state functional MRI), glucose hypometabolism (from FDG-PET), and pathological features (from histological stainings) – all currently under processing at CIBM. Tractography is a cutting-edge methodology to assess brain connectivity and the pipeline created could be further developed to improve understanding and support diffusion metrics. The relationship between white and gray matter will also improve the understanding of spatio-temporal degeneration and the progression nature of the disease.

Keywords: Alzheimer’s disease, animal models, white matter microstructure, diffusion tensors and biophysical models of diffusion

Resumo

O mecanismo que desencadeia a doença de Alzheimer (DA) não é bem conhecido, contudo sabe-se que a presença de placas amilóides e de emaranhados neurofibrilares da proteína tau, microgliose e ainda hipometabolismo de glucose estão envolvidos na fase inicial da cascata de desenvolvimento da doença. A principal vantagem dos modelos animais é justamente a possibilidade de estudar individualmente o impacto de cada um destes mecanismos no processo de neurodegeneração. Após uma injeção intracerebroventricular (icv) de estreptozotocina (STZ), várias espécies de animais mostraram um metabolismo anormal de glucose no cérebro, processo que foi referido como “diabetes do cérebro”. Vários estudos demonstraram que animais icv-STZ são portadores de características típicas de DA, mas este modelo animal nunca foi estudado em termos de biomarcadores derivados de técnicas de imagem por ressonância magnética (IRM), exceto atrofia estrutural do cérebro. Um biomarcador promissor de DA que se acredita preceder a atrofia do córtex cerebral é a degeneração da matéria branca do cérebro, uma vez que foi fortemente correlacionado com a progressão e gravidade da doença. Logo, este projeto propõe um estudo longitudinal da degeneração da matéria branca em ratas icv-STZ utilizando IRM de difusão. O plano de processamento de imagem existente foi utilizado primeiramente para obter resultados preliminares e viabilizar a proposta de estratégias de otimização da mesma, em termos de melhoramento da qualidade de imagem e credibilidade das variáveis extraídas das imagens resultantes. Estas estratégias foram testadas e implementadas no plano de processamento quando a sua performance confirmou ser de valor, para que os resultados fossem o mais reproduzíveis possível em caracterizar a distribuição espaço-temporal da degeneração do cérebro neste modelo animal.

Todos os procedimentos aqui descritos foram aprovados pelo serviço local dos assuntos veterinários. Ratas macho Wistar (N=18, 236±11 g) foram submetidas a uma injeção icv de STZ (3 mg/kg) no caso do grupo infetado (N=10) ou de um *buffer* no caso do grupo de controlo (N=8). As ratas foram examinadas no *scanner* de IRM do tipo *Varian* de 14 T em quatro momentos no tempo: 2, 6, 13 e 21 semanas após a injeção. As imagens por difusão foram adquiridas com uma sequência semi-adiabática *spin-echo* EPI PGSE com os seguintes parâmetros: 4 (b=0), 12 (b=0.8 ms/μm²), 16 (b=1.3 ms/μm²) and 30 (b=2 ms/μm²) direções; TE/TR=48/2500 ms, 9 secções coronais de 1 mm, δ/Δ=4/27 ms, FOV=23x17 mm², matriz=128x64 e 4 *shots*.

O plano existente de processamento de imagem incluía a correção das imagens ao nível de ruído e correntes-*eddy*. Posteriormente, os tensores de difusão e curtose foram estimados para cada voxel e os mapas paramétricos de anisotropia fracional (FA), difusão média, axial e radial (MD, AD e RD) e curtose média, axial e radial (MK, AK e RK) foram calculados. Adicionalmente, um modelo de difusão de água nas fibras da matéria branca foi utilizado para providenciar maior especificidade ao estudo da microestrutura do cérebro. Como tal, o modelo de dois compartimentos denominado WMTI-Watson foi também estimado e as seguintes variáveis foram derivadas do mesmo: a fração do volume de água f , a difusividade paralela intra-axonal D_a , as difusividades paralela $D_{e,\parallel}$ e perpendicular $D_{e,\perp}$ extra-axonais e, finalmente, a orientação da dispersão axonal c_2 . Este modelo matemático tem duas soluções possíveis dada a sua natureza quadrática, pelo que a solução $D_a > D_{e,\parallel}$ foi imposta com base em evidências recentes. Considerando estudos anteriores, as regiões de interesse (RDIs) da matéria branca escolhidas para analisar a microestrutura cerebral foram o corpo caloso, o cíngulo, a fimbria e a fórnix. Estes foram automaticamente segmentados através de registo de imagem de um atlas das regiões do cérebro da ratas e as médias das medidas extraídas dos tensores de difusão e curtose e ainda do modelo biofísico neuronal foram calculadas em cada RDI para cada conjunto de imagens obtidas. Os dois grupos de teste e controlo foram comparados usando testes t de Student bilaterais em cada momento do tempo, e a comparação das alterações longitudinais em cada grupo foi feita usando uma ANOVA. Devido ao baixo número de amostras, o último momento no tempo às 21 semanas foi excluído da análise.

No decorrer deste projeto, várias estratégias para otimizar o processamento de imagem ou complementar a análise da informação disponível foram testadas. Nomeadamente, o atlas cerebral da ratazana foi aperfeiçoado relativamente às regiões de matéria branca, a segmentação do cérebro foi testada com algoritmos automáticos e a correção do *bias field* em imagens estruturais de IRM foi adicionada ao plano antes do registo de imagem. O aumento dos ventrículos cerebrais é uma característica frequente em animais icv-STZ, constituindo um problema de alinhamento nos métodos de registo de imagem. No sentido de otimizar a correspondência entre as regiões do atlas e as respetivas regiões na imagem estrutural e por difusão, vários procedimentos de registo de imagem foram testados. O co-registo de imagem convencional utiliza imagens estruturais para normalizar o espaço das imagens por difusão, no entanto os mapas paramétricos de FA têm vindo a substituir este conceito dado o excelente contraste que providenciam entre a matéria branca e cinzenta do cérebro. Mapas de FA com diferentes direções predominantes mostraram uma melhoria significativa da segmentação do corpo caloso e da fimbria e também do poder estatístico das variáveis extraídas destas RDIs. Adicionalmente, um novo plano de processamento de tratografia foi construído de raiz no âmbito deste projeto para extrair variáveis adicionais das fibras de interesse e compará-las com as variáveis de difusão obtidas por análise voxel-a-voxel. Por último, as variáveis calculadas através dos tensores de difusão e curtose foram avaliadas na matéria cinzenta do cérebro para uma caracterização espaço-temporal da degeneração cerebral na DA.

Os resultados da análise estatística foram obtidos após integrar no plano de processamento as estratégias que mostraram valorizar o projeto em termos de qualidade de imagem ou credibilidade das variáveis. Houve poucas diferenças significativas ao longo do tempo em cada grupo, no entanto as diferenças entre grupos foram bastante acentuadas. As alterações ao nível da microestrutura da matéria branca foram consistentes com estudos prévios em animais icv-STZ usando métodos histológicos e avaliações das suas capacidades cognitivas. Alterações nas variáveis extraídas dos tensores indicaram deficiência axonal inicial na fimbria e no fórnix 2 semanas após injeção no grupo de teste, um potencial período de recuperação às 6 semanas e novamente deficiência axonal às 13 semanas, sendo que neste período tardio todas as RDIs foram afetadas. O modelo biofísico WMTI-Watson confirmou aumentar especificidade ao estudo da microestrutura, visto que demonstrou danos intra-axonais na fimbria e no corpo caloso 2 semanas após injeção, seguidos de um período de recuperação e de perda de estrutura axonal definitiva às 13 semanas em todas as RDIs.

Não só estes dois métodos de análise de IRM de difusão se complementam, como são também consistentes entre eles e com as tendências de alterações ao longo do tempo descritas noutros estudos. Além disso, o animal icv-STZ mostrou alterações características da DA, mesmo tendo a degeneração cerebral sido induzida pela disrupção do metabolismo de glucose no cérebro. Como tal, este modelo animal é excelente para reproduzir a doença e deverá continuar a ser avaliado nas diferentes áreas multidisciplinares para explorar a hipótese de a DA ser desencadeada pela falha do sistema insulina/glucose. A combinação da informação de difusão obtida dos tensores e da modelação da difusão neuronal provou ser uma ferramenta promissora no estudo das fibras da matéria branca do cérebro e poderá vir a ser o desafio futuro no que toca a investigação clínica da DA. Este estudo focar-se-á em correlacionar as alterações microestruturais aqui descritas com dados de conectividade funcional (obtida por IRM funcional em repouso), hipometabolismo de glucose (por FDG-PET) e outras características patológicas (por coloração histológica) – todos já em curso no CIBM. Tratografia é a metodologia topo de gama para aceder à conectividade cerebral e o plano de processamento gerado neste projeto poderá continuar a ser desenvolvido no futuro para informação adicional, assim como a relação entre a matéria branca e cinzenta poderá suplementar a compreensão da progressão da doença no espaço e no tempo.

Palavras-chave: Doença de Alzheimer, modelos animais, microestrutura da matéria branca cerebral, tensores de difusão, modelos biofísicos de difusão.

Table of Contents

Acknowledgements	iii
Abstract	iv
Resumo.....	vi
Table of Contents	viii
List of Figures	x
List of Tables.....	xiii
List of Abbreviations and Notations	xiv
1. Introduction	1
2. Theoretical Background	3
2.1. Alzheimer’s disease	3
2.1.1. Pathological cascade of AD.....	3
2.1.2. Etiopathology of AD	4
2.1.3. Animal models of AD	6
2.1.4. Relevant rat brain anatomy.....	6
2.2. Magnetic Resonance Imaging principles	8
2.2.1. Alignment and precession of magnetic moments	8
2.2.2. Resonance phenomenon	9
2.2.3. Pulse sequence parameters and image contrast	10
2.2.4. Signal acquisition and image reconstruction	11
2.3. Assessing microstructure with diffusion-weighted imaging.....	13
2.3.1. Biological diffusion principles	13
2.3.2. Diffusion-weighted imaging and signal representation	14
2.3.3. DWI data assessment using tensor-derived metrics	16
2.3.4. Biophysical modelling of DWI data	17
2.3.5. Tractography	20
2.4. DWI image processing.....	22
2.4.1. General image noise correction	22
2.4.2. Image correction in EPI acquisition	22
2.4.3. Bias field correction	23
2.4.4. Image registration.....	23
3. Methods.....	24
3.1. Study design.....	24
3.2. MRI data acquisition.....	24
3.3. Existing image processing pipeline	26
3.3.1. Data reconstruction and brain extraction.....	26
3.3.2. dMRI data correction.....	27

3.3.3.	Spatial normalization of anatomical MRI data for co-registration	28
3.3.4.	dMRI data registration and segmentation.....	28
3.3.5.	Diffusion and kurtosis tensors estimation.....	30
3.3.6.	Estimation of the WMTI-Watson biophysical model of the white matter.....	31
3.4.	Optimization strategies to the existing pipeline.....	32
3.4.1.	Improvement of white matter labels in the template atlas	32
3.4.2.	Semi-automatic brain extraction.....	32
3.4.3.	Bias field correction	33
3.4.4.	FA atlas-based registration of dMRI data.....	33
3.4.5.	Evaluation of the initial values in the WMTI-Watson model.....	35
3.5.	Statistical analysis of diffusion metrics	36
3.6.	Additional diffusion analysis strategies	37
3.6.1.	Gray matter analysis for correlation with white matter metrics	37
3.6.2.	Tractography for quality assessment of metrics	38
4.	Results	41
4.1.	Optimization strategies to the existing pipeline.....	41
4.1.1.	Improvement of white matter labels in the template atlas	41
4.1.2.	Semi-automatic brain extraction.....	42
4.1.3.	Bias field correction	44
4.1.4.	FA atlas-based registration of dMRI data.....	44
4.1.5.	Evaluation of the initial values in the WMTI-Watson model.....	47
4.2.	Statistical analysis of diffusion metrics using the optimized pipeline	49
4.2.1.	Tensor-derived metrics results.....	49
4.2.2.	WMTI-Watson model metrics results	50
4.3.	Additional diffusion analysis strategies	51
4.3.1.	Gray matter analysis for correlation with white matter metrics	52
4.3.2.	Tractography for quality assessment of metrics	53
5.	Discussion	55
5.1.	White matter microstructural patterns	55
5.2.	Consistency with previous studies	56
5.3.	Optimization strategies	57
6.	Conclusion	58
7.	References.....	59
8.	Appendices.....	65
8.1.	Appendix A.....	65
8.2.	Appendix B.....	72

List of Figures

<i>Figure 2.1: Pathological cascade of AD adapted from Jack et al, 2013 [24]. Evolution of biomarkers over disease progression, where white matter degeneration might have a key role. MCI: mild cognitive impairment.</i>	<i>4</i>
<i>Figure 2.2: The role of insulin in the cellular membrane. PI-3K and PKB/Akt: signalling pathways. GLUT4: glucose transporter [51]......</i>	<i>5</i>
<i>Figure 2.3: Anatomy of the rat brain from the Allen Brain Atlas in a coronal plane. Regions in purple correspond to white matter tracts.</i>	<i>7</i>
<i>Figure 2.4: Alignment of nuclear spins with no external field applied (on the left) and in the presence of \mathbf{B}_0 (on the right) [61]. NMV: net magnetization vector.</i>	<i>8</i>
<i>Figure 2.5: Precessional movement of the net macroscopic magnetic moment induced by \mathbf{B}_0 [61].</i>	<i>9</i>
<i>Figure 2.6: The net magnetization vector (NMV) is completely transferred from the longitudinal to the transverse plane after a 90° RF pulse as a resonance result [61].</i>	<i>9</i>
<i>Figure 2.7: Difference of image contrast between fat tissue and water as a function of time parameters in a T2-weighted image [61].</i>	<i>10</i>
<i>Figure 2.8: Spin-echo (A) and gradient-echo pulse sequences (B).</i>	<i>11</i>
<i>Figure 2.9: At each TR, echoes are stored in the frequency and phase encoded k-space to produce an image by applying a Fourier transform [63].</i>	<i>12</i>
<i>Figure 2.10: A fibrous tissue is an anisotropic medium and can be represented by an ellipsoid with one of the eigenvalue magnitudes greater than the others.</i>	<i>14</i>
<i>Figure 2.12: Directional sampling in increasing directions [67].</i>	<i>15</i>
<i>Figure 2.13: Two-compartment WMTI model providing five parameters [16].</i>	<i>18</i>
<i>Figure 2.14: Deterministic tractography methods. A) discretized “connect-the-voxels”. B) continuous FACT. C) non-linear method [83].</i>	<i>20</i>
<i>Figure 2.15: Fiber populations within a voxel with orientations (θ_1, ϕ_1) and (θ_2, ϕ_2). The measured signal can be obtained by the convolution between the response functionl and the fiber ODF [88].</i>	<i>21</i>
<i>Figure 3.1: Experimental timeline of the longitudinal study.</i>	<i>24</i>
<i>Figure 3.2: Experimental setup for the MRI scan. A) rat holder. B) capacitors for adjustment of frequency by tuning and matching procedure. C) superficial rat head coil. D) water tubes for body temperature adjustment. E) sedation injection. F) anal thermometer. G) breathing sensor.</i>	<i>25</i>
<i>Figure 3.3: Plot of the b-values acquired in a total of 62 directions in one of the repetitions.</i>	<i>25</i>
<i>Figure 3.4: Reconstructed MRI images in each modality (column) in two coronal planes (rows).</i>	<i>26</i>
<i>Figure 3.5: Manually drawn masks of the brain and resulting extracted brains in anatomical and diffusion data in two coronal planes (rows).</i>	<i>27</i>
<i>Figure 3.6: Sequential steps of diffusion data correction in two coronal planes (rows).</i>	<i>27</i>
<i>Figure 3.7: WHS template space where anatomical data were registered to.</i>	<i>28</i>
<i>Figure 3.8: Schematic representation of the registration procedure. Anatomical data in A) was registered into the template image B) so that the deformation field from the template space to the original anatomical space could be calculated. Diffusion data in D) and anatomical data in A) were co-registered so that the deformation field from</i>	

<i>the anatomical space to the diffusion space could be calculated. Finally, the transformations from the template space to the anatomical space and from this to the diffusion space were convoluted in order to calculate the transformation of the atlas in the template space C) to the diffusion space and obtain an atlas E) for each diffusion dataset.</i>	29
<i>Figure 3.9: White matter ROIs in different coronal planes (columns). In A) ROIs are represented as binary labels and B) is the original diffusion data where labels are overlapped.</i>	29
<i>Figure 3.10: Parametric maps of DTI and DKI quantitative metrics.</i>	30
<i>Figure 3.11: Parametric maps of parameters resulting from the WMTI-Watson model in two coronal planes (rows).</i>	31
<i>Figure 3.12: Parametric maps of f before (A) and after the filter F_{WMTI} is applied (B) in two coronal planes (rows).</i>	31
<i>Figure 3.13: Comparison between STZ (A) and CTL (B) rat brain ventricles at 13 weeks after injection in different coronal planes (columns).</i>	34
<i>Figure 3.14: Different parametric maps (columns) obtained from the pipeline (upper row) and the respective images available in WHS template space (lower row).</i>	34
<i>Figure 3.15: “Fitting” (upper row) and “unfitting” voxels (lower row) capturing the corpus callosum in three different representations (columns): corrected diffusion image (A and D), FA parametric maps (B and E) and f parametric maps (C and F).</i>	36
<i>Figure 3.16: Updated experimental timeline with the datasets included in statistical tests. Due to poor data quality or health reasons, some rat brains could not be included in all time points.</i>	36
<i>Figure 3.17: Gray matter ROIs in two coronal planes.</i>	37
<i>Figure 3.18: FOD dataset represented with arrows that characterize the fiber orientation. Orientation is defined by arrow color and FOD magnitude by arrow size.</i>	39
<i>Figure 3.19: Registration of FOD datasets (A) to a template generated from original data (B). In C) the FOD datasets was transformed into the generated template space.</i>	39
<i>Figure 4.1: Differences between the initial and improved template atlas with particular focus on the white matter regions in two coronal planes (rows). Red arrows and blue circles highlight the main differences between both.</i>	41
<i>Figure 4.2: Comparison between two different tools (columns) for brain extraction before (upper row) and after (lower row) intensity correction of anatomical data. The red arrow and blue circle represent the advantages of the corresponding tool.</i>	42
<i>Figure 4.3: Comparison between different parameters for the brain extraction in diffusion data. The circles represent the main differences between parameters.</i>	43
<i>Figure 4.4: Comparison between manual extraction and the 3dAutomask tool with $thr=0.65$ and 3 dilations in the corrected diffusion signal (upper row) and the MK parametric map (lower row) in the corpus callosum.</i>	43
<i>Figure 4.5: Difference between the original anatomical image and after bias field correction in two coronal planes (rows).</i>	44
<i>Figure 4.6: Comparison between the ROIs extracted from atlases resulting from different registration procedures (columns) in a STZ dataset in three coronal planes (rows).</i>	45
<i>Figure 4.7: Comparison between the ROIs (rows) extracted from atlases resulting from linear and non-linear registration (columns) of the method selected in the first stage in a STZ dataset.</i>	46

<i>Figure 4.8: Histograms of each WMTI-Watson model parameter (columns) in two different voxels (rows) with 3750 combinations of initial values. The window of each parameter comprises parameter values considered to be biophysically reasonable.</i>	48
<i>Figure 4.9: Boxplots of DTI and DKI derived metrics. Significant differences between study groups at each time point are shown in red and within groups over time in green. *: $p<0.05$, **: $p<0.01$ and ***: $p<0.001$.</i>	49
<i>Figure 4.10: Boxplots of WMTI-Watson model parameters. Significant differences between study groups at each time point are shown in red and within groups over time in green. *: $p<0.05$, **: $p<0.01$ and ***: $p<0.001$.</i>	50
<i>Figure 4.11: Boxplots of WMTI-Watson model parameters. Significant differences between study groups at each time point are shown in red and within groups over time in green. *: $p<0.05$.</i>	51
<i>Figure 4.12: Scatter plots of the relationship between degeneration in the white matter and gray matter. This analysis was carried out across groups (upper row) and over time (lower row) between regions known to be relevant to AD and anatomically connected. CG: cingulum, CC: corpus callosum.</i>	52
<i>Figure 4.13: Isolation of tracks of interest after track generation using ROI-editing techniques and manual correction. SSC: somatosensory cortex, CC: corpus callosum.</i>	53
<i>Figure 4.14: Plots of the normalized AFD in each tract of interest at each time point. CC: corpus callosum, CG: cingulum.</i>	54
<i>Figure 5.1: Interpretation of spatio-temporal pattern of diffusion metrics obtained by DTI, DKI and the biophysical model.</i>	55
<i>Figure 8.1: Boxplots of the metrics derived from DTI (columns) averaged by study groups and time points in each ROI (row). Significant differences between and within study groups are shown in the Table 8.1 and Table 8.2. Fundamental differences are shown in the Section 4.2.1.</i>	66
<i>Figure 8.2: Boxplots of the metrics derived from DKI (columns) averaged by study groups and time points in each ROI (row). Significant differences between and within study groups are shown in the Table 8.1 and Table 8.2. Fundamental differences are shown in the Section 4.2.1.</i>	67
<i>Figure 8.3: Boxplots of two metrics derived from the model (columns) averaged by study groups and time points in each ROI (row). Significant differences between and within study groups are shown in the Table 8.3 and Table 8.4. Fundamental differences are shown in the Section 4.2.2.</i>	69
<i>Figure 8.4: Boxplots of remaining three metrics derived from the model (columns) averaged by study groups and time points in each ROI (row). Significant differences between and within study groups are shown in the Table 8.3 and Table 8.4. Fundamental differences are shown in the Section 4.2.2.</i>	70

List of Tables

<i>Table 4.1: Average R calculated after 5 different linear registration procedures for each ROI in each study group. CC: corpus callosum, CG: cingulum.</i>	<i>44</i>
<i>Table 4.2: Average R calculated after linear and non-linear registration of the method selected for the corpus callosum (CC) and the fimbria in each study group.</i>	<i>46</i>
<i>Table 4.3: Comparison between t-tests computed in the preliminary results and with CCFAx in the corpus callosum (CC). p-values quantify differences between groups at each time point in diffusion metrics.</i>	<i>47</i>
<i>Table 4.4: Comparison between t-tests computed in the preliminary results and with CCFAz in the fimbria. p-values quantify differences between groups at each time point in diffusion metrics.</i>	<i>47</i>
<i>Table 4.5: Number of iterations with each exitflag value for each voxel.....</i>	<i>48</i>
<i>Table 8.1: Significant differences ($p<0.05$) between study groups in metrics derived from DTI and DKI in each ROI and at each time point.</i>	<i>68</i>
<i>Table 8.2: Significant differences ($p<0.05$) over time in metrics derived from DTI and DKI in each ROI and within each study group.</i>	<i>68</i>
<i>Table 8.3: Significant differences ($p<0.05$) between study groups in metrics derived from the model in each ROI and at each time point.</i>	<i>71</i>
<i>Table 8.4: Significant differences ($p<0.05$) over time in metrics derived from the model in each ROI and within each study group.</i>	<i>71</i>

List of Abbreviations and Notations

Aβ	Amyloid- β	FOV	Field of view
ACC	Anterior cingulate cortex	icv	Intracerebroventricular
AD	Alzheimer's disease	IR	Insulin receptor
AFD	Apparent Fiber Density	MD	Mean diffusivity
AK	Axial kurtosis	MK	Mean kurtosis
APP	A β protein precursor	MRI	Magnetic resonance imaging
A_xD	Axial diffusivity	MTL	Medial temporal lobe
c₂	Fiber orientation dispersion	NFT	Neurofibrillary tangles of tau
CCFA	Color-coded FA	ODF	Orientation distribution function
CSF	Cerebrospinal fluid	PET	Positron emission tomography
CTL	Control	PPC	Posterior parietal cortex
D_a	Parallel intra-axonal diffusivity	RD	Radial diffusivity
D_{e,}	Parallel extra-axonal diffusivity	RF	Radiofrequency
D_{e,⊥}	Perpendicular extra-axonal diffusivity	RK	Radial kurtosis
DKI	Diffusivity kurtosis imaging	ROI	Region of interest
DOF	Degrees of freedom	rs-fMRI	Resting-state functional MRI
DTI	Diffusion tensor imaging	RSC	Retrosplenial cortex
DWI	Diffusion weighted imaging	SNR	Signal-to-noise ratio
EPI	Echo-planar imaging	STZ	Streptozotocin
f	Water volume fraction	TE	Time of echo
FA	Fractional anisotropy	TR	Time of repetition
FDG	2-[¹⁸ F]fluoro-2-Deoxy-D-glucose	WHS	Waxholm space

1. Introduction

Alzheimer's disease (AD) is a multifactorial neurodegenerative disorder affecting 10% of the population over 65 years old. AD is the most common form of dementia and its increasing incidence is leading to a costly burden of disease. There is no effective cure to AD since brain damage begins 20 years before clinical symptoms are evident, which are manifested by cognitive and memory impairment [1]. Current approaches to treat AD have failed because at time of symptoms onset, the disease is already irreversible. According to the Alzheimer's Association, due to the rising life expectancy and other environmental factors, the incidence of AD is expected to quadruplicate by 2050 if no healthcare plan, other than palliative care or social support, is provided [2]. Hence, it is of the outmost importance to understand the determinants leading to AD development in its long asymptomatic stage.

According to the report "Health at a Glance 2017" published by OCDE, Portugal is the fourth country in the EU with the higher prevalence of dementia, with an average of 1 in each 50 inhabitants having dementia. In Switzerland, 1 in each 58 inhabitants suffer from dementia and the tendency of incidence is to double in the next 10 years, according to the non-profit organization Alzheimer Switzerland.

Even though the trigger mechanism of the disease remains unknown, AD is well characterized by a pathological cascade of events that defines the temporal progression and severity of the disease, which normally ends in dementia because of the late diagnosis [3]. The pathological hallmarks of the cascade include aggregation of amyloid- β plaques and neurofibrillary tangles of tau, cortical atrophy, synaptic dysfunction, inflammation and hypometabolism of glucose. Understanding the temporal and causal relationships between them might offer the opportunity for an early and efficient detection.

Fortunately, animal models provide the possibility to tease out the individual impact of each of these hallmarks and perform longitudinal studies in a relatively short period of time [4]. Following an intracerebroventricular (icv) injection of Streptozotocin (STZ), animals develop impaired glucose metabolism in the brain [5]–[7]. Several studies have reported AD-like features in icv-STZ animals [8]–[12], but this model has never been assessed with magnetic resonance imaging (MRI) derived biomarkers.

MRI has emerged in the 70's, even though the first clinical MRI scanners have appeared in 1990. It relies on generating 3D images by measuring the magnetic moments of particles in resonance. With a range of contrasts that provide better image detail than Computed Tomography, MRI has become one of the standard non-invasive non-ionizing imaging modalities. Both structural and functional imaging have profited from the introduction of MRI, with several applications coming along with it. In particular, diffusion-weighted imaging (DWI) was introduced in 1986 and relies on the Brownian motion of water molecules to study the underlying microstructure of tissues [13]. Fibrous tissues such as white matter tracts present a restricted diffusion which provides contrast to images. The study of skeletal and cardiac muscle is one of the applications of DWI, however neuroimaging research has made the most promising advances. While ischemic stroke is the killer application of DWI, this technique has brought over the past 30 years an incontestable insight into neurodegenerative processes.

Several approaches have been proposed to model diffusion within the brain. From the simple diffusion tensor imaging to the non-Gaussian diffusivity kurtosis imaging [14], [15], numerous metrics can be extracted from DWI data to quantify microstructure. Moreover, biophysical models of neuronal diffusion have emerged to provide specificity to the interpretation of changes, which indicate abnormalities in tissue microstructure such as demyelination, inflammation, axonal loss, among others [16], [17]. Tractography has become the standard approach to assess brain connectivity using diffusion data [18].

White matter degeneration has been proposed as a promising biomarker for AD that well precedes cortical atrophy and correlates strongly with disease severity and progression [19]–[21]. Given its anisotropic diffusion properties, white matter tracts have been widely assessed using DWI [22], [23], be-

cause the diffusion tensor is sensitive to the direction of diffusion. Therefore, this master's project consisted in a longitudinal study of the white matter microstructure in the icv-STZ rat using DWI. Longitudinal information was expected to contribute to the understanding of the spatio-temporal impact of the disrupted metabolism of brain glucose in the white matter tracts as well as of the temporal interplay between microstructural damage, amyloid deposition, functional loss and cognitive performance.

This project occurred in the context of the integrated BSc/MSc in Biomedical Engineering and Biophysics of Faculdade de Ciências da Universidade de Lisboa (FCUL) in Portugal and took place at Centre d'Imagerie Biomédicale (CIBM), École Polytechnique Fédérale de Lausanne (EPFL) in Switzerland, from September 2018 to June 2019. The main objective of this project was the biological interpretation of neurodegeneration results obtained by an existing processing pipeline of DWI images. From an engineering perspective, optimization strategies to improve the processing pipeline and the statistical analysis were tested and implemented in the course of the traineeship.

Theoretical background on AD's pathological features and the icv-STZ animal model are further described in the Section 2.1. MRI principles are shortly explained as well in the Section 2.2 and DWI fundamentals and applications are put into neuroimaging context in the Section 2.3, by characterizing the standard cutting-edge mathematical models to assess diffusion data. In the Section 2.4, general image processing techniques including registration and intensity and noise correction are briefly mentioned. The study design is described in the Section 3.1 and the methodology used in this project consists in the MRI data acquisition explained in the Section 3.2, the image processing pipeline and the statistical analysis. The image processing pipeline is divided into the existing pipeline and the optimization strategies.

The existing image processing pipeline was developed by Dr. Ileana Jelescu and used in previous projects. It includes image reconstruction, registration and correction, as well as two different approaches to assess DWI data. Namely diffusion and kurtosis tensors and the WMTI-Watson biophysical model of the white matter. This pipeline is fully described in the Section 3.3 because it was firstly used to obtain preliminary results. Practice using this pipeline provided deep understanding of the processing methodology and allowed for the development of strategies towards its optimization.

These strategies were tested following the purpose and procedure described in the Section 3.4. Optimization strategies were focused on obtaining more efficiently reliable and accurate results in terms of data quality and statistical power. They consisted in speeding up some of the steps in the existing processing pipeline, improving registration methods and diffusion metrics extraction from available data. The Section 4.1 shows the performance of each of these strategies and whether they were an additional value to the existing pipeline or not. If so, they were integrated in the pipeline to achieve the final results.

After image processing, statistical analysis of the measures extracted from tensors and the biophysical model is described in the Section 3.5. Tests here described allowed for the quantification of changes in the white matter microstructure and were computed after integrating in the existing pipeline the strategies that were previously shown to be effective improvements in terms of data quality or reliability. Results are shown in the Section 4.2.

Other strategies were proposed as well in this project to complement the final analysis and take advantage of the available diffusion data. These included performing tractography and diffusion analysis of the gray matter. The purpose and procedure to test these strategies are described in the Section 3.6. Additional diffusion analysis did not affect statistical tests as strategies were not meant to replace any stages of the processing pipeline, but to support the results from the statistical analysis of diffusion metrics in the white matter. The performance of these strategies are shown in the Section 4.3.

The results from each part of the methodology pipeline are addressed and interpreted in depth in the Chapter 5, as well as potential drawbacks of the final optimized processing pipeline and promising advantages of this project. The consistency of the results presented with the existing literature is evaluated and so is the future lines of this project at CIBM towards the understanding of AD progression and the spatio-temporal relationship between the hallmarks characteristic of the pathological cascade.

2. Theoretical Background

2.1. Alzheimer's disease

Alzheimer's disease (AD) is a progressive multifactorial neurodegenerative disorder without effective treatment. AD is the most common form of dementia, affecting 10% of the population over 65 years worldwide. According to Alzheimer's Association, the incidence of AD will quadruplicate until 2050 if no healthcare plan is provided with its outburst already constituting an economic and social burden [2].

Over the years, the view of Alzheimer's disease (AD) has been changing in what concerns to the clinical progression of the disease. As recently as 30 years ago, pathological changes and clinical evidence were believed to be independent. The current view of AD is that these occur gradually, with dementia being the end stage of many years of accumulation of brain alterations. Dementia might be defined as the clinically observable result of the cumulative burden of multiple pathological insults in the brain [3], that implies an inevitable course towards the complete loss of autonomy.

Importantly, it is now well-established that pathological changes begin to develop decades before the earliest clinical evidences [1]. According to the clinical stage, the disease has been divided into three phases [24]. The first one is the long asymptomatic phase, in which individuals are cognitively normal but might show pathological changes. The second phase is the mild cognitive impairment and consists in the early onset of cognitive symptoms, most likely deficits in episodic memory, that do not meet yet criteria for dementia but are at high risk for developing AD. The last phase is dementia, in which there are irreversible impairments in multiple domains that are severe enough to produce loss of function.

2.1.1. Pathological cascade of AD

The measurement of biomarkers in longitudinal studies enables the understanding of the interplay between them and their relationship to clinical symptoms, being a biomarker defined as any chemical or imaging indicator of specific changes that characterize AD. The time-dependent occurrence of different physiological changes could provide an effective disease staging, its expression as clinical changes and a prediction of mild cognitive impairment conversion into AD. In that regard, many studies have proposed the order in which relevant biomarkers occur in the disease progression [1], [24], [25], allowing studies from different disciplines to relate to one another through a common framework.

AD is clinically manifested by progressive memory loss and gradual decline in cognitive function, often culminating in premature death. Neuropathologically, AD is characterized by abnormal protein deposits and neurodegeneration. The former includes both amyloid- β ($A\beta$) plaques in the extracellular space and intracellular neurofibrillary tangles of hyperphosphorylated tau (NFTs). Normally, measuring the concentration of $A\beta_{42}$ or tau in the cerebrospinal fluid (CSF) within the ventricles is a way of evaluating abnormal plaques deposition, as well as Positron Emission Tomography (PET) imaging. Nearly all patients clinically diagnosed with AD have positive amyloid imaging studies [26].

In turn, neurodegeneration is manifested as reduced brain glucose metabolism [27] that leads to neuron loss and synaptic dysfunction and these to gross cerebral atrophy [28], especially in the hippocampus and parietotemporal cortex [19], [20], [29]–[31]. In this context, AD is commonly assessed either by histological *post-mortem* examinations, anatomical MRI to provide volumetric measures of atrophy or 2- $[^{18}F]$ fluoro-2-Deoxy-D-glucose (FDG) PET. A decreased uptake of FDG has been well correlated with impaired synaptic activity and cognitive decline [32].

Brain structural atrophy encountered in AD studies in humans refers to both gray and white matter degeneration. In terms of the temporal projection of these mechanisms, the emerging hypothesis, though not fully established, is that gray matter degeneration begins in the temporal lobe and progresses to other

brain areas via degenerating white matter tracts [33]. The most reported gray matter regions early affected are the medial temporal lobe (MTL), the parietal cortex and the posterior cingulate cortex [34], while the main white matter tracts affected are the corpus callosum, the cingulum and the fornix [19], [35]. White matter degeneration has recently been gathering attention as a key biomarker for AD, being strongly correlated with disease severity and progression [19], [21], although its relationship with clinical symptoms is largely under-investigated.

All these hallmarks of AD occur in a pathological cascade, that is yet to be fully understood. One of the proposed temporal progression of pathological changes is shown in *Figure 2.1* and suggests that malformation of protein precedes neurodegeneration, neurodegenerative biomarkers are temporarily ordered and biomarkers abnormalities precede clinical symptoms [1], [24].

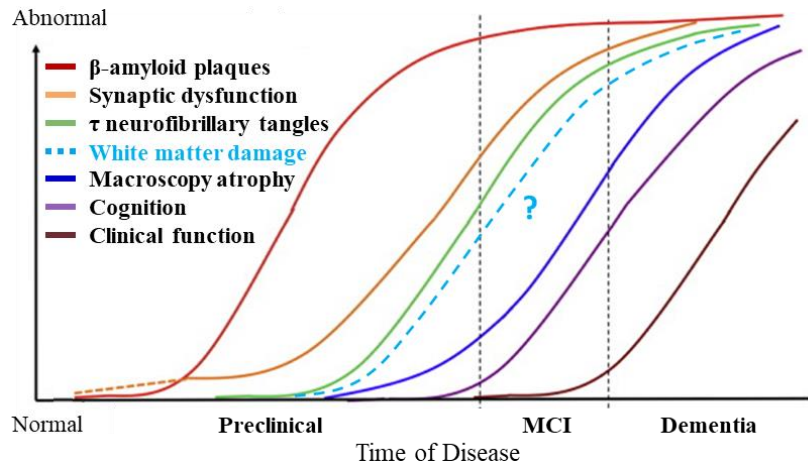


Figure 2.1: Pathological cascade of AD adapted from Jack et al, 2013 [24]. Evolution of biomarkers over disease progression, where white matter degeneration might have a key role. MCI: mild cognitive impairment.

2.1.2. Etiopathology of AD

There are two origin-based types of AD, despite the indistinguishable clinical symptoms. The early-onset familial AD occurs in a very small proportion ($\approx 1\%$) of the population compared to the sporadic late-onset AD. Familial AD has a genetic origin and is caused by a mutation in A β protein precursor (APP), presenilin-1 or presenilin-2. While an abnormal processing of APP leads to the excess production and/or reduced clearance of A β in the cortex, presenilin mutations encode abnormal cleavage of A β from APP to generate amyloidogenic A β peptides [36]. Nevertheless, the majority of the cases are sporadic in origin, with aging, type II diabetes and apolipoprotein E4 as the main risk factors [37].

The uncertainties associated with the etiopathology and progression of AD have led to intense investigation over the past years. The most prevailing theory stands in the amyloid cascade hypothesis, where neuropathological alterations are downstream consequences of a gradual aberrant A β accumulation [38], [39], as represented by the *Figure 2.1*.

An amyloid is a type of protein susceptible to structural conversion. Amyloid protein aggregation is considered a hallmark in several degenerative disorders, depending on the major constituents of the A β plaques. In AD, A β plaques are mainly formed by A β_{40} and A β_{42} peptides, which vary in the amino acids present at the C-terminal, resulting in distinct toxicity profiles. Due to environmental and genetic factors, A β peptides may undergo a toxic process of on-path oligomerization and be transformed into metastable structured oligomeric species, contributing to the proliferation of toxic species and the acceleration of neurodegeneration. A β oligomers affect cellular membranes on multiple levels by inducing endocytosis of the cell, influencing cellular signalling transduction, dysregulating the flux through the cell pores or being internalized into neurons and accumulated intracellularly [40]. These damaging events induce microglia and astrocyte activation and typically involve the presence of NFTs [41].

In accordance, evidence clearly shows that severe amyloidosis triggers familial AD [39], [42]. Yet, A β has not been proven to be required for the onset and progression of sporadic AD, despite of its early occurrence [37], [43]. Evidence indicates that A β is normally present in the brain, being in higher levels in younger than in older individuals in the absence of dementia [44]. Whereas mutations do not manifest dementia until 40 years of age [45], 30% of individuals carrying *pre-* or *post-mortem* detected amyloid plaques are cognitively intact [46]. In addition, immunotherapy can remove these plaques but does not affect the progression of dementia, suggesting that A β may not be sufficient to cause dementia [47].

So far, brain metabolic decline has been assumed to result from A β plaques and NFTs aggregation, being ultimately associated with dementia [48], [49]. Curiously, dementia has been reported in rodents, which do not produce A β , implying that the mechanism that triggers the cascade must be prior to A β aggregation. Hence, the aggregation of A β has been questioned as the primary cause of AD, being instead proposed as a secondary consequence of disturbed insulin/glucose metabolism in the brain [43].

In the mature brain, most of the insulin derives from the periphery, being transported by the CSF after its synthesis in the pancreatic β -cells and a smaller portion is synthesized *de novo* in the brain. As well as in the periphery, insulin actions in the brain are mediated by insulin receptors (IRs), a tyrosine kinase type of receptors. As shown in the *Figure 2.2*, insulin binds to IRs promoting autophosphorylation of their intracellular domain. Activated IRs phosphorylate intracellular substrates that activate several signalling pathways, one of which triggers the translocation of the insulin-sensitive glucose transporter to the membrane surface, enhancing cellular glucose uptake [50]. In addition to be the master regulator of brain glucose metabolism, insulin plays a significant role in neuronal growth [51], influences APP metabolism potentiating A β formation [52] and tau phosphorylation [53] and is involved in synaptic plasticity by altering gene expressing required for long-term memory consolidation [54].

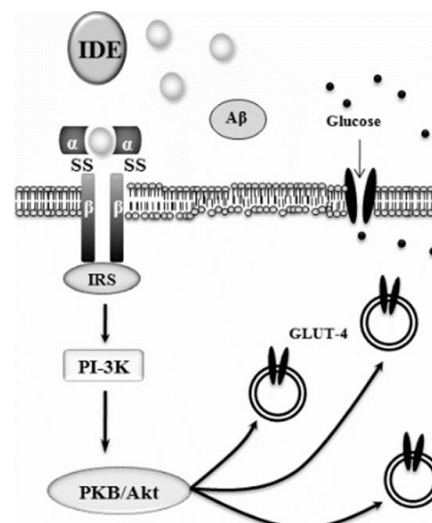


Figure 2.2: The role of insulin in the cellular membrane. PI-3K and PKB/Akt: signalling pathways. GLUT4: glucose transporter [51].

It has been reported that AD patients have higher levels of plasma insulin as well as decreased IR density and reduced tyrosine kinase activity [55] reinforcing the idea that abnormalities in brain insulin function and insulin signal transduction are major factors that influence the onset of AD [50]. It has also been shown that insulin administration improves cognitive performance in AD patients [56]. In that regard, reductions in brain glucose have been shown to decrease the rate of acetyl-coenzyme A suggesting a causal role of glucose metabolism dysfunction in the loss of cognitive function [57].

Other less acknowledged hypotheses for the primary cause of development and progression of AD are tau pathology, synaptic loss and inflammation [58].

2.1.3. Animal models of AD

One problem in investigating neurodegenerative disorders is obtaining comprehensive longitudinal data on prospective patients. Longitudinal studies in animals are of particular interest because the study can be designed across their entire lifespan, whereas many years would have to be dedicated to capture the human lifespan. Besides, animal models allow studying each of the characteristics and the disease stages individually, which is particularly important when multiple domains are affected simultaneously.

Independent mechanisms can be studied separately by biologically modifying the animals, with an increasing use of rodents to reproduce AD. Transgenic mouse models of AD are very common in research and focus on reproducing protein mutations, namely APP, presenilin or tau protein. The mouse models most used in current AD research are the triple transgenic model (3xtg AD) and the 5XFAD (Tg6799) mouse line. Whereas transgenic mice are naturally representative of familial AD, the sporadic form of AD is reproduced without genetic modifications. With AD being increasingly recognized as an insulin-resistant state, a non-transgenic animal model has emerged to reproduce early pathological changes of sporadic AD [5], [6], [59]. This model consists in an intracerebroventricular (icv) injection of streptozotocin (STZ), which is a toxic diabetogenic substance that damages pancreatic β cells when given parenterally. When injected exclusively into the ventricles, STZ does not induce type I diabetes because the molecule cannot pass across the blood brain barrier to reach the systemic circulation. For that reason, icv-STZ induced-AD has been referred to as type III diabetes or “diabetes of the brain” [11].

Even though its mechanism is not fully elucidated, STZ is thought to disrupt the brain IR system thereby reducing the glycolytic metabolism in the parietotemporal cortex and in the hippocampus [7]. Accordingly, behavioural, neurochemical and structural features reported in icv-STZ studies resemble those found in the human AD brain, validating this experimental model. Several icv-STZ animals such as mice, rats, dogs, pigeons, monkeys and pigs have been studied and displayed features including memory impairment, thinning of the parietal cortex and corpus callosum, NFT changes and extracellular accumulation of A β early in the neocortex and later in the hippocampus [9]. Focal lesions on the corpus callosum and on the septum were found in the form of neuronal loss and inflammation, as well as atrophy of the entorhinal, cingulate cortex and hippocampal regions [8]. In addition, histopathological studies have shown evidence of axonal damage and demyelination in the hippocampus and fornix, where abnormal transport of nerve growth factor has been reported. More than disrupting brain glucose metabolism, STZ also induces oxidative stress to which myelin is particularly vulnerable [8]–[12].

The icv-STZ model has been demonstrating its potential to reproduce sporadic AD [60]. However, beyond anatomical MRI, all icv-STZ studies have used histology, immunohistochemistry, PET and electron microscopy derived-biomarkers. Pathological alterations typical of this animal model have never been assessed with MRI techniques, which have brought a significant insight into neurodegenerative processes with such a broad spectrum of contrast mechanisms as described in the Section 2.2. This scenario opens a window for future investigation, provided that white matter degeneration has been repeatedly reported in icv-STZ studies and a unique way to assess brain microstructure is diffusion weighted imaging (DWI), as explicated in detail in the Section 2.3.

2.1.4. Relevant rat brain anatomy

AD has been highly associated with degeneration in the hippocampus as one of the explanations to high memory deficits. The hippocampus is a major component of the brain, located in between the medial temporal lobes (MTL) and is composed of several subparts such as the dentate gyrus, *cornus ammonis* and subiculum. There are two groups of fibers covering its communication with the brain: the myelinated tract that connects the ventricle part of the hippocampus is designated by alveus, while the tract that covers the temporal part of the hippocampus is the fimbria-fornix complex. This complex is a C-shaped structure composed by fiber bundles that are mainly output tracts of the hippocampus.

The fimbria is composed by two separated bundles on the left and right sides that leave the hippocampus and go to a posterior and superior location around the thalamus where the bundles take the name of *crura* of the fornix. These are intimately connected with the under surface of the corpus callosum and come together in the midline of the brain forming the body of the fornix. Between the corpus callosum and the fornix lies a transparent membrane composed of white matter fibers referred to as septum. The two hippocampi are thus connected by the hippocampal commissure. Going along with the corpus callosum to the anterior part of the brain, the fornix is divided into two arches and meet the mammillary bodies. The function of this complex in the physiology of the brain is not entirely understood, although the fimbria and the fornix are thought to be related to learning and memory processes intermediation.

As a wide, thick and flat tract across the entire brain, the corpus callosum is the largest white matter structure there is. It is a bundle of commissural fibers beneath the cerebral cortex and above the fornix and it connects the left and the right cerebral hemispheres enabling communication between them. The corpus callosum is divided into several parts depending on the coronal position. Towards the frontal lobe, the bundles are designated genu, whereas towards the occipital lobe and the cerebellum the bundles are designated splenium. Behind the splenium stands the retrosplenial cortex (RSC), whose function might be related to mediating perceptual and memory functions.

The trunk of the corpus callosum is located in the middle of the brain and connects exactly the two sides of the temporal lobe, through a tract named anterior commissure. The cortices are connected to inferior parts of the brain through the numerous ramifications of the corpus callosum, in particular the external capsule. The posterior parietal cortex (PPC) is on top of the corpus callosum and is responsible for receiving information from somatosensory systems.

Right above the corpus callosum is the cingulum, which is composed of two groups of fibers in a C-shaped structure as well. The cingulum is located beneath the cingulate cortex from where fibers are projected into the entorhinal cortex and the RSC. The anterior cingulate cortex (ACC) controls emotion such as apathy and depression, while the posterior part of the cingulate cortex is in charge of cognitive function such as memory. While establishing the communication between these regions, the cingulum has a serious role in the correction of mistakes, appraisal of pain and reinforcement behaviour. These regions are represented in the *Figure 2.3*.

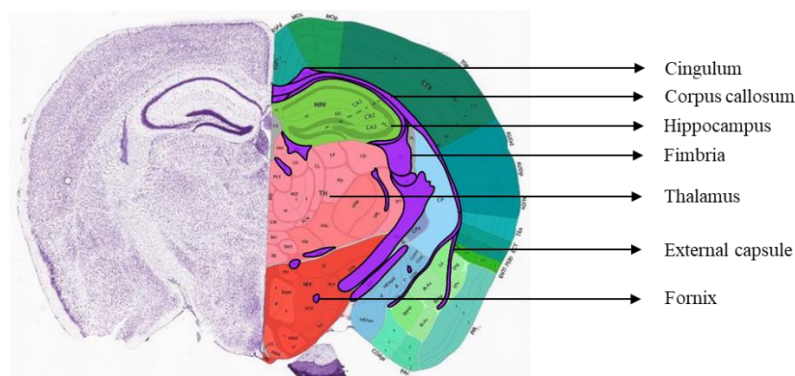


Figure 2.3: Anatomy of the rat brain from the Allen Brain Atlas in a coronal plane. Regions in purple correspond to white matter tracts.

2.2. Magnetic Resonance Imaging principles

2.2.1. Alignment and precession of magnetic moments

The atom is the smallest constituent unit of ordinary matter and is composed of protons, neutrons and electrons. Electrons are negatively-charged and orbit around the atomic nucleus that is composed by positively-charged protons and uncharged neutrons. In quantum mechanics, elementary particles such as atomic nuclei carry an intrinsic angular momentum called nuclear *spin*. The spin assumes two possible values ($-\frac{1}{2}$ and $+\frac{1}{2}$) and the proportion of populations in each of the two states is given by the Boltzmann distribution which gives the relative weight of magnetic energy to thermal energy. However, while this is a purely quantum phenomenon, a convenient classical description might be used to explain it. Herein, MRI is explained with an illustrative classical approach.

From the classical physics point of view, the spin is viewed as the rotational motion of the nuclei around their own axis and the principles of MRI rely on that spinning motion of specific nuclei present in biological tissue. Following the laws of electromagnetic induction, when a charged nucleus is spinning, it acquires a magnetic moment and therefore is able to align with an external magnetic field. In the absence of an external magnetic field, the orientations of the nuclear spins are random. Contrarily, when a magnetic field B_0 is applied, the magnetic moments of the nuclei are capable of aligning in either a parallel or anti-parallel direction. These two states of energy are explained by quantum physics that describes the properties of electromagnetic radiation in terms of discrete quantities.

The parallel aligning nuclei are the low-energy population that does not have enough energy to oppose B_0 and therefore the magnetic moments align in the same direction as the B_0 . On the contrary, the anti-parallel nuclei are the high-energy population that opposes B_0 and aligns in the opposite direction of B_0 . Naturally, the low-energy population is larger and there is a small excess of magnetic moments in the parallel direction. The energy difference between the two populations produce a net magnetic moment which is proportional to the strength of B_0 . The higher the B_0 , the fewer nuclei in the anti-parallel state, the higher the energy difference and the larger the magnetization, that ultimately improves the MRI signal. The alignment phenomenon is shown in the *Figure 2.4*.

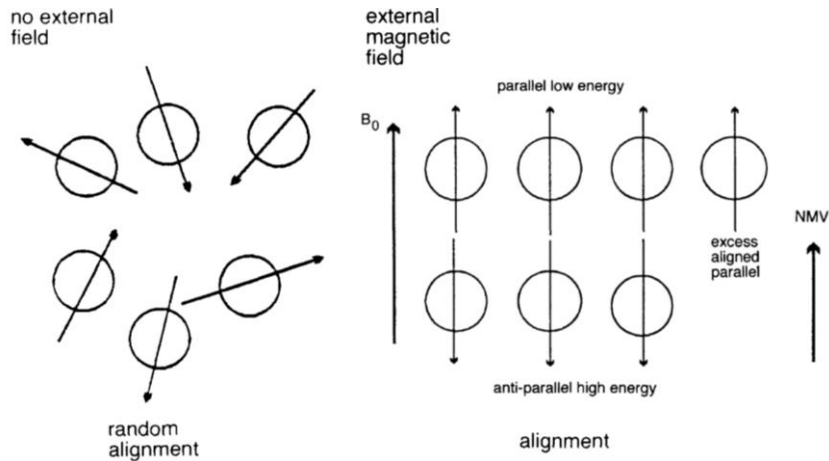


Figure 2.4: Alignment of nuclear spins with no external field applied (on the left) and in the presence of B_0 (on the right) [61]. NMV: net magnetization vector.

Every nucleus that makes up the net magnetization is spinning on its own axis with one of two orientations. In addition, the influence of B_0 produces another rotation of the magnetic moment around B_0 , which is called precession and is shown in the *Figure 2.5*. The speed at which the net magnetization precesses around B_0 is called precessional frequency ω_0 and depends on nuclei properties, such as the gyromagnetic ratio γ , as stated by the Larmor equation in the Equation 4.1 [61]–[63].

In particular, hydrogen creates a large net magnetization after aligning with B_0 since it is relatively more abundant in biological tissue than other species and hydrogen nuclei have a large gyromagnetic ratio. Providing that the gyromagnetic ratio of the hydrogen nuclei is 42.57 MHz/T, if an external field of 14.1 T is applied, their precessional frequency is roughly 600 MHz.

$$\omega_0 = B_0 \gamma \quad [4.1]$$

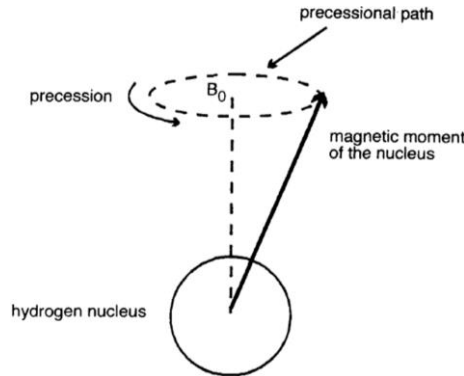


Figure 2.5: Precessional movement of the net macroscopic magnetic moment induced by B_0 [61].

2.2.2. Resonance phenomenon

Acquaintance with the precessional frequency is fundamental to produce resonance of a nucleus and produce a moving magnetic field that can finally be captured by a coil to acquire an MRI signal. The phenomenon of resonance occurs when a nucleus precessing in its natural frequency is exposed to an external perturbation with an oscillation with similar frequency and gains energy from the interaction. For resonance of hydrogen to happen, a radio-frequency (RF) pulse at frequency equal to the hydrogen's precessional frequency must be applied. Other nuclei that have aligned with B_0 do not resonate because their precessional frequency is different from that of the hydrogen.

As a result of resonance, the absorption of energy from the RF pulse by the nuclei increases the high-energy population as some of the low-energy nuclei gain enough energy to oppose B_0 . With a balanced number of nuclei in both populations, the longitudinal component of the magnetization is completely transferred into the transverse plane and is no longer affected by B_0 as shown in the Figure 2.6. The angle at which the net magnetization moves relatively to B_0 direction is called flip angle and depends on the amplitude and duration of the RF pulse. The transverse component of the magnetization rotates at the Larmor frequency and the magnetic moments of the hydrogen nuclei move in phase with each other.

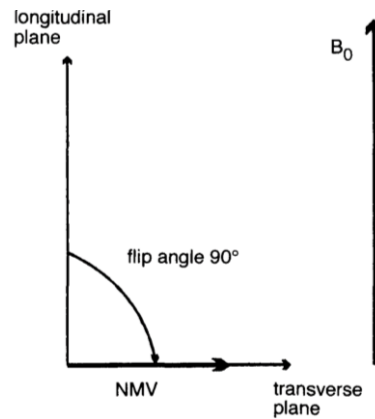


Figure 2.6: The net magnetization vector (NMV) is completely transferred from the longitudinal to the transverse plane after a 90° RF pulse as a resonance result [61].

When the RF pulse is switched off, the net magnetization is influenced by B_0 again and realigns with it, by losing the energy it has acquired from the RF pulse. The process of returning to the original longitudinal alignment is called relaxation and consists in two phases, namely the recovery phase and the decay phase. The recovery phase is the exponential increase of longitudinal magnetization while the nuclei transfer energy to the surroundings – spin lattice relaxation, with a time constant T_1 . The decay phase is due to the transfer of energy to other nuclei – spin-spin relaxation and it represents the exponential decrease of transverse magnetization with a time constant $T_2 < T_1$.

According to Faraday's laws of induction, a voltage is produced in a receiver coil when it experiences a time-varying magnetic flux through its cross-section. The precessing net magnetization produces such a time-varying magnetic flux in a receiver coil if the coil axis is perpendicular to B_0 , i.e. is parallel to the transverse plane. The induced voltage across the coil, and of the electric current flowing in the coil as a result, are proportional to the amplitude of the transverse magnetization. When the RF pulse is switched off, the transverse magnetization starts decaying and so does the voltage amplitude in the receiver coil. This reduced signal in induction is designated free induction decay [61]–[63].

2.2.3. Pulse sequence parameters and image contrast

Image contrast can be produced by exploiting T_1 and T_2 relaxation differences between different types of tissues. Fat tissue and water, for instance, have completely different properties that make them appear with opposite contrasts in the MRI image. Considering that relaxation relies on giving up energy, in fat tissue, the slow molecular mobility makes recovery and decay very efficient so that the net magnetization realigns quickly and leads to a short T_1 and T_2 . Regarding to water, the high molecular mobility makes recovery and decay less efficient, so that the net magnetization takes longer to realign and leads to long water T_1 and T_2 . This is shown in the *Figure 2.7*.

The amount of T_1 relaxation that has occurred is determined by the time between RF pulses, which is called time of repetition (TR). The amount of T_2 relaxation is controlled by the time of echo (TE), which is the interval between the application of the RF pulse and the peak of the signal induced in the coil. TR and TE are specifically set in a pulse sequence and their combination gives rise to different contrast mechanisms. For instance, in T_2 -weighted images, since water has a longer T_2 than fat tissue, it takes longer to lose its transversal magnetization. Thus, the signal amplitude of the water in the receiver coil is larger and water appears bright and fat tissue dark. The maximum contrast between tissues in T_2 -weighting occurs when there is the major difference in the transversal magnetization. Because TE controls the amount of T_2 decay, it controls the amount of T_2 -weighting. The contrary applies to T_1 -weighted images.

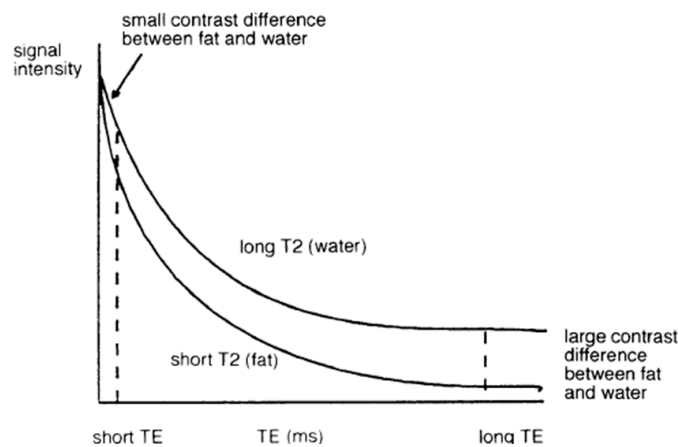


Figure 2.7: Difference of image contrast between fat tissue and water as a function of time parameters in a T_2 -weighted image [61].

The most standard pulse sequences in MRI acquisitions are spin-echo and gradient-echo. Spin-echo pulse sequences are characterized by having a 180° RF pulse after the initial 90° RF pulse, because of the so-called $T2^*$ decay. This decay is faster than the $T2$ decay because it also accounts for the effect of the magnetic field inhomogeneities that may cause spatial variations in precessional frequencies depending on the magnetic field experienced at a given location. To compensate for the dephasing induced by these variation, the 180° RF pulse rephases all nuclei by flipping magnetic moments to the opposite longitudinal magnetization and with the same transverse magnetization. After the 180° RF pulse, a maximum signal is induced in the coil generating an individual spin-echo used to create an image [61]–[63].

In a different approach, the gradient-echo pulse sequence uses variable magnetic fields that cause nuclei to precess at variable frequencies along the direction of the applied magnetic field gradient, leading to a phase shift. While a first gradient induces magnetic moments within the transverse magnetization to dephase, a consecutive gradient with reversed polarity and double the duration time rephase them, inducing a signal in the coil called the gradient echo. Unlike the spin-echo, the dephasing and rephasing occur in the same direction and do not cancel inhomogeneity effects. These pulse sequences are illustrated in the *Figure 2.8*. Many other sequences have been proposed according to the quality image required in each study [61].

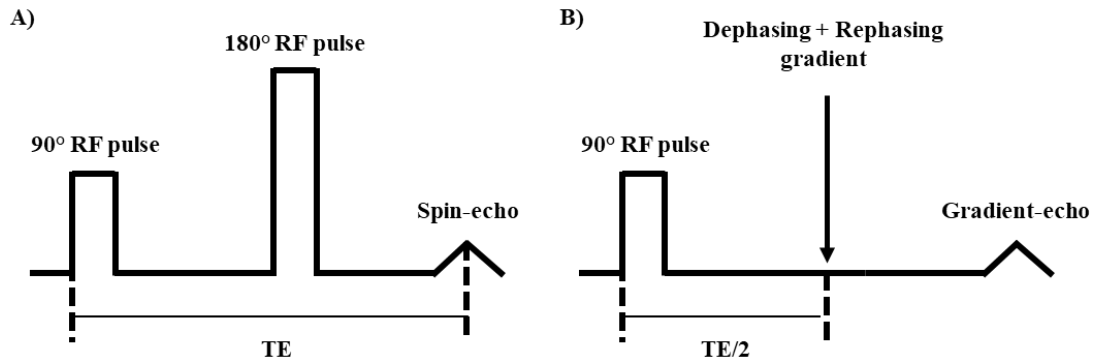


Figure 2.8: Spin-echo (A) and gradient-echo pulse sequences (B).

2.2.4. Signal acquisition and image reconstruction

Considering that the value of the magnetic field sets the precessional frequency at which nuclei precess, if the outer field is no longer homogeneous and there is a spatial gradient, nuclei in different regions will precess at different frequencies. This is the basis of MRI ability to spatially locate signals. Spatial encoding is performed by using three coils placed in the main directions. The magnetic field gradient is achieved by overlapping the field of these coils and its direction is determined by the combination of their orientations. The first encoding is the slice selection gradient and the frequency of the RF pulse defines the slice of the image and its thickness. The second encoding is called phase encoding and locates the signal along the short axis of the anatomy. From the moment each position in the short axis corresponds to a different phase, the various elements in that position are encoded by the frequency encoding gradient. This is perpendicular to the phase encoding gradient and defines the field of view (FOV).

At the end of all encoding, the signal coming from each slice is phase and frequency encoded. When applying the frequency encoding gradient, an echo is produced and corresponds to a real time series of measurements. The successive application of increasing phase selection gradients leads to the variation of these echoes according to TR . The echoes recorded in each TR are stored in an abstract spatial-frequency domain matrix, designated k -space, as shown in the *Figure 2.9*. The horizontal axis of the k -space is the phase information (k_{PE}) while the vertical axis corresponds to the frequency (k_{FE}). By applying the Fourier transform to the sampled time-dependent signal, the various frequencies specific to a point in the image are calculated and the image is able to be reconstructed.

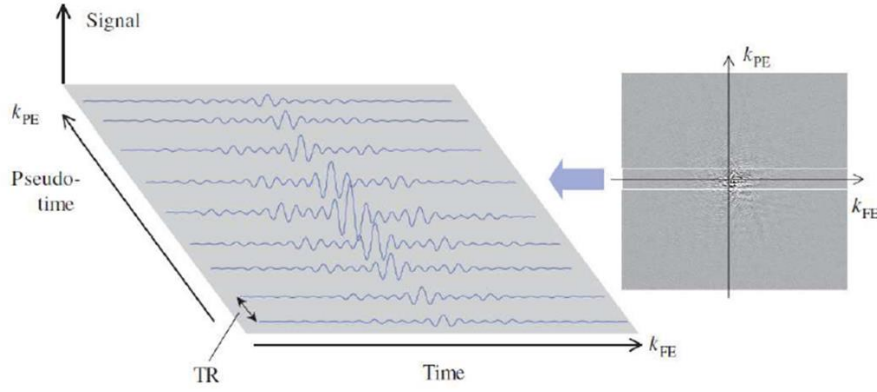


Figure 2.9: At each TR, echoes are stored in the frequency and phase encoded k-space to produce an image by applying a Fourier transform [63].

The simplest way to fill in the k-space is to start filling it sequentially line by line from bottom to top. However, this form of acquisition is slow and may limit clinical applications. In order to suit the circumstances at scan, other forms of acquisition are available such as fast spin-echo pulse sequences or echo-planar imaging (EPI). As suggested by its name, fast spin-echo is a spin-echo pulse sequence with scan times shorter than the conventional spin-echo, by filling out more than one line of the k-space per TR. This is achieved by using a train of several 180° RF pulses, each rephasing the spins and producing several echoes that lead to different phase encoding steps at each TR [61].

Taking the fast spin-echo to the limits, EPI fills all lines after one repetition [64]. The train of RF pulses is applied and afterwards, instead of filling out each line in the same direction from the left to the right, the k-space is filled in a spiral form beginning at the center. Not only does the frequency encoding oscillate to fill lines from left to right and then right to left, the phase encoding must also oscillate from bottom to top and then top to bottom. EPI has a huge potential in clinical applications due to its rapid data acquisition and sensitivity that can capture physiological motion. Despite all these advantages, the rapid switching of gradients causes severe noise vibration of the system.

Both spatial resolution and signal-to-noise ratio (SNR) characterize the image quality in MRI. The SNR is the ratio between the amplitude of the signal received and the average noise of the image. MRI-derived noise is generated both by physiological motion and thermal noise. In order to be minimized, the signal must be increased so that the SNR increases as well. Several factors affect the SNR, namely a high proton density, the thickness of slices or a wide FOV increase the SNR, although the latter will increase the partial volume effect [65]. Approaches for noise correction of images are described in the Section 2.4.

2.3. Assessing microstructure with diffusion-weighted imaging

2.3.1. Biological diffusion principles

Diffusion is a random transport phenomenon which describes the transfer of material, such as ions and molecules, from one spatial location to another over time. From the physical point of view, diffusion is characterized by the random walk of the diffusion particles, also known as Brownian motion. The Brownian net movement of particles suspended in a fluid result from their collision with fast-moving particles in that fluid, where there is no preferential direction.

The massive amount of interactions that yield the Brownian pattern (roughly 10^{14} collisions/s) cannot be solved by classical mechanics models that account for every involved molecule. Therefore, probabilistic models must be used to consider a collective motion of particles in the assessment of how far a Brownian particle travels in a given time interval. In 1905, Einstein developed the Brownian theory to find the relationship between the diffusion coefficient and the mean squared displacement of particles in random motion [66]. When the particle position is incremented over time in a space x with a random variable Δ with a probability density function $\varphi(\Delta)$, the density of diffusion particles is given by an expansion in a Taylor series, as shown in the Equation 4.2. The second order of probability of displacement in the Equation 4.2 might be interpreted as the mass diffusivity D , such that the density of particles at point x and at time t satisfies the diffusion equation in the Equation 4.3.

$$\frac{d\rho}{dt} = \frac{d^2\rho}{dx^2} \int_{-\infty}^{+\infty} \frac{\Delta^2}{2\tau} \varphi(\Delta) d\Delta + \text{higher order odd terms} \quad [4.2]$$

$$\frac{dp}{dt} = D \frac{d^2\rho}{dx^2} \quad [4.3]$$

Assuming that N particles start from the origin at the initial time $t = 0$, the diffusion equation has a solution with a Gaussian distribution with mean $\mu = 0$ and variance $\sigma^2 = 2Dt$ given by the Equation 4.4, which shows that the spread of particles increases with elapsed time. Evidently, when $\rho(x, t) = 0$, since a molecule is equally likely to diffuse in a positive or negative x -direction, the average displacement is zero. Therefore, the average square of the displacement can be considered instead, which is shown to be proportional to the elapsed diffusion time in the Equation 4.5 [66].

$$\rho(x, t) = \frac{N}{\sqrt{4\pi Dt}} e^{-\frac{x^2}{4Dt}} \quad [4.4]$$

$$\overline{\Delta x^2} = 2NDt \quad [4.5]$$

In the current context, the diffusion coefficient of pure water at 20 °C is $2 \mu\text{m}^2/\text{s}$ and increases at higher temperatures, according to the equation of the ideal gas law. Water diffusion is primarily caused by random thermal fluctuations and is modulated by interactions with cellular membranes and organelles. While cellular membranes hinder the extracellular diffusion of water, causing water molecules to take more tortuous paths and thereby decreasing the mean squared displacement, intracellular water tends to be more restricted. In fibrous tissues, water diffusion is relatively unimpeded in the direction parallel to the fiber orientation and hindered in perpendicular directions. Thus, diffusion in fibrous tissues is anisotropic as opposed to homogeneous unrestricted media.

To describe anisotropic diffusion, a diffusion tensor was introduced in the normal distribution of particles defined by the Equation 4.6 [22], [23]. The tensor is a 3×3 covariance matrix that describes the diffusion displacement in three dimensions of a single voxel. The diagonalization of the matrix is a common procedure as diffusion coefficients become independent of the orientation of the reference frame. It yields the eigenvalues $(\lambda_1, \lambda_2, \lambda_3)$ and corresponding eigenvectors $(\epsilon_1, \epsilon_2, \epsilon_3)$ of the diffusion tensor that correspond to the directions and apparent diffusivities along the axes of principal diffusion, that are obtained with the Equation 4.7.

$$D = \begin{bmatrix} D_{xx} & D_{xy} & D_{xz} \\ D_{yx} & D_{yy} & D_{yz} \\ D_{zx} & D_{zy} & D_{zz} \end{bmatrix} = \begin{bmatrix} D_{xx}' & 0 & 0 \\ 0 & D_{yy}' & 0 \\ 0 & 0 & D_{zz}' \end{bmatrix} \quad [4.6]$$

$$D = [\epsilon_1 \quad \epsilon_2 \quad \epsilon_3]^T \begin{bmatrix} \lambda_1 & 0 & 0 \\ 0 & \lambda_2 & 0 \\ 0 & 0 & \lambda_3 \end{bmatrix} [\epsilon_1 \quad \epsilon_2 \quad \epsilon_3] = \sum_{k=1}^3 \epsilon_k^T \lambda_k \epsilon_k \quad [4.7]$$

The diffusion tensor may be visualized as an ellipsoid, whose directions of the principal axes are characterized by the eigenvectors and the radii by the eigenvalues [22], [23], as shown in the **Figure 2.10**. When diffusion is isotropic, the ellipsoid resembles a sphere and eigenvalues are nearly equal ($\lambda_1 \approx \lambda_2 \approx \lambda_3$), whereas an anisotropic medium is represented by an ellipsoid with significantly different eigenvalues magnitudes (e.g. $\lambda_1 > \lambda_2 > \lambda_3$). The major diffusion eigenvector represents the direction of greatest diffusivity and it is assumed to be parallel to the main tract orientation. This directional relationship is the basis for diffusion tensor image metrics and tract reconstruction algorithms.

Therefore, diffusion neuroimaging techniques rely on the ability of the diffusion coefficient to provide information about microstructure. The eigenvalues magnitude might be affected by changes in local tissue microstructure such as tissue injury, disease or normal physiological changes such as aging, making the diffusion tensor a sensitive probe for characterizing both normal and abnormal tissue.

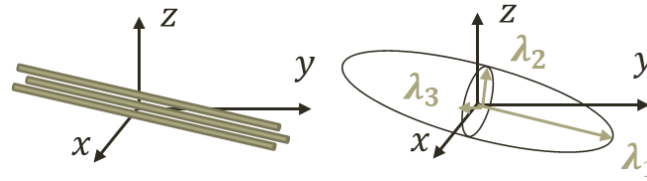


Figure 2.10: A fibrous tissue is an anisotropic medium and can be represented by an ellipsoid with one of the eigenvalue magnitudes greater than the others.

2.3.2. Diffusion-weighted imaging and signal representation

Diffusion-weighted imaging (DWI) is the application of MRI principles to the Brownian water motion within the human body. DWI is a unique method to describe the microstructure of the brain since its characteristic features are able to capture the displacement of water molecules (in 50 ms molecules move about 10 μm). The most common approach is the spin-echo pulse sequence with an EPI readout and a pair of opposite large-gradient pulses on both sides of the 180° refocusing RF pulse. While the first gradient dephases the magnetization across the sample, the second rephases the magnetization.

In stationary molecules, the phases induced by both gradient pulses completely cancel and the magnetization is maximally coherent, producing no signal attenuation from diffusion. Conversely, when there is coherent flow in the direction of the applied gradient, there is a change in the phase by different amounts for each pulse. The net phase difference produced is proportional to the displacement, which is described by the distribution in the Equation 4.5. In the presence of diffusion gradients, phase dispersion of water molecules generates attenuation of the signal S , i.e. contrast.

Without any *a priori* assumptions about the medium, the signal might be represented by a Taylor series called the cumulant expansion as shown in the Equation 4.8, where S_0 is the DWI signal without any gradients, b is the diffusion-weighting factor that characterizes the gradient pulses, K is the kurtosis of the diffusion tensor that quantifies complexity and inhomogeneity of the medium [14].

$$\ln\left(\frac{S}{S_0}\right) = -bD + \frac{1}{6}(bD)^2 K + \dots \quad [4.8]$$

The cumulant expansion can be simplified under the assumption that the medium is indistinguishable from a Gaussian medium. This distribution requires low diffusion-weighting (low b -values) so that $K = 0$ and uniformity of water distribution occurs in all directions. Thus, for isotropic Gaussian diffusion, the signal attenuation is described by the Equation 4.9 [13], with the b -value defined by the Equation 4.10. In this case, for the expansion up to the first order of the Equation 4.8 to be valid, $b \ll \frac{1}{DK}$ [68].

$$S = S_0 e^{-bD} \quad [4.9]$$

$$b = \gamma^2 G^2 \delta^2 \left(\Delta - \frac{\delta}{3} \right) \quad [4.10]$$

In the presence of anisotropy, diffusion can no longer be characterized by scalars and requires the use of the tensor in the Equation 4.6, that fully describes molecular mobility along each direction. The Equation 4.9 should then be rewritten as the combination of all main directions as in the Equation 4.11.

$$S = S_0 \exp \left(- \sum_{i=x,y,z} \sum_{j=x,y,z} b_{ij} D_{ij} \right) \quad [4.11]$$

In the Equation 4.11, b_{ij} are in this case the elements of the b matrix that replaced the b coefficient, since the b -value is different in each direction depending on the gradients used. To access the anisotropic diffusion effects, the diffusion tensor must be fully calculated, knowing both attenuated and non-attenuated DWI signals and collecting the b -values along several gradient directions. The use of the diffusion tensor to produce parametric maps is designated diffusion tensor imaging (DTI).

Although DTI metrics are recognized to characterize water diffusion properties, only part of the information is being assessed due to the assumption that the displacement function has a Gaussian distribution. Therefore, an extension to DTI has been proposed to quantify the non-Gaussian diffusion. Beyond low b -values, i.e. using the cumulant expansion, it is possible to estimate how much the medium deviates from the Gaussian distribution and further estimate K . The use of the kurtosis tensor to produce parametric maps is designated diffusivity kurtosis imaging (DKI) [14]. DKI has been gathering attention due to its sensitivity to microstructure not captured by the diffusion tensor in multiple clinical areas, including stroke [69] and children brain development [68].

Since b -values are quadratic terms, the 2nd order symmetric diffusion tensor requires measurements along at least six directions, while the 4th order kurtosis tensor requires at least 15 measurements. For DTI and DKI joint analysis, a minimum total of 21 gradient directions is necessary, even though collecting data along as many directions as possible is recommended to uniformize space sampling and increase SNR [70], [71]. Sampling directions are shown in the *Figure 2.11*. The estimation of D_{ij} and K_{ijkl} is generally done by multiple linear regression, and therefore measurements of diffusion in all directions require at least two non-zero b -values (shells). In *in-vivo* experiments, the maximum b -value for Gaussian brain DTI is roughly $b_{max} = 1 \text{ ms}/\mu\text{m}^2$ whereas for non-Gaussian brain DKI is $b_{max} = 2 \text{ ms}/\mu\text{m}^2$. Naturally, in *ex-vivo*, the maximum b -values are higher because diffusion is slower.

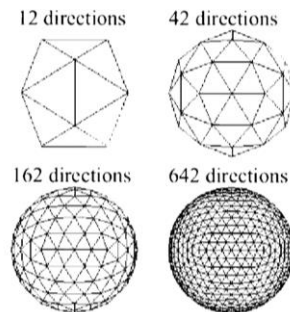


Figure 2.11: Directional sampling in increasing directions [67].

2.3.3. DWI data assessment using tensor-derived metrics

As aforementioned, despite being a high-sensitivity and non-invasive method, DWI is an indirect probe of the microstructure because its signal needs to be modelled to extract quantitative measures. The display and interpretation of 3D image data with diffusion and kurtosis tensors at each voxel must be simplified into simple scalar maps, by extracting metrics from the combination of eigenvalues.

Regarding DTI, although the apparent diffusion coefficient has been extremely successful in clinical practice, it is being replaced by direct quantitative measures. For instance, the mean diffusivity (MD) is a rotationally invariant measure – independent of the orientation of the reference frame [23]. MD characterizes the overall mean-squared displacement of water molecules in all directions, being equivalent to the average of the eigenvalues, as given by the Equation 4.12. Therefore, it is proportional to the trace of the diagonalized tensor and can be separated into axial (A_xD) and radial diffusivity (RD) according to the gradient directions, as shown in the Equations 4.13 and 4.14.

$$MD = \frac{Tr(\vec{D})}{3} = \frac{D_{xx}' + D_{yy}' + D_{zz}'}{3} = \frac{\lambda_1 + \lambda_2 + \lambda_3}{3} \quad [4.12]$$

$$A_xD = \lambda_1 \quad [4.13]$$

$$RD = \frac{\lambda_2 + \lambda_3}{2} \quad [4.14]$$

While low values of A_xD are representative of axonal degeneration, RD appears to be modulated by myelin in the white matter and thereby is expected to increase as a result of demyelination in neuro-degenerative processes. As a combination of diffusivity in each direction, MD is expected to decrease due to inflammation or to increase if there is loss of structure resulting in increased water mobility.

The degree to which diffusion is a function of DWI encoding directions is represented by metrics of anisotropy [67]. The most popular invariant metric of anisotropy is the fractional anisotropy (FA) and it represents the magnitude of the D that is attributed to anisotropic diffusion. FA varies between 0 (isotropic) and 1 (anisotropic) [72] and is described by the Equation 4.15.

$$FA = \sqrt{\frac{(\lambda_1 - MD)^2 + (\lambda_2 - MD)^2 + (\lambda_3 - MD)^2}{2(\lambda_1^2 + \lambda_2^2 + \lambda_3^2)}} \quad [4.15]$$

Because of the well-oriented integrity of white matter tracts and their myelin insulation, FA is expected to be higher within white matter tracts than in gray matter regions in normal conditions. In neurodegeneration, FA is expected to decrease because of fiber dispersion. Even though FA is sensitive to a broad spectrum of pathological conditions, different eigenvalues combinations can generate the same value of FA [73]. This means that FA recognizes changes in diffusion, but different pathologies such as inflammation, demyelination or axonal injury might result in the same change in FA.

Another relevant metric extracted from the diffusion tensor is the tensor orientation described by the major eigenvector direction. Using a color-coded map, the eigenvectors are represented to identify and parcelate specific white matter tracts [74]. These maps are hereafter called color-coded FA (CCFA) maps. The 3D approach of this metric is called DTI-based tractography [75], and it is greatly appreciated to anatomically track white matter bundles, as discussed in the Section 4.3.5.

Analogous to DTI, DKI defines the mean kurtosis (MK) as the directionally averaged observed kurtosis. However, because kurtosis is a 4th order tensor, it is calculated over at least 15 directions \hat{n} and MK is solved by averaging projections of the tensor over as many directions as possible, isotropically distributed on a sphere, as given by the Equation 4.16.

$$MK = \frac{1}{4\pi} \int K(\hat{n}) d\hat{n} \quad [4.16]$$

K provides as well metrics of the axial and radial components of kurtosis. Axial (AK) and radial kurtosis (RK) may be represented in terms of the eigenvectors of the diffusion tensor [14], even though different definitions have been proposed [76], as shown in the Equations 4.17 and 4.18.

$$AK = K(\hat{\epsilon}_1) = \frac{MD^2}{\lambda_1^2} K_{zzzz} \quad [4.17]$$

$$RK = \frac{K(\hat{\epsilon}_2) + K(\hat{\epsilon}_3)}{2} = \frac{MD^2}{2} \left(\frac{K_{xxxx}}{\lambda_2^2} + \frac{K_{yyyy}}{\lambda_3^2} \right) \quad [4.18]$$

MK, AK and RK are expected to be increasing as long as there is on-going development of the brain, because there is a general increase in the complexity of the tissues. However, a variety of physiological mechanisms could result in the increase of complexity. A high cellular crowding that happens during inflammation for instance would contribute to increase the MK value, even though it is not a matter of development. As much as DKI brings complementary value to DTI analysis by extending the signal to a non-Gaussian distribution, the empirical representation of DWI still lacks specificity.

2.3.4. Biophysical modelling of DWI data

In order to address this issue, analytical expressions can be derived from theoretical models as a complement to tensors estimation. Models rely on assumptions about the underlying tissue and therefore provide specific parameters, whereas the cumulant expression in the Equation 4.8 is universally applicable. In the past few years, several models of neuronal tissue have aroused, with special focus on white matter characterization. Such models have common features before establishing their own assumptions [17], [77], for instance all models consist in at least two non-exchangeable compartments that represent the intra-axonal and extra-axonal spaces. Generally, what differs among the existing models is the orientation distribution function (ODF) ψ of the fibers. The ODF is a continuous distribution that represents the volume and orientation of the underlying fibers and its assessment depends on the application of interest.

One of the most popular neuronal models is NODDI (Neurite Orientation Dispersion and Density Imaging) [78], which uses a Watson ODF and includes CSF as a compartment. Thus, it requires a substantial amount of diffusion parameters that enforce the fixation of some of them. Therefore, without biological validation, the approach of fixating parameters defeats the purpose of biophysical modelling. NODDIDA (NODDI with Diffusivity Assessment) [79] has emerged to answer the requirement for simplification, suggesting the exclusion of CSF and consequently releasing the diffusivities.

Another highly accepted model in animal studies is the WMTI (White Matter Tract Integrity) [16]. This model varies from the later by analytically deriving parameters as a function of diffusion and kurtosis metrics instead of fitting the signal to non-linear equations describing the diffusion of water. In the WMTI-Watson model, represented in the *Figure 2.12*, the axons are modelled as long narrow cylinders that reproduce a highly anisotropic medium. The intra-axonal space is described by a volume fraction of water molecules f and the parallel intra-axonal diffusivity D_a . The perpendicular intra-axonal diffusivity is negligible at the relevant diffusion times, such that axons are considered to be sticks, with radius equal to zero. The bundle of axons is embedded in the Gaussian extra-axonal space that yields the parallel $D_{e,\parallel}$ and the perpendicular extra-axonal diffusivities $D_{e,\perp}$. The extra-axonal space is orientationally correlated with the fibers, whose orientation is given by the FOD-based parameter $c_2 = \langle \cos(\psi)^2 \rangle$.

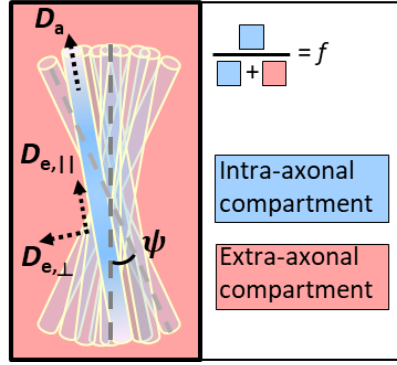


Figure 2.12: Two-compartment WMTI model providing five parameters [16].

The diffusion signal can be described in terms of both compartments, as given by the Equation 4.19. The first term represents the signal originating from a volume fraction of voxel consisting of intra-axonal tissue that is only affected in the axial direction, whereas the second term represents the signal originating from the remaining extra-axonal volume fraction $(1 - f)$ that is affected in both axial and radial directions. As the signal in each compartment is modelled by the orientation distribution, the Equation 4.19 is the integral of the fiber ODF across all directions [80], [81].

$$S(b, \hat{u}) = \int \psi(\hat{u}) \left(f e^{-b D_a (\hat{u} \cdot \hat{n})^2} + (1 - f) e^{-b D_{e,\parallel} - b (D_{e,\perp} - D_{e,\parallel}) (\hat{u} \cdot \hat{n})^2} \right) d\hat{u} \quad [4.19]$$

Taking advantage of the stable fitting of DKI, analytical expressions of tensors as functions of the model parameters can be readily found [77], [81], if assuming axial symmetry of the fiber ODF. Geometric interpretation of diffusion allows for the decomposition of the diffusivity into radial and axial directions, where $\xi = \hat{u} \cdot \hat{n}$ represents the direction and the functions h_l the moments of the fiber ODF with $l=2,4$. Each component is the sum of the diffusion in the intra-axonal and in the extra-axonal spaces in that direction weighted by the volume fraction, as shown in the Equations 4.20 and 4.21.

$$h_2(\xi) = 0: D_{\perp} = (1 - f) D_{e,\perp} \quad [4.20]$$

$$h_2(\xi) = 1: D_{\parallel} = f D_a + (1 - f) D_{e,\parallel} \quad [4.21]$$

The diffusion tensor can be represented as a function of $h_2(\xi)$ by the Equation 4.22. Using the cumulant expression in the Equation 4.8, the kurtosis tensor can be further represented in the same form as shown in the Equation 4.23. The diffusion tensor has two rotational invariants D_0 and D_2 because of the implications of axial symmetry while the 4th order kurtosis tensor has three K_0 , K_2 and K_4 .

$$D(\xi) = (1 - f) (D_{e,\perp} + h_2(\xi) (D_{e,\parallel} - D_{e,\perp})) + f D_a h_2(\xi) \quad [4.22]$$

$$D^2 K = W(\xi) = 3 \left((1 - f) (D_{e,\perp}^2 - D(\xi)^2 + 2 D_{e,\perp} (D_{e,\parallel} - D_{e,\perp})^2 h_2(\xi) + (D_{e,\parallel} - D_{e,\perp})^2 h_4(\xi)) + f D_a^2 h_4(\xi) \right) \quad [4.23]$$

Without further simplification, it is impossible to determine all 6 unknown parameters in the model $(f, D_a, D_{e,\parallel}, D_{e,\perp}, h_2$ and $h_4)$, because there are only 5 rotational invariants from the tensors. By employing a one-parameter family of axially symmetric ODFs, h_2 and h_4 contain only one common degree of freedom κ . Therefore, the Equations 4.22 and 4.23 can be solved for the 5 independent microstructural parameters. The most successful parametrization used by the WMTI model is the Watson distribution as shown in the Equation 4.24 [77].

$$p(\hat{u}) \propto e^{-\kappa(u \cdot n)} \quad [4.24]$$

Thus, the fiber ODF moments h_l are defined by p_l with $l=2,4$ as a function of κ and can be matched with the measured DWI signal. The solutions to the Equations 4.22 and 4.23 are given by the Equations 4.25-29 with the rotational invariants of D and K being defined by the Equations 4.30-34.

$$3D_0 = (1-f)(2D_{e,\perp} + D_{e,\parallel}) + fD_a \quad [4.25]$$

$$\frac{3}{2}D_2 = p_2 \left((1-f)(D_{e,\parallel} - D_{e,\perp}) + fD_a \right) \quad [4.26]$$

$$\begin{aligned} (1-f) \left(5D_{e,\perp}^2 + (D_{e,\parallel} - D_{e,\perp})^2 + \frac{10}{3}D_{e,\perp}(D_{e,\parallel} - D_{e,\perp}) \right) D_2^2 + fD_a^2 \\ = 5D_o^2 \left(1 - \frac{K_0}{3} \right) \end{aligned} \quad [4.27]$$

$$\begin{aligned} \frac{1}{2}D_2(D_2 + 7D_0) + \frac{7}{12}K_2D_o^2 \\ = p_2 \left((1-f) \left((D_{e,\parallel} - D_{e,\perp})^2 + \frac{7}{3}D_{e,\perp}(D_{e,\parallel} - D_{e,\perp}) \right) + fD_a^2 \right) \end{aligned} \quad [4.28]$$

$$\frac{9}{4}D_2^2 + \frac{35}{24}K_4D_o^2 = p_2 \left((1-f)(D_{e,\parallel} - D_{e,\perp})^2 + fD_a^2 \right) \quad [4.29]$$

$$D_0 = \frac{2RD + AD}{3} = MD \quad [4.30]$$

$$D_2 = \frac{2}{3}(AD - RD) \quad [4.31]$$

$$K_0 = MK \quad [4.32]$$

$$K_2 = \frac{1}{7} \left(3AK \left(\frac{AD}{MD} \right)^2 + 5MK - 8RK \left(\frac{RD}{MD} \right)^2 \right) \quad [4.32]$$

$$K_4 = \frac{4}{7} \left(AK \left(\frac{AD}{MD} \right)^2 - 3MK + 2RK \left(\frac{RD}{MD} \right)^2 \right) \quad [4.34]$$

In practical terms, the rotational invariants are estimated from the tensors and inputted into the system of Equations 4.25-29. The first four equations are solved analytically by expressing f and all the diffusivities in terms of p_2 and then κ is determined by solving the last equation numerically, which is related to the orientation dispersion through the Equation 4.35, with F being the Dawson's function.

$$c_2 = \frac{1}{2\sqrt{\kappa}F(\sqrt{\kappa})} - \frac{1}{2\kappa} \quad [4.35]$$

Due to the squared diffusivities in the parametrization, the system of Equations 4.31-35 has two possible solutions [16], [80], [82]: one solution corresponds to the condition $D_a < D_{e,\parallel}$ and the other fulfils $D_a > D_{e,\parallel}$. In certain neurodegenerative pathologies, both f and D_a are expected to be lower as there is damage and loss of function of the tracts. $D_{e,\parallel}$ and $D_{e,\perp}$ characterize the degree of cellular crowding and might be higher in case of inflammation or as a result of demyelination. With potential loss of structure of the fibers, there is higher orientation dispersion and c_2 is expected to be lower.

Numerous models have been developed to alleviate the downsides of both NODDI and WMTI-Watson, although they come with the expense of new parameters. The intrinsic assumptions of each model have the potential to introduce bias in the estimation of diffusion properties, but nevertheless all models indeed outperform DTI and DKI in capturing specificity and bringing new interpretations of the underlying changes of diffusivity. The choice of the model to use should have into account the purpose of the analysis since the reliability in pathological tissue needs further investigation [17].

2.3.5. Tractography

Assuming that the orientation of the largest component of the diagonalized diffusion tensor corresponds to the orientation of dominant axonal tracts in a certain voxel, DTI can provide a 3D vector field with each component representing the fiber orientation. Based on this information, it is possible to reconstruct a 3D trajectory, method referred to as tractography. Particularly, the study of white matter has been making progress due to tract reconstruction methods since there is a coherent fiber orientation within a voxel. On the contrary, isotropic gray matter anisotropy information is dominated by random noise, and therefore a single gray matter voxel may have incoherent fiber orientation.

Tractography can be performed using either deterministic or a probabilistic approaches. [83]. The most intuitive way to reconstruct a 3D trajectory from a field of fiber orientations is to propagate a line from a seed point by following the local fiber orientation at each iteration. This is the conceptual idea of deterministic approaches, also known as propagation methods, and based on which several streamline tracking techniques have been proposed over the years. In detail, seeds are placed in voxels with FA greater than a certain threshold to only include white matter voxels ($FA \approx 0.5$). These seeds grow in both directions along the dominant diffusion direction, generating streamlines according to the dominant diffusion direction in the neighbouring voxel. A streamline is terminated when it reaches a voxel with sub-threshold FA or when the turning angle exceeds a certain limit.

The first successful tractography obtained was the “connect-the-voxels” approach [84]. As voxels are discrete entities, the vector information contained in each voxel was not being fully reflected in the propagation. To overcome this issue, the vector field was turned into a continuous number field, so that the streamline could be continuously propagated rather than discretized in such a way that a streamline exits a pixel to enter the next one at a location with continuous coordinates [85]. This method is called FACT (Fiber Assignment by Continuous Tracking). Since FACT still lacked streamline smoothness, tensor interpolation was proposed by a continuous non-linear method [75] in which the principal diffusion direction was treated as the path tangent. These methods are depicted in the *Figure 2.13*.

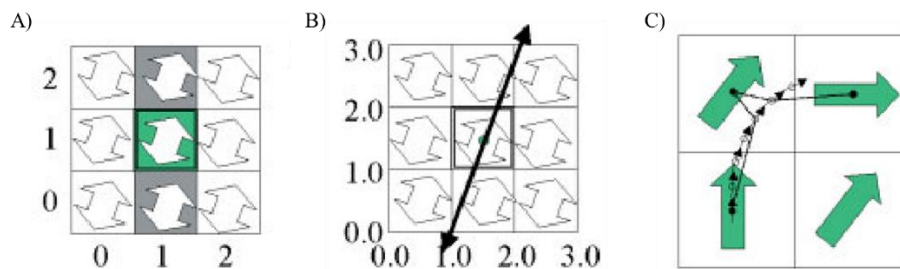


Figure 2.13: Deterministic tractography methods. A) discretized “connect-the-voxels”. B) continuous FACT. C) non-linear method [83].

Such deterministic methods are, however, susceptible to noise accumulation as the propagation of streamlines becomes longer. Although the noise effect can be reduced using smoothing, it comes with a cost in the reduction of data resolution and slows down the computation. At the millimeter scale resolution typical of DTI, the widespread divergence and convergence of white matter fascicle lead to a considerable amount of intra-voxel orientational heterogeneity. At the low b -values conventionally employed by DTI, the diffusion tensor possesses only a single orientational maxima that is its major eigenvalue. This makes it incapable of capturing intra-voxel orientational heterogeneity in the form of crossing fibers, branching issues and partial volume effect [83].

An assessment of all drawbacks of deterministic methods led to a turnaround into a probabilistic perspective of fiber reconstruction, in which a fiber orientation distribution probability function is obtained at each voxel and a streamline follows a particular path according to its likelihood [86], [87]. This is possible as long as diffusion signals can be detected with multiple discrete maxima indicating the

presence of multiple underlying fiber population. High-angular resolution, i.e. high b-value diffusion direction sampling, is therefore required in diffusion data acquisition for probabilistic tractography, as models can provide more information than the DTI-based tractography. In this way, not only this method takes into account the uncertainty of fiber orientation allowing for multiple paths, it is also more robust to noise in the sense that streamlines along noisy paths are of low probability and tend to disperse. As a result, the importance of curvature and anisotropy stopping criteria is reduced.

One of the most popular models for fiber ODF estimation is the use of spherical deconvolution [88]. In this model, the diffusion signal characteristic of each fiber population is assumed to be identical in all respects apart from their orientation. Hence, the response function from a single coherently oriented fiber population is represented as $R(\theta)$, being θ the elevation angle in spherical coordinates, relative to the z-axis. Considering that the diffusion signal emanating from different regions add independently to generate the total signal measured, this signal is given by the sum of the response functions, weighted by their respective volume fractions f_i and with a certain rotation onto the direction (θ, ϕ) represented by the operator \hat{A}_i , as shown in the Equation 4.36 [88].

$$S(\theta, \phi) = \sum_i f_i R(\theta) \hat{A}_i \quad [4.36]$$

The fraction of fibers aligned along the direction (θ, ϕ) is, in fact, its orientation density. The fiber orientation density is in fact the fiber ODF $\psi(\theta, \phi)$ and thus, differences in the ODF amplitude along a given orientation can be attributed to differences in the relative amount of fibers thought to be aligned with that direction [87]. Hence, the total signal measured can be expressed as the convolution of the response function with the fiber ODF along the direction (θ, ϕ) , as shown in the *Figure 2.14* and given by the Equation 4.37. The response function can be estimated directly from data by measuring the diffusion-weighted signal profile in regions likely to contain an oriented fiber population, i.e. where the diffusion anisotropy is higher [88], [89].

If the response function is known *a priori*, the ODF can be obtained by performing the spherical deconvolution of $R(\theta)$ from $S(\theta, \phi)$. Spherical deconvolution uses a set of spherical and rotational harmonics [90] and can be formulated as the action of an ensemble of rotations corresponding to the convolution kernel. Therefore, it can be simplified into a set of matrix multiplications through a simple linear least squares fit.

$$S(\theta, \phi) = R(\theta) * F(\theta, \phi) \quad [4.37]$$

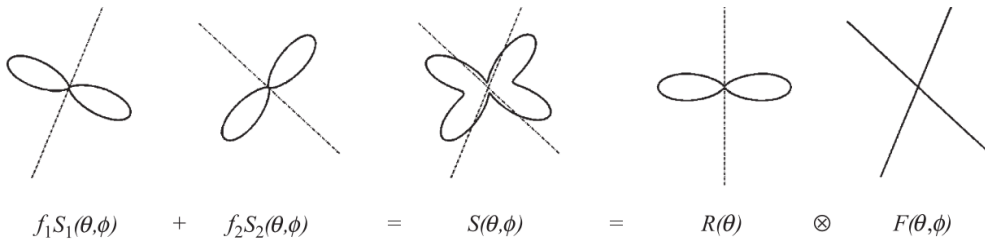


Figure 2.14: Fiber populations within a voxel with orientations (θ_1, ϕ_1) and (θ_2, ϕ_2) . The measured signal can be obtained by the convolution between the response function and the fiber ODF [88].

A potential application of spherical deconvolution of the diffusion signal obtained from high-angular resolution diffusion-weighted acquisition is to reliably reconstruct tracts in regions of crossing fibers. A successful metric proposed for voxel-wise comparison of tracts is the apparent fiber density (AFD). It reflects the relative amount of underlying axons thought to be aligned with a certain orientation in each voxel [91], grounded on information provided by the ODF.

2.4. DWI image processing

2.4.1. General image noise correction

Microstructural modelling sets a high bar on estimating signals in an unbiased way, considering that the non-Gaussian random nature of noise is very likely to bias diffusion parameters, as confirmed by the low SNR typical of diffusion data [92]. The correction of this noise-induced bias relies on an independent unbiased estimate for the noise map, that can denoise the original data. Most of the existing noise estimation methods that are able to deal with spatially varying noise patterns depend on many unrealistic assumptions such as homogeneous signal intensities. Recently, a new model-independent approach was proposed [93] based on the Random Matrix Theory. .

The elements of a random matrix are random variables from several probability distributions. The main goal of this method is to provide understanding of the diverse properties of the matrix after decomposition into its linearly independent sources with Principal Component Analysis. Since DWI data are said to exhibit redundancy, an uncorrelated basis set can be extracted as an independent source from the random matrix and characterized as noise [93]. Thus, by coupling Random Matrix Theory with Principal Component Analysis, the precise estimation of local noise in multi-directional data is possible.

This random type of noise however does not include subject motion or other physiological variations such as the breathing and the heart rates. Naturally, such periodic variations cannot be assessed with random noise approaches. One strategy to deal with it is to apply an automatic detector of outliers in the data, exclude them and refit the model without the presence of these outliers. This method is called robust model fitting and the most common algorithm is the RESTORE algorithm [94], which uses an iterative reweighted process with Monte Carlo simulations to find the outliers.

2.4.2. Image correction in EPI acquisition

Single-shot EPI is the most widely used DWI acquisition method because it is fast, efficient and insensitive to small motion [95]. As mentioned in the Section 2.2.4, the fast acquisition speed of EPI effectively freezes any head motion, maximizing the image SNR and the accuracy of diffusion measurements. Although EPI is available in most clinical MR systems, its use has certain disadvantages. First, the mechanical impacts on the holder (*tilting*) occur as a result of the gradients changing rapidly, causing vibration of the system. Moreover, according to Faraday's law of induction, a changing magnetic field in a conductor creates the so-called eddy-currents. When these gradients are applied, the eddy-currents account for distortions in the image, causing misalignments that lead to errors in the estimation of diffusion maps [96]. The images may be further warped non-linearly due to magnetic field inhomogeneities caused by non-zero off-resonance fields induced by the susceptibility field of the tissue [97]. The homogeneity level might be determined by the linewidth of the spectrum of frequencies.

All things considered, diffusion EPI images are particularly vulnerable to distortion and sources of misregistration from a combination of eddy-currents, motion and magnetic field inhomogeneities. Ideally, these should be corrected before calculating any subsequent quantitative diffusion maps. Image distortions can be reduced using bipolar diffusion-weighting schemes [98], correction with the displacement field [99], or image registration methods [96], which are mentioned in the Section 2.4.4. Bipolar diffusion-weighting schemes use two diffusion-encoding gradients with opposing polarities between the 90° and the 180° RF pulses. Both gradients induce eddy-currents that cancel out because they are inverse. As this option requires a higher TE, an alternative is to acquire an image with each of these gradients at a time. The displacement field can be calculated because distortion is imaged in opposing directions and used to correct the original image. As mentioned previously, sequence parameters selection such as increasing the number of encoding directions or the SNR improve the accuracy of DTI measures. Unfortunately, these increase the scan time and increase the partial volume effect respectively.

2.4.3. Bias field correction

One of the concerns during image processing is an undesirable low-frequency signal designated bias field that is caused by magnetic field inhomogeneities of MRI machines. This smooth signal corrupts the high-frequency content of images, blurring its edges. In addition, it changes the intensity values of image pixels, causing one single tissue to have different gray-level distributions across the image.

Applying high-pass filters was one of the first methods for correcting the bias field. Recently, approaches towards the elimination of contrast differences and the maximization of high frequency content include the expectation maximization algorithm. It divides one function that has multiple local maxima into a sequence of subfunctions each with global maxima. Thereby, this tool is applied to segmentation algorithms in order to find the most likely location of tissues and then correct for the bias field induced spatial invariance with a smoothing kernel.

2.4.4. Image registration

The aim of neuroimaging in longitudinal studies is to consistently and accurately communicate the spatial relationship within data and thus compare data across subjects, time, image types or other conditions, classify data in terms of meaningful position-dependent metrics and find patterns. These benefits are contingent on the premise that positions and sizes in one brain must correspond to positions and sizes in another brain. Determining anatomical correspondence is almost universally done by image registration, in which brains are transformed into one another or into a template. The essential components of any generic registration algorithm are transformation models, similarity measures and optimization strategies. These steps combined lead to image spatial normalization while finding the optimal transformation that maps each x of the image $I(x)$ to a location z in the image $J(z)$, such that a specified cost function $D(I, J)$, that describes the similarity between I and J , is minimized [100].

Registration algorithms can be divided into linear and non-linear, depending on the type of deformations they permit. Linear registration includes transformation models capable of performing translation, scaling, rotation and shearing. With up to 12 degrees of freedom (DOF), linear transformations globally deform an image, while preserving collinearity and ratios of distance. Particular cases of linear transformation are the 6-DOF rigid-body transformation widely used in data from the same subject or affine transformation that uses 12 DOF. With over 12 DOF, non-linear registration matches boundaries and internal structures by warping the data and allows for the local alignment between two images.

Transformations are carried out by a simple multiplication matrix of the voxels coordinates from one image to give the corresponding coordinates of another. If a voxel at coordinates x_i undergoes a transformation to the coordinates z_j , the mapping of the deformation is given by the Equation 4.38.

$$z_j = \sum_{i=0}^3 m_{ji}x_i + C_j \quad [4.38]$$

In this notation, m_{ij} with $i, j = 1, 2, 3$ specifies the respective transformation matrix. This matrix $m_{ij} = M_r$ is such that $M_I^{-1}M_rM_J$ will co-register the images I and J and define the transformation that maps the space of $I(x)$ to that of $J(z)$ [101], [102]. An additional matrix M_X should account for image dimensions, since its voxels might be anisotropic and often differ from other images. Thus, using a given interpolation method, the image is resampled according to its FOV and axis size as in the Equation 4.39.

$$M_X = \begin{bmatrix} FOV_x & 0 & 0 & Size_x \\ 0 & FOV_y & 0 & Size_y \\ 0 & 0 & FOV_z & Size_z \\ 0 & 0 & 0 & 1 \end{bmatrix} \quad [4.39]$$

3. Methods

This project aims at studying the brain microstructure of the icv-STZ rat, since this animal model has shown features typical of AD, yet it has never been assessed with MRI-derived techniques. The study required MRI data acquisition and processing for posterior statistical analysis. The study design and acquisition are explained in the Sections 3.1 and 3.2. The existing image processing pipeline is fully described in the Section 3.3 and it was primarily used to obtain preliminary results and come up with a methodology to improve it. The improvement strategies are described in the Section 3.4 and the statistical analysis is described in the Section 3.5. The strategies for additional approaches to analyse the available diffusion data are shown in the Section 3.6.

3.1. Study design

The longitudinal study of the brain microstructure in the icv-STZ rat required two study groups for comparison. Therefore, a treated (STZ) and a healthy or control (CTL) groups took part in the study and underwent an icv-injection so that all rats were under the same conditions.

The CTL group (241 ± 23 g at injection, $N=8$) was injected with a citrate buffer, while the STZ group (245 ± 17 g at injection, $N=10$) was injected with 3 mg/kg of streptozotocin. As shown in the *Figure 3.1*, each rat was scanned at four time points after injection following the ethics plan of the local Service for the Veterinary Affairs. MRI data were collected at 2, 6, 13 and 21 weeks after injection and rats were subsequently sacrificed by perfusion fixation under sedation. This euthanasia method was used to enable brain extraction and acquire histological data to support imaging results in future projects.

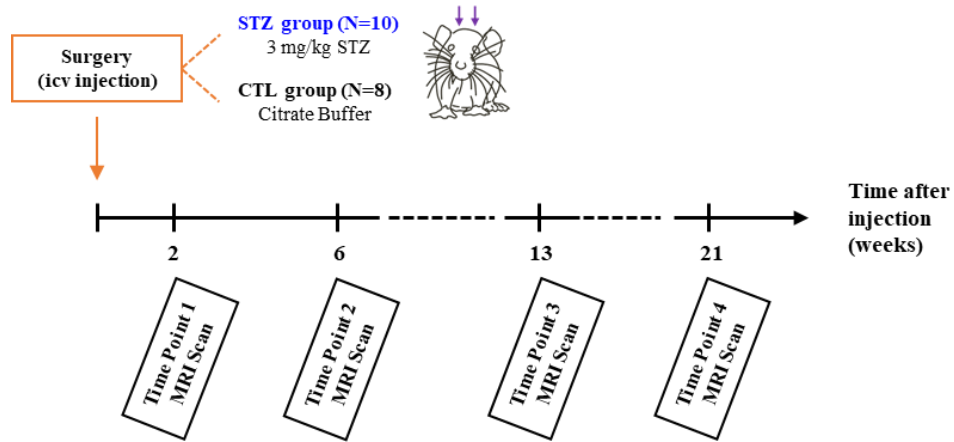


Figure 3.1: Experimental timeline of the longitudinal study.

3.2. MRI data acquisition

According to the *Figure 3.1*, each rat underwent four sessions of MRI scans. Before each scanning session, rats were exposed to isoflurane, which is an anaesthetic administered by inhalation. After sedation, rats were tightly fixated in a holder according to a very precise experimental setup while vital signs including body temperature and breathing rate were being monitored. A surface coil was placed over the head and close to the skin, in such a way that the whole brain could be captured on image. The holder was finally slid into a 14 T Varian system and the resonance frequency of the coil was fine-tuned to 600 MHz. The experimental setup is shown in the *Figure 3.2*.

Moreover, the power of the RF pulses was calibrated to obtain a 90° excitation pulse at the desired depth from the brain surface, and the magnetic field was adjusted to be as homogeneous as possible, especially around the regions of interest (ROIs) of the study. The optimization of field homogeneity is

called *shimming* and it consists in changing electric currents that create new magnetic fields that when summed up with B_0 make the total magnetic field homogeneous in each direction. The shimming algorithm was performed in three steps, in which more directions were evaluated consecutively, so that the susceptibility distribution could be compensated for. Shimming was repeated whenever rats might have undergone vibration and moved from the original location, as often occurs in EPI acquisitions.

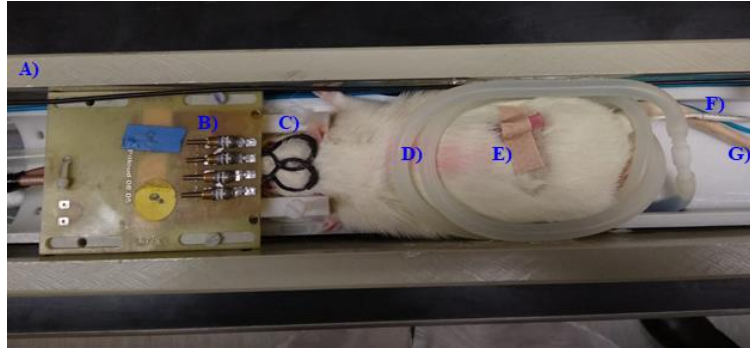


Figure 3.2: Experimental setup for the MRI scan. A) rat holder. B) capacitors for adjustment of frequency by tuning and matching procedure. C) superficial rat head coil. D) water tubes for body temperature adjustment. E) sedation injection. F) anal thermometer. G) breathing sensor.

Each scanning session comprised three acquisition protocols to obtain anatomical, diffusion and resting-state functional MRI (rs-fMRI) images. Diffusion assessment was the primary focus of this project, while rs-fMRI data was processed and analysed within the ambit of another project. The outcomes of that analysis are briefly elucidated in the Chapter 5 as they support microstructural results.

The anatomical images were T2-weighted and since they were only used for spatial localization and not quantitative purposes, the scanning time was reduced by using a fast spin-echo sequence, with $TE/TR = 10.17/3000$ ms, $matrix = 128 \times 128$, $FOV = 19.2 \times 19.2$ mm³, $voxel\ size = 0.15 \times 0.15$ mm³ and 30 slices with 0.5 mm thickness.

The diffusion protocol was performed with a semi-adiabatic spin-echo EPI acquisition. The sequence included the following parameters: $TE/TR = 48/2500$ ms, $matrix = 128 \times 64$, $FOV = 23 \times 17$ mm³, $voxel\ size = 0.18 \times 0.27$ mm³ and 9 slices with 1 mm thickness in $NR = 4$ repetitions. Data were acquired in three different shells and a total of 62 measurements, as shown in the Figure 3.3, provided that at least 21 measurements with at least 2 non-zero shells were required for regression of tensor estimation, as explained in the Section 2.3.3. Four $b = 0$ ms/ μm^2 (b_0) images, i.e. with no diffusion weighting, were acquired as well. Another shell with $b = 0.8$ ms/ μm^2 was acquired in 12 directions, $b = 1.3$ ms/ μm^2 in 16 directions and lastly $b = 2$ ms/ μm^2 in 30 directions.

In order to make up for the distortions caused by eddy-currents in the processing pipeline, two short b_0 images were acquired with opposing gradients each, *linear* and *reverse linear*.

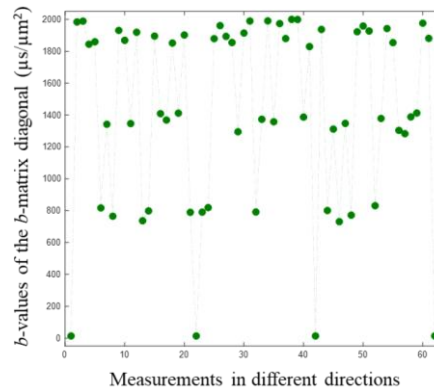


Figure 3.3: Plot of the b-values acquired in a total of 62 directions in one of the repetitions.

3.3. Existing image processing pipeline

The existing image processing pipeline is herein described. It includes all the processing steps taken towards the quantification of diffusion in the white matter. Several stages were included in order to correct images in terms of noise and MRI-induced artefacts and to enable the comparison across datasets. Diffusion was assessed in four ROIs within this project by calculating diffusion and kurtosis tensors and estimating the WMTI-Watson model.

3.3.1. Data reconstruction and brain extraction

Anatomical and diffusion data were reconstructed automatically in the Varian system, being only necessary to convert them into a common file type for additional processing. Since one of the most conventional formats to represent neuroimaging information is the NIfTI (Neuroimaging Informatics Technology Initiative), the *Tools for NIfTI and ANALYZE image* from Matlab were used for conversion into .nii images. The reconstructed anatomical (A) and diffusion images are shown in the *Figure 3.4*, with the later including the images resulting from the linear (B) and reverse linear (C) acquisition directions. The differences are mainly evident at the bottom of the brain, where structures seem more compressed in the linear direction and more stretched in the reverse linear. This difference allows for the estimation of the displacement field and distortion correction, as treated in detail in the next section.

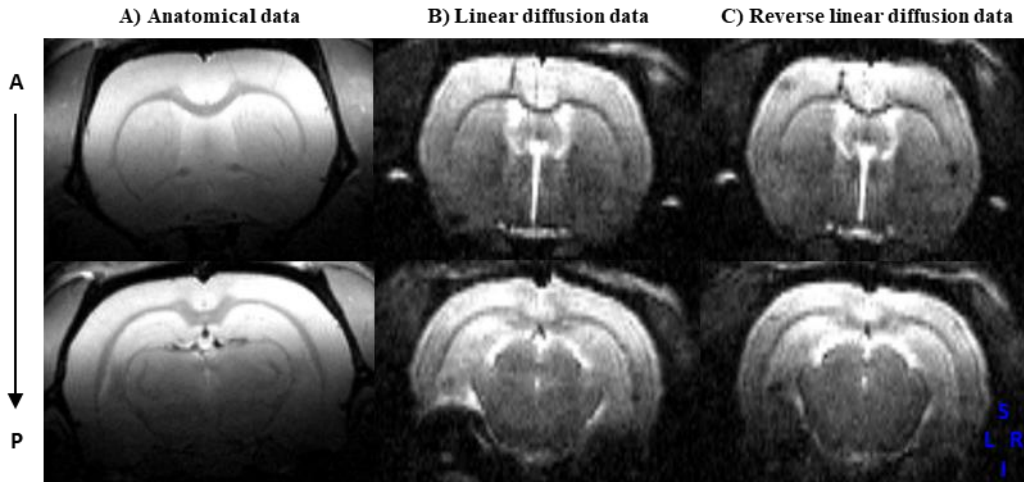


Figure 3.4: Reconstructed MRI images in each modality (column) in two coronal planes (rows).

Following reconstruction, a mask was created to extract only brain tissue from data to be used in the subsequent stages of the pipeline. Thus, brain extraction refers here to the separation between brain and non-brain tissue. In the initial pipeline, the brain was extracted manually from anatomical and diffusion data using MRIcron [103], by carefully drawing the contour of the brain and filling in the inside of the outline. The drawn mask (A and C) and the extracted brain (B and D) of anatomical and diffusion data are shown in the *Figure 3.5*. It is important that brain extraction precedes bias field correction and registration so that when accounting for the intensity distribution or the parcellation of the brain, external regions such as fat or muscle are not included.

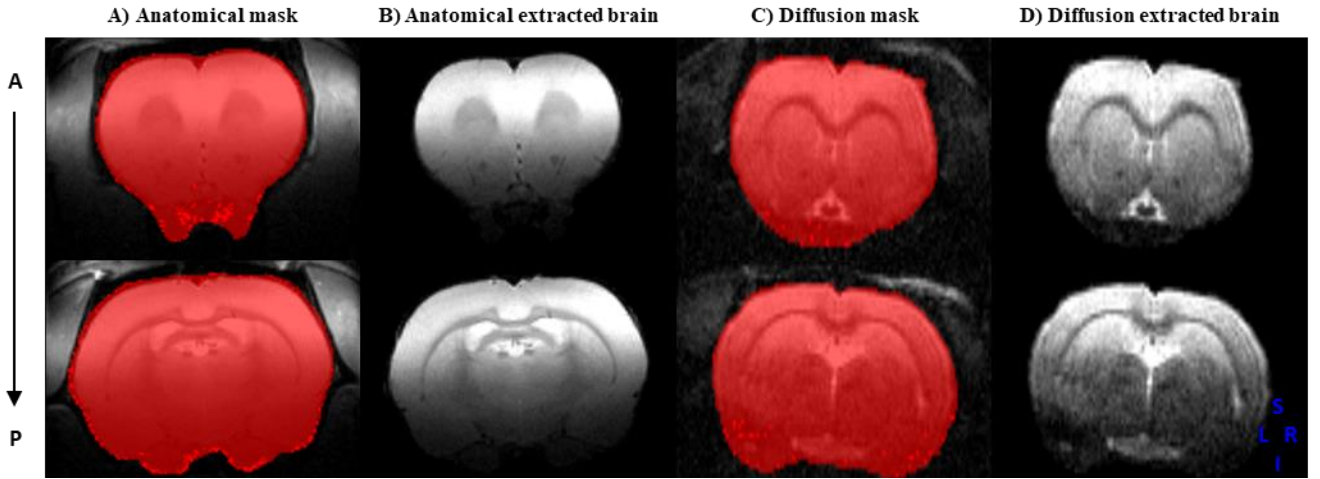


Figure 3.5: Manually drawn masks of the brain and resulting extracted brains in anatomical and diffusion data in two coronal planes (rows).

3.3.2. dMRI data correction

After reconstruction and brain extraction, data underwent corrections for quality improvement and reliability of quantitative measures. Measurement repetitions were averaged and diffusion images were firstly denoised using the method of the Random Matrix Theory and Principal Component Analysis coupling [93]. A data matrix with Marchenko Pascur distribution was generated and Principal Component Analysis eigenvalues were computed in the extracted brain. Each image was then associated to a noise map, SNR map and the denoised version of the brain.

After random noise minimization, specific EPI distortions were minimized as well. The *topup* function of FSL estimated the susceptibility field by finding when the similarity of the unwrapped images was maximal, using the sum-of-squared differences [104]. Therefore, linear and reverse linear acquisition directions datasets were used to correct the displacement distortions of the main image caused by magnetic field inhomogeneities. In the same context, the *eddy* tool from FSL [105] was helpful as it separated the offset eddy-current field from motion and aligned the different weighted images. A comparison between the original unedited diffusion data (A), denoised (B) and distortion corrected data (C) is shown in the *Figure 3.6*. From A) to B) the correction of random noise is evident with the denoised image being “cleaner” and with brain structures better delineated. From B) to C), differences are clear in terms of the ringing that was induced by motion and non-brain tissue is entirely removed from data at this stage.

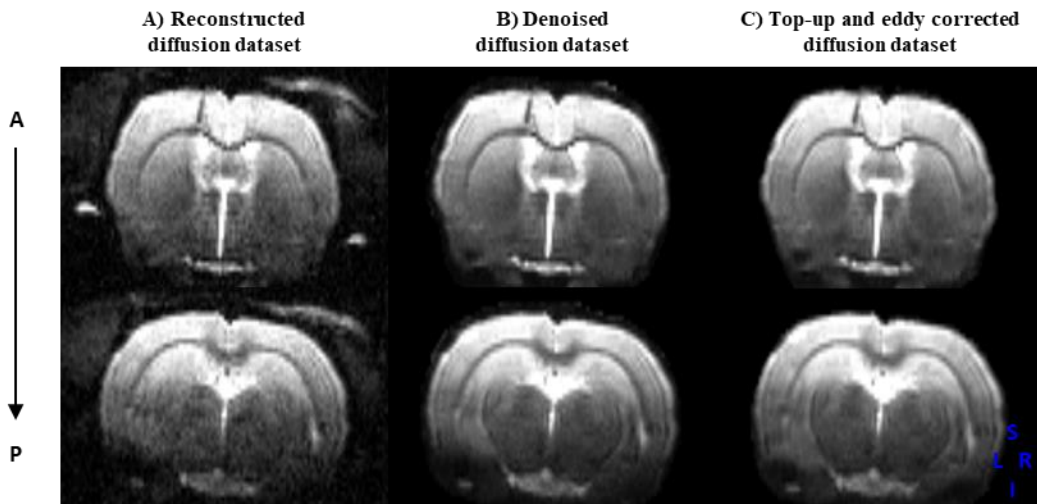


Figure 3.6: Sequential steps of diffusion data correction in two coronal planes (rows).

3.3.3. Spatial normalization of anatomical MRI data for co-registration

In this project, anatomical data were acquired merely to provide spatial information of brain structures in the diffusion space, rather than to perform any morphometric analysis. A robust concept of location was required so that explicit estimation of diffusion measures could be done over certain regions of the brain known to be affected in AD and can be compared across datasets, between study groups and time points. Hence, anatomical images were registered to a template so that diffusion and anatomical data could be posteriorly co-registered.

Instead of creating a template by averaging anatomical data, an available high-field MRI unbiased standard space template image, designated Waxholm Space (WHS) [106] was used to align anatomical datasets to. An available 255-tissue segmented atlas provided by the Minimal Deformation Template (MDT) [107] was transformed into the same space to be further used as the parcellation template of the rat brain. The template anatomical image A) and atlas B) are shown in the *Figure 3.7*.

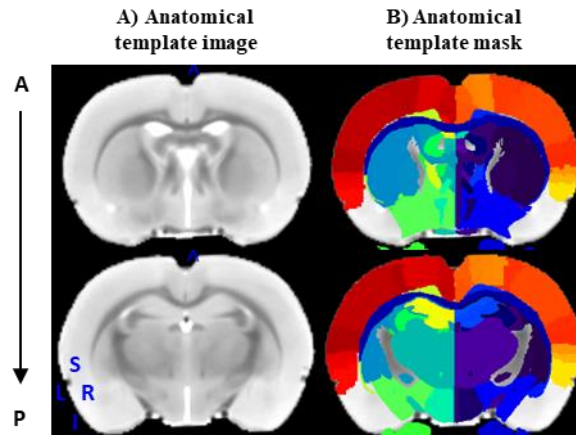


Figure 3.7: WHS template space where anatomical data were registered to.

All anatomical datasets were aligned to the anatomical template using affine transformation followed by higher DOF non-linear registration (T_{A2T}), so that non-localized rotation, translation and scaling occurred, as well as local warping. FSL tools were used in this regard, such as FLIRT (FMRIB's Linear Registration Tool) [108], [109] and FNIRT (FMRIB's Non-linear Registration Tool) [110]. Affine registration was estimated with the *mutual information* cost function, 12 DOF and trilinear interpolation; whereas non-linear registration used with the affine transformation matrix as the starting estimate for initial alignment, warp resolution of 1 mm in all directions, a cubic spline, a smoothing Gaussian kernel, a non-linear model for intensity mapping, 5 iterations in each direction and a final linear interpolation.

The purpose of registration in this pipeline was not to align all datasets in the same stereotaxic space, but to align the template atlas in each single dataset space and obtain brain parcellation. The inverse warping matrix ($T_{A2T}^{-1} = T_{T2A}$) of the non-rigid registration was calculated, allowing for the transformation of the template space into the anatomical space of each dataset, using the FSL function *invwarp*.

3.3.4. dMRI data registration and segmentation

In order to obtain an atlas aligned to diffusion data, each diffusion dataset was transformed into the respective anatomical data space (T_{D2A}) using the same affine parameters aforementioned. The function *convert-xfm* from FSL allowed for the estimation of the inverse transformation matrix ($T_{D2A}^{-1} = T_{A2D}$), which was further convoluted with the inverse warping matrix previously estimated (T_{T2A}). This operation was performed by the FSL function *applywarp* using the nearest neighbour method to interpolate the integer values of the atlas, finally obtaining a map in the diffusion space of each dataset. The registration methodology aforementioned is shown in the *Figure 3.8*.

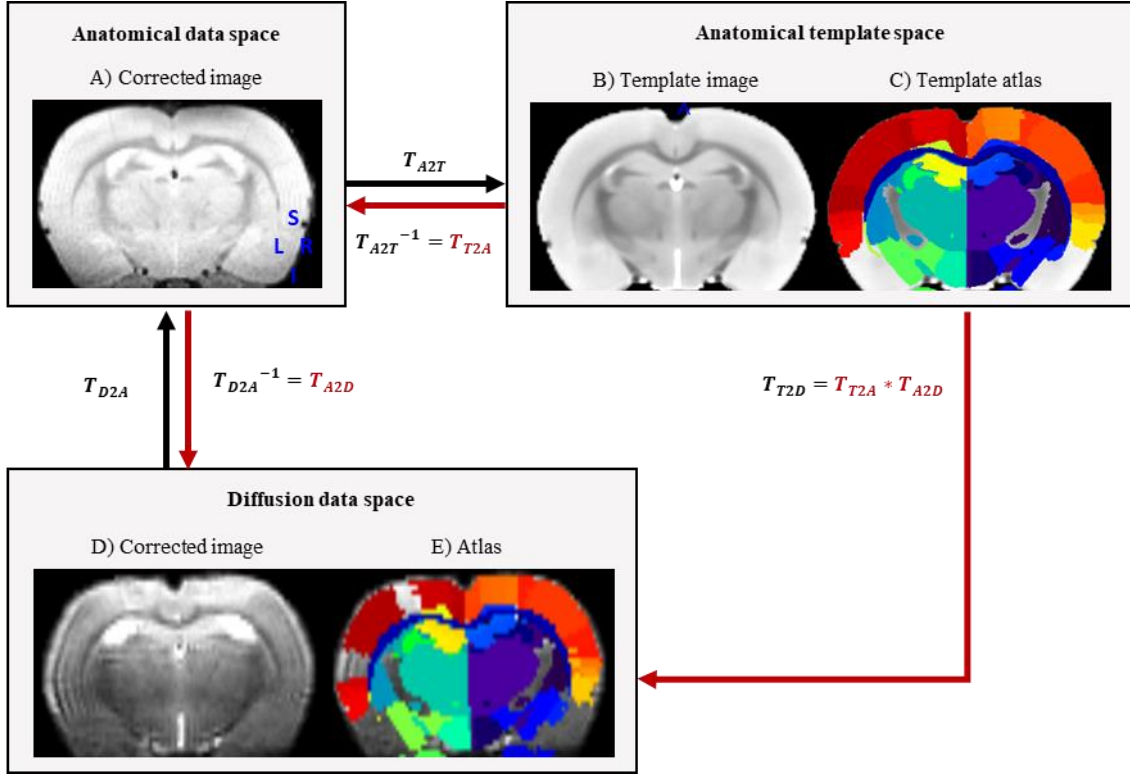


Figure 3.8: Schematic representation of the registration procedure. Anatomical data in A) was registered into the template image B) so that the deformation field from the template space to the original anatomical space could be calculated. Diffusion data in D) and anatomical data in A) were co-registered so that the deformation field from the anatomical space to the diffusion space could be calculated. Finally, the transformations from the template space to the anatomical space and from this to the diffusion space were convoluted in order to calculate the transformation of the atlas in the template space C) to the diffusion space and obtain an atlas E) for each diffusion dataset.

From the diffusion-transformed atlas, white matter regions known to be involved in AD, according to previous findings in human studies [35], [57] and in the icv-STZ animal models [8]–[10], [12], [20] were extracted. The tracts selected to characterize white matter were the corpus callosum, the cingulum, the fimbria and the fornix and each one was transformed into a binary mask such that diffusion parameters were estimated specifically in these ROIs. Tracts are represented in the Figure 3.9.

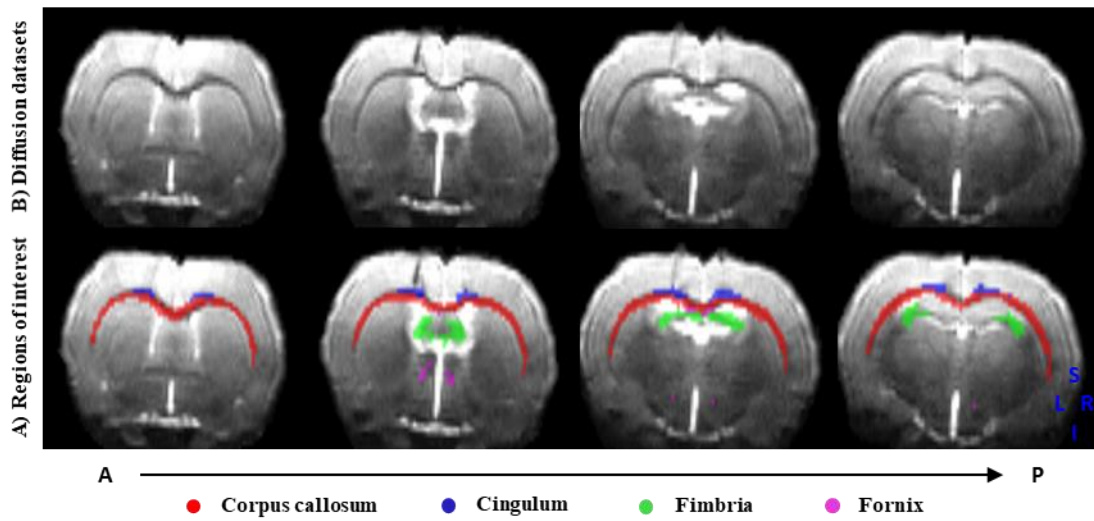


Figure 3.9: White matter ROIs in different coronal planes (columns). In A) ROIs are represented as binary labels and B) is the original diffusion data where labels are overlapped.

3.3.5. Diffusion and kurtosis tensors estimation

Following denoising and distortion correction, unbiased diffusion data were used to estimate tensors and its measures using Matlab. First, the b -matrix initially extracted from the acquisition parameters was loaded and DTI was estimated with the weighted linear least squares estimator, according to the simplified cumulant expansion Equation 4.9 [111]. The eigenvalue decomposition was performed because the metrics chosen for this study were invariant metrics of diffusion [23]. Thus, the metrics MD, $A_{\perp}D$, RD and FA were calculated in each voxel from the Equations 4.12-15, respectively.

In non-Gaussian DKI, the cumulant expansion was used without any prior assumptions (Equation 4.8) and the kurtosis tensor was obtained using the same estimator [111], where the several diffusion shells and multiple directions allowed the fitting of the tensors [70], [71]. The metrics MK, AK and RK from the Equations 4.16-18, respectively, were calculated in each voxel to complement DTI information [14]. Therefore, DTI and DKI estimation provided altogether seven parametric maps of the whole brain shown in the *Figure 3.10*, where different contrasts result from the way scalar values are calculated from the tensors and thereby provide different information.

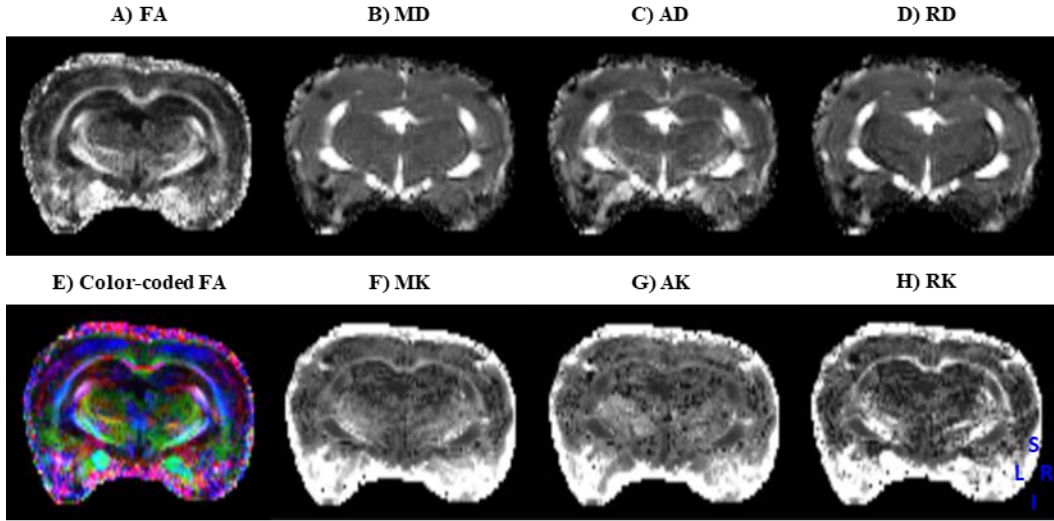


Figure 3.10: Parametric maps of DTI and DKI quantitative metrics.

Tensor models take into account certain types of noise such as thermal noise or magnetic field inhomogeneities, but not others, such as physiological noise that is seen as motion inside the scanner. Since EPI acquisitions have such high sensitivity to motion, an automatic detector of outliers was used to refitting the model estimation, so that the effects of the breathing and the heart rates present in data were excluded from the estimation. The RESTORE algorithm [94] was used and the noise map previously obtained in the denoising phase was provided for the initial iteration of the reweighted process. The outlier voxels were therefore removed subsequently from the fit in an attempt to remove artefacts that were not removed earlier in the processing pipeline.

In order to avoid potential outranged values in these parametric maps, a filter was applied before statistical analysis. Unphysical values were caused by artefacts unable to be removed from data and more importantly by partial volume effect. When a voxel labelled as white matter was capturing regions of the gray matter or CSF it caused, for instance, MD to be much higher, because those are isotropic regions. This issue is further addressed in the Section 3.4.4. Considering this, the filtering condition consisted in only including in the analysis voxels with values within the expression in the Equation 5.1. All these conditions characterize white matter in terms of scalar values.

$$F_{WM}: 0 < RK < 10 \wedge 0 < MD < 2.5 \wedge 0 < MK < 2 \quad [5.1]$$

3.3.6. Estimation of the WMTI-Watson biophysical model of the white matter

As to provide specificity to the diffusion analysis, a model of the white matter was estimated and yielded complementary measures [17]. The WMTI-Watson model is one of the most well-established existing models at the moment because it relies on DTI and DKI measures and does not depend on unstable non-linear fitting of parameters [16], [77]. Therefore, WMTI-Watson was estimated on Matlab, where tensors metrics were loaded to further calculate the rotational invariants of D and K as given by the Equations 4.30-34. The solutions were obtained with the Equations 4.25-29 using the Matlab tool *fsolve*, that was fed with D_0, D_2, K_0, K_2 and K_4 , the option of 5000 iterations and an initial guess of parameters $x_0 = [f_0, D_{a0}, D_{e,\parallel 0}, D_{e,\perp 0}, \kappa_0] = [0.35, 2.5, 0.85, 0.75, 5]$.

Its output was then the series of five parameters $f, D_a, D_{e,\parallel}, D_{e,\perp}$ and κ , and c_2 was calculated using the Equation 4.35. The mathematical solution $D_a > D_{e,\parallel}$ was here retained based on recent evidence [82]. Since *fsolve* solves systems of non-linear equations with several variables, it is extremely time-consuming. To reduce the amount of time spent to obtain these parametric maps, the system was not solved over the whole brain data, but only over the ROIs. The parametric maps obtained after model computation are shown in the *Figure 3.11*, where scalar values are only given for ROIs.

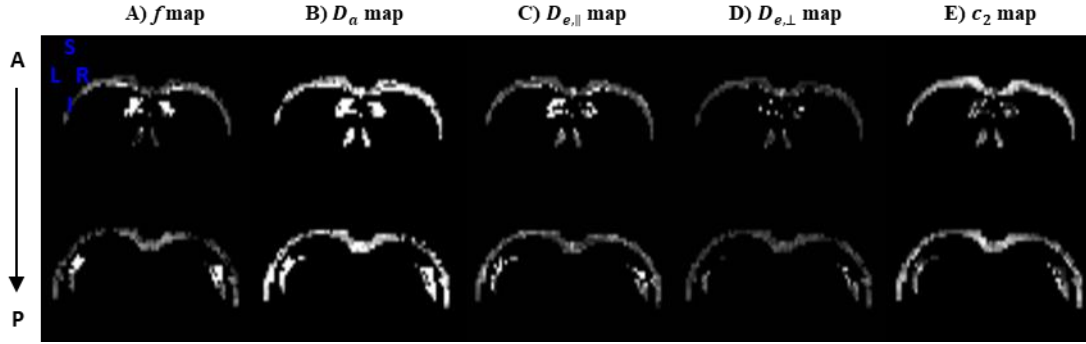


Figure 3.11: Parametric maps of parameters resulting from the WMTI-Watson model in two coronal planes (rows).

Due to the risk of divergence of parameters during the fitting, a filter was applied to the 5 parametric maps provided by the WMTI-Watson model. Voxels were only kept for statistical analysis under the condition stated by the Equation 5.2. It forced all voxels to have a set of parameters within a biophysical acceptable range of values. An example of a filtered map is the *Figure 3.12* and shows that a great deal of voxels is clearly outside of the range of vales required. This issue is addressed in the Section 3.4.5.

$$F_{WMTI}: 0 < f < 1 \wedge 1 < D_a < 3 \wedge 0 < D_{e,\parallel} < 3 \wedge 0 < D_{e,\perp} < 3 \wedge \frac{1}{3} < c_2 < 1 \quad [5.2]$$

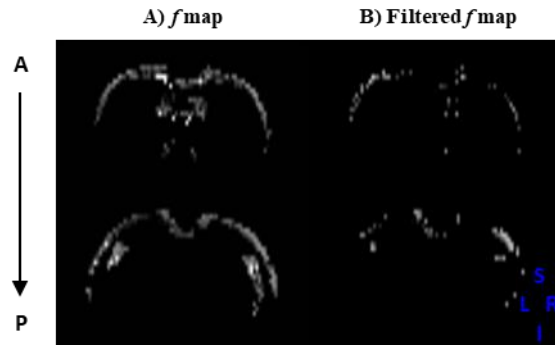


Figure 3.12: Parametric maps of f before (A) and after the filter F_{WMTI} is applied (B) in two coronal planes (rows).

3.4. Optimization strategies to the existing pipeline

The improvements proposed to the existing processing pipeline are herein described. To understand how to optimize the pipeline, preliminary results were obtained in the first part of the traineeship using the methodology described in the Section 3.3. From speeding up some stages of the existing pipeline to improve data quality, subprojects were developed in the second part of the project. Each of the subsequent sections is one optimization strategy, whose results are shown in the Section 4.1. If these results were satisfactory, strategies were implemented in the existing pipeline and the statistical analysis was computed considering the adjustments made.

3.4.1. Improvement of white matter labels in the template atlas

The existing 255-label 300-slice template atlas was initially developed for gray matter analysis and white matter tracts were not quite properly represented. Namely, the external capsule, corpus callosum and cingulum were represented as a single tissue, structures in general were not fitting in with each other with several voxels having the value “0”, some of the labels did not match exactly the tissue in the underlying anatomical image and some of them were missing. Since the aim of this project is to assess the white matter microstructure, additional care was taken with image-label correspondence.

Therefore, the methodology to improve the existing template atlas in terms of white matter regions consisted in manually redrawing these structures slice-by-slice when overlaid onto the anatomical template image using ITK-SNAP [112]. This hands-on methodology was based on the extensive information collected from the Data Portal of the Allen Brain Atlas ©. In this way, there would be less partial volume effect and diffusion metrics in each ROI would be more reliable. The differences between the original and the latest version of the improved atlas were evidenced by subtracting one from the other using ImageJ.

3.4.2. Semi-automatic brain extraction

Manual brain extraction was one of the most time-consuming steps in the pipeline considering that, for each dataset, a brain mask was drawn in 30 anatomical slices and 9 diffusion slices. Since over 45 datasets were to be processed in the course of this project, finding a solution for this issue was naturally one of the first concerns. The most obvious solution consisted in the automatization of the process using specific algorithms for brain extraction that usually generate meshes to model the brain surface. While there are several tools for extracting the human brain, only few of them apply to rodents. Three tools were considered to meet the requirements to be used in this pipeline and replace manual work: the bet2 (brain extraction tool) from FSL and the 3dSkullStrip and 3dAutomask from AFNI (Analysis of Functional NeuroImages). Since only the latter is suitable for EPI data, bet2 and 3dSkullStrip were tested in anatomical data, whereas 3dAutomask was tested in diffusion data as follows.

Bet2 generated a binary brain mask by iteratively expanding and deforming its initial tessellated mesh until enveloping completely the brain, according to several dynamic controlling parameters [113]. In turn, AFNI’s 3dSkullStrip [114] was adapted from bet2 and included a new set of processing operations more specific anatomical-wise. The expansion of the spherical surface was improved by a 3D edge detection tool, tools to avoid clipping of frontal areas and to reduce leakage into the skull and the adjustment of features to rat data. Choosing between both tools was solved essentially by trial and error. First, each tool was applied to an anatomical dataset with the default settings. After trying different controlling parameters, neither of the two tools appeared to be sufficiently good. In the end, the best combination of parameters was achieved with the application of the 3dSkullStrip followed by intensity normalization. The tool was set up with 250 iterations, defining the mesh density, an intensity threshold of 0.1 and nearest neighbour interpolation followed by final smoothing using the Taubin’s method.

Concerning diffusion data, the advantage of the 3dAutomask from AFNI of accepting 4D (3D+time) EPI data compromised its robustness by not generating an iteratively expanded mesh. Instead, the largest components of the supra-threshold voxels were kept after erosion-dilation procedures. The intensity threshold in 3dAutomask was brain size-dependent and varied between 0.4 and 0.65. A dilation step was applied afterwards with a 3D kernel of a 3x3x3 box centered on the target voxel to compensate for the intensity drop at the bottom of the brain. In consequence, the dilation was equally applied on top of the brain, which is closer to non-brain tissues, possibly overlapping fat or muscle tissue. To understand how impactful overlapping could be, metrics were computed after following the entire processing pipeline described in the Section 3.3 using an unsupervised dilated mask in one dataset. The parametric maps were visually compared with the ones obtained with the manually drawn mask.

3.4.3. Bias field correction

Before registration, it is a common procedure to remove the bias field signal and uniformize the intensity distribution across the image that has suffered variations induced by MRI inhomogeneities during the scan. Here, the use of a surface coil induced a gradient in the signal's amplitude of images that was a function of depth from the coil placed above the cortex. It explains the brighter signal in regions closer to the coil and the darker signal in regions further. By correcting the induced-bias, the subsequent steps are not affected by corrupted voxel values.

Since the correction of the bias field in anatomical data was not included in the pipeline, it was one of the optimization strategies. Bias field correction was performed after brain extraction, because otherwise the algorithm would account for other tissues to normalize the overall intensity. It was performed by the FSL tool FAST (FMRIB's Automated Segmentation Tool) that uses a hidden Markov random field associated to the expectation maximization algorithm [115]. Visual evaluation was carried out.

3.4.4. FA atlas-based registration of dMRI data

In neurodegenerative diseases there is frequently enlargement of the brain ventricles over time, even though the nature of this process remains unclear. On the one hand, inflammation could cause the obstruction of the intraventricular foramen, which allows the CSF to reach the brain ventricular system, and the gradual reduction of CSF drainage. On another hand, the degeneration of hypothalamic cells could result in the caving in of tissue, leading to the taking over of CSF over the free space left [10].

In consequence, it is common to be faced with a disease group with greater ventricle sizes than the CTL group, which constitutes a problem in terms of registration because regions around the ventricles of the disease group are shifted uncontrollably [116]. This issue affected this project and caused ROIs to be misaligned in the diffusion data. The registration approach failed to spatially normalize the structures around the oversized ventricles, especially the fimbria, as can be seen in the *Figure 3.13*.

Misalignment naturally affected diffusion metrics because the tissue-label correspondence was no longer accurate. For instance, considering that water diffusion within the ventricles is isotropic, FA is much lower in the ventricles ($FA \approx 0.1$) than in the white matter tracts ($FA \approx 0.5$). Thus, partial volume effect of white matter tracts with CSF would have a lower average FA and generally a suboptimal sensitivity to true differences in tensors. Accordingly, preliminary results showed that partial volume effect was reflected as group differences in FA in the fimbria unlikely to correspond to true differences.

Several studies have in that regard tried to find ways to guarantee that registration was successful both in resolving topology variability and exact alignment of the very fine structures. Although manual edition of atlas labels is a helpful approach in particular situations, an automatic solution must be achieved for larger amounts of data in order to be an unbiased, efficient and low time-consuming process. Approaches including affine alignment of DTI maps across datasets [117], extreme DOF non-linear registration [118] or tractography-based registration [119] have been proposed, but failed.

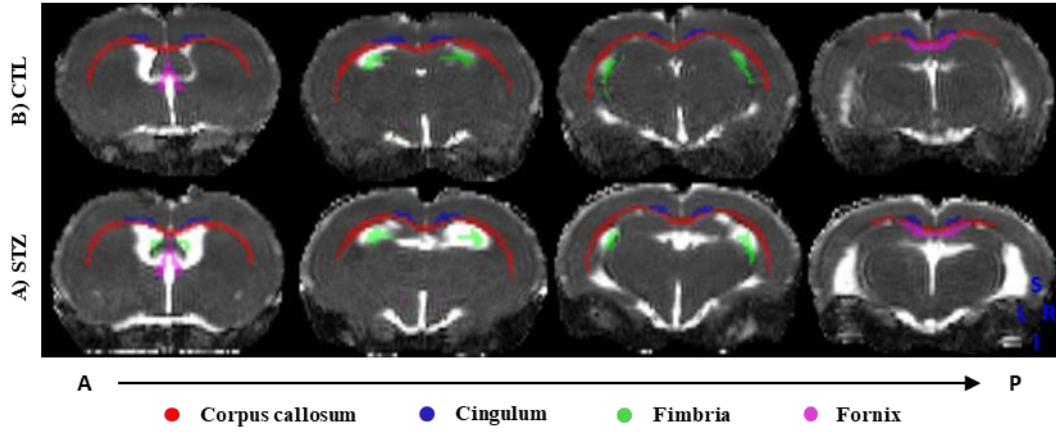


Figure 3.13: Comparison between STZ (A) and CTL (B) rat brain ventricles at 13 weeks after injection in different coronal planes (columns).

A newly attempt to overcome all these flawed approaches is called tract-based spatial statistics (TBSS) [120]. It aims to solve the alignment and smoothing issues, while being fully automated and without requiring pre-specifications of tracts of interest. This is achieved by projecting the FA map from each dataset onto a *mean FA skeleton* in such a way that each skeleton voxel takes the FA value from the nearest relevant tract center. FA was proposed because it is computable voxel-wise and a vastly used marker for tract integrity with scalar values independent of the local fiber orientation [118]

In this project it was not reliable to create a skeletonized mean FA, since in this longitudinal study, ventricles become larger over time. Hence, an FA template image was used instead. An FA template was available in the template WHS, i.e. the same stereotaxic space as the template atlas [106]. Taking into consideration the TBSS method, FA data was registered into the FA template, replacing the conventional anatomical registration described in the *Figure 3.8* in the Section 3.3.4. The inverse transformation was calculated and co-registration between diffusion and with FA data was carried out, so that the template atlas was transformed into each diffusion dataset space. Naturally, this diffusion-transformed atlas was different than the one obtained after anatomical registration, because the dataset/template image correspondence of FA data and anatomical data is also different.

While FA reveals differences across space, it does not reflect any information regarding direction. On the contrary, CCFA maps are direction-dependent as they visualize each x (CCFAx), y (CCFAy) and z (CCFAz) diffusion directions separately by reading the coordinates of the largest eigenvalue. Hence, the procedure described above was also tested with a CCFA template image and CCFA data in each direction. The different template images are shown in the *Figure 3.14* and compared to the respective corrected diffusion parametric maps.

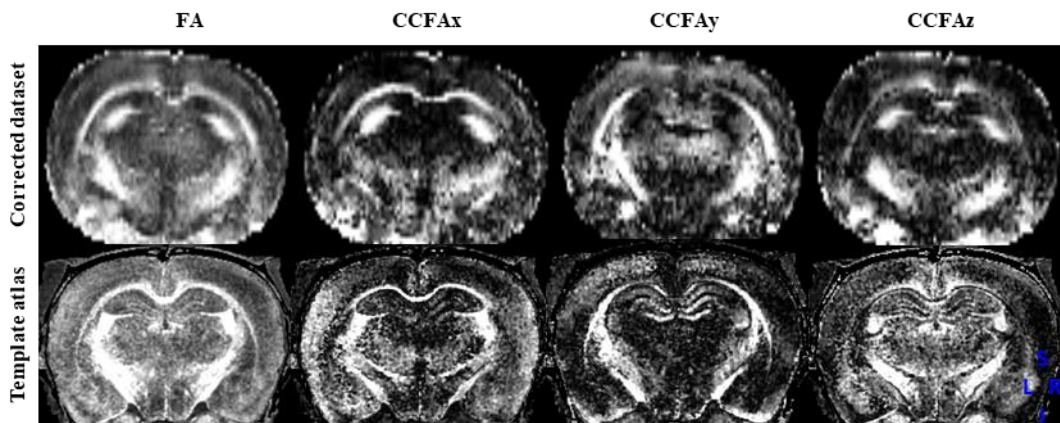


Figure 3.14: Different parametric maps (columns) obtained from the pipeline (upper row) and the respective images available in WHS template space (lower row).

In order to evaluate the best registration procedure, a quality measure was defined. Since the outcome of registration in this project was the labelled atlas, the best way to quantify the misalignment of each procedure was to calculate the tensors metrics over the ROIs extracted from those atlases and apply the white matter filter F_{WM} given by the Equation 5.1. The ratio R between the number of voxels filtered by the white matter cut-off and the total number of voxels of each ROI partially determines how much the white matter label is aligned to the underlying tissue, since the filter excludes voxels that contain CSF.

This ratio is given by the Equation 5.3 and the higher it is, the less voxels are being excluded from image analysis and the less voxels are overlapping the ventricles. However this ratio does not quantify partial volume effect with gray matter regions. During registration, while different transformations try to *push* away the labels from the ventricles, they might force such distortions that the labels end up being *pulled* into the gray matter, which is concerning as well. Since it was too restrictive to narrow down the values of the diffusion metrics to exclude gray matter, visual inspection was always required.

$$R = \frac{\text{Number of voxels kept after } F_{WM}}{\text{Total number of voxels}} \quad [5.3]$$

In a total of 30 (14 CTL and 16 STZ) datasets, linear and non-linear registration between FA, CCFAx, CCFAy and CCFAz data was performed. Diffusion metrics were calculated over the ROI labels extracted from each resulting atlas and finally, R was estimated for each ROI in each dataset. It was averaged in CTL and STZ groups for each registration procedure and compared between each other and with the conventional anatomical registration procedure. Statistical analysis of the diffusion metrics was computed using the labels resultant from the best method chosen for each ROI, using the statistical tests described in the following Section 3.5 where p -values were compared. The ultimate goal was to understand whether alignment of tissue-label correspondence was significantly impactful for data analysis. If existing significant differences between and within groups were improved to a more powerful statistical significance (lower p -values), the misalignment caused by oversized ventricles would be minimized and the respective registration procedure would be integrated into the pipeline to obtain the final results.

3.4.5. Evaluation of the initial values in the WMTI-Watson model

After estimating WMTI-Watson model parameters, the filter in the Equation 5.1 was applied to ensure that only biologically acceptable values participated in the statistical analysis. However, it was noticed in the *Figure 3.12* that a substantial amount of voxels were being filtered out in that process, with an average of $58 \pm 4\%$ of voxels being removed from analysis. This means that these results were not entirely reliable and, in addition, tensors and model metrics were being averaged out in fairly different ROIs. In this case, the outranged values could not have been caused by partial volume effect due to misalignment of structures, because the excluded voxels had unphysical parameter values regardless containing white matter, gray matter or CSF. In fact, this could be an issue with the model fitting while solving the system of Equations 4.31-35.

In order to understand what was causing the model to fail in so many voxels, only one option could be changed within the model estimation. Thus, retaining the mathematical solution $D_a > D_{e,\parallel}$, different initial values were tested. If the model was diverging because of the starting estimates, other combinations of starting values would provide parameters within the filter conditions. Since the model estimation was one of the most time-consuming steps in the pipeline, only two voxels were selected to undergo model fitting: one voxel where the model has worked and another from the same dataset where the model has failed. The selected voxels are shown in *Figure 3.15* where f has not been properly estimated in the “unfitting” voxel.

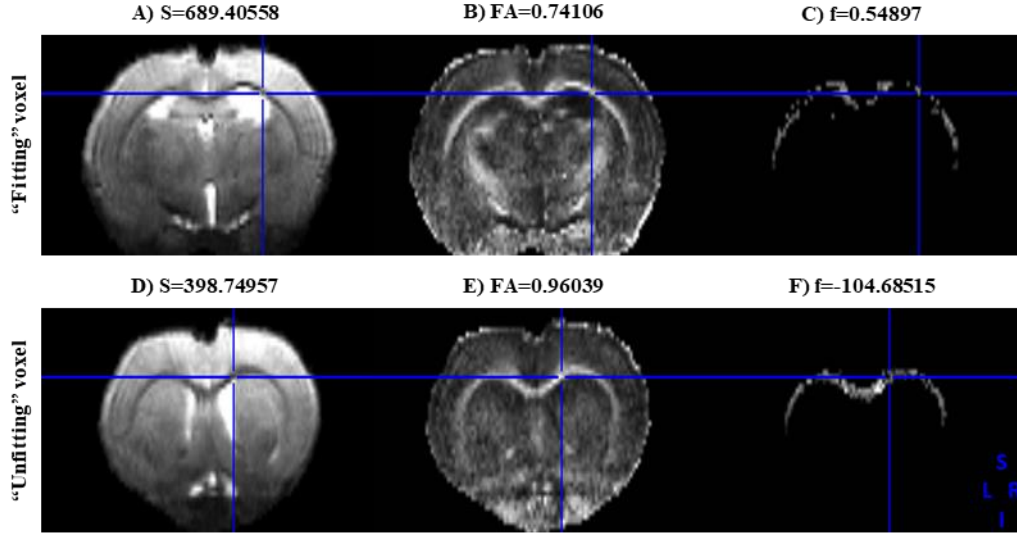


Figure 3.15: “Fitting” (upper row) and “unfitting” voxels (lower row) capturing the corpus callosum in three different representations (columns): corrected diffusion image (A and D), FA parametric maps (B and E) and f parametric maps (C and F).

For a deeper understanding, multiple initial values for each parameter were selected to produce different combinations at each iteration within a nested *for* loop. These included $f_0 = [0.1:0.2:0.9]$, $D_{a0} = [0.4:0.6:2.8]$, $D_{e,\parallel 0} = [0.4:0.6:2.8]$, $D_{e,\perp 0} = [0.3:0.4:1.9]$ and $\kappa_0 = [1:2:11]$. Each iteration corresponded to a different set of initial values and for each, a set of parameters was calculated in each voxel. Histograms were produced for each parameter after all combinations, with a sample of $5^4 \times 6 = 3750$ iterations.

3.5. Statistical analysis of diffusion metrics

Taking all data into consideration, a 4D data matrix was ultimately obtained to compute statistical tests. Either for health reasons or data corruption, not all data acquired were eligible for analysis. From the 18 (10 STZ + 8 CTL) rats that underwent injection, 1 (STZ) died before the 2 weeks assessment, and 2 (1 STZ + 1 CTL) were sacrificed before the 21 weeks assessment because of weight loss. One poor quality STZ dataset at 6 weeks was excluded because of a problem with the coil during the scanner. In addition, several datasets were excluded from the analysis because of incorrect acquisition. 2 STZ and 2 CTL datasets at 2 weeks were discarded, as well as other 2 STZ and 2 CTL datasets at 6 weeks and at 21 weeks. Since 8 (4 STZ and 4 CTL) rats were not scanned at 21 weeks in time for the statistical analysis of this project, a total of 45 datasets were included in the tests to be described. The reformulated experimental timeline with all datasets included in the analysis is presented in the Figure 3.16.

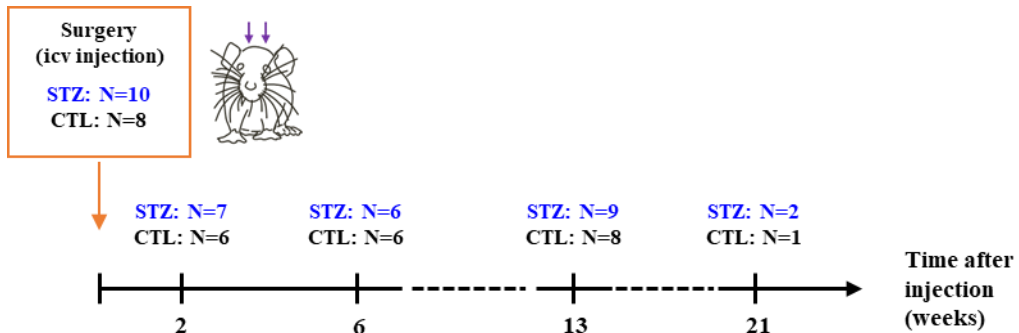


Figure 3.16: Updated experimental timeline with the datasets included in statistical tests. Due to poor data quality or health reasons, some rat brains could not be included in all time points.

Unfortunately, at 21 weeks after injection the sample of datasets was not statistically powerful and these three datasets were not included in the tests. Nevertheless, these datasets were included in the visualization boxplots to provide the tendency of values in the last time point.

Statistical analysis approaches were explored considering that this project aims to address white matter microstructure in two different manners: how STZ rats evolve over time, compared with CTL rats, and how both groups differ at each moment in time. Thus, two different statistical tests were carried out in Matlab. The mean and standard deviation values of each of the 12 metrics were averaged over each of the 4 ROIs labels for each dataset. Study groups and time points were averaged so that statistical tests to compare the means in different populations were computed. At each time point, two-tailed t -tests were computed to evaluate the differences in the mean of each metric and in each ROI between groups. The null hypothesis was that the STZ and the CTL groups at each time point came from independent random normal distributed samples with equal means at a 5% significance level. Within each group, a one-way ANOVA assessed the variance in the mean of each metric and in each ROI over the experimental timeline. The null hypothesis was that the samples at 2, 6 and 13 weeks of each group were drawn from populations with the same mean at a 5% significance level.

3.6. Additional diffusion analysis strategies

In addition to the strategies proposed to optimize the existing pipeline, two new approaches to analyse the available data were proposed as well. The strategies proposed are described in the subsequent sections and aim at complementing the statistical analysis of the diffusion metrics with new spatio-temporal information that would ideally support the results obtained from the Section 3.5. Both these approaches were developed from scratch and were carried out with the intention of being the starting point for new projects.

3.6.1. Gray matter analysis for correlation with white matter metrics

Gray matter atrophy has been a reported manifestation of AD, alongside with white matter degeneration, in several icv-STZ rat studies [8]–[10]. A study has shown that white matter degeneration is an intermediate event between early amyloid deposition and late gray matter atrophy [121]. However, it remains unclear what trigger white matter degeneration and whether this is immediately anterior to gray matter atrophy or they are independent.

Even though a mathematical model for gray matter is lacking, gray matter microstructure can be evaluated with DTI and DKI. In order to disclose the spatio-temporal relationship between white matter degeneration and gray matter atrophy, tensors metrics were averaged over gray matter regions: ACC, RSC, hippocampus, PPC and MTL. These regions were selected according to their functional association with white matter ROIs and to the existing literature [8]–[10], [12], [20]. Labels are represented in the *Figure 3.17*, where the connection between gray matter and white matter ROIs becomes clear. The mean DTI and DKI metrics in the gray matter were averaged by study groups and time points.

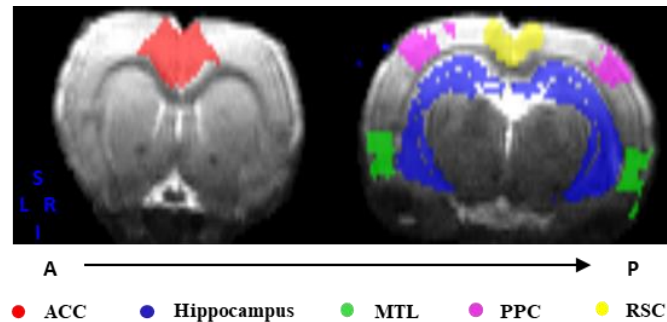


Figure 3.17: Gray matter ROIs in two coronal planes.

In the preliminary results, the diffusion metric that showed more significant differences across all white matter ROIs was the MK. Therefore, MK in the white matter ROIs was studied as a function of the MD in the gray matter ROIs, because this metric is the easiest to predict in such an isotropic medium. Among all the ROIs selected herein, diffusion alterations in the cingulum were expected to be related to alterations in the RSC and the ACC, alterations in the corpus callosum to alterations in the PPC and the MTL and alterations in the fornix and fimbria to alterations in the hippocampus. Thus, scatter plots of the variables were computed between the ROIs potentially related. For instance, the MK in the cingulum was plotted against the MD in the RSC and so on for the other five relationships. These relationships were studied in two ways: variables were divided into time points across all study groups and into study groups across all time points. Except for the datasets at 21 weeks after injection across time points, all datasets were included in the gray matter analysis.

The preliminary results have shown that white matter degeneration was reflected by low MK values in the STZ group. This would be related to gray matter atrophy in ROIs firstly affected by AD, such as the hippocampus. In the CTL group the opposite would be expected. Gray matter atrophy is supposed to be translated into high MD and structural development is characterized by low MD. The separation of the scatter plots into time points would ideally characterize the temporal degeneration.

3.6.2. Tractography for quality assessment of metrics

Tractography is one of the most widely used techniques to study the brain connectome because of its ability to assess its microstructure. However, the idea of this subproject was to take advantage of available data. The goal was to reconstruct tracts corresponding to the ROIs of this project and to obtain metrics from them. Tractography-derived metrics were expected to have a spatio-temporal pattern similar to the diffusion metrics, that would confirm the reliability of the reconstructed tracks. According to the literature, constrained spherical deconvolution of FODs is a better solution than DTI-based tractography, since it minimizes image noise and resolves crossing fibers, as long as there is high b -value diffusion direction sampling [88]. Hence, due to the comprehensive tutorials available, MRtrix 3.0 tools were used to perform spherical deconvolution of diffusion data.

Since this subproject was an experiment and occurred at the end of the traineeship, there was no time to include more than 8 (4 STZ and 4 CTL) datasets. Preliminary results showed that at 6 weeks after injection, study groups showed almost no differences, whereas at 13 weeks there were numerous differences between groups. From each time point, 2 datasets belonging to each group were selected and were included in the tractography processing pipeline, that was developed from scratch. Evidently, results were not statistically powerful but, nevertheless, a tendency could already be perceived.

Even though diffusion data were already corrected, tractography required isotropic data before computing FODs in order to improve software performance. Images were then upsampled to their minimum voxel size, $0.18 \times 0.18 \times 0.18 \text{ mm}^3$, using the MRtrix function *mrresize*. As ROI labels were used as seeds, atlases were upsampled as well. The first stage of spherical deconvolution was to estimate the response function $R(\theta)$ for each dataset, based on diffusion signals and gradient information. The *tournier* algorithm was used within the *dwi2response* tool of MRtrix as it combines the provided b -values and directions to improve angular resolution [122]. The FOD function $F(\theta, \phi)$ was then estimated by spherical deconvolution as given by the Equation 4.37. For this purpose, response functions and the diffusion data were inputted in the *dwi2fod* tool of MRtrix to calculate spherical harmonics coefficients [123].

An FOD dataset is shown in the *Figure 3.18* and accurately represents tracts directions. The body of the corpus callosum is shown in the x-direction, the external capsule in the y-direction and the cingulum in the z-direction. Moreover, the fimbria is imaged in pink which means that its tracts are oriented in the x- and z-directions to meet the fornix in the midline of the brain. The random arrow directions in the ventricles further confirms the accuracy of the estimated FOD.

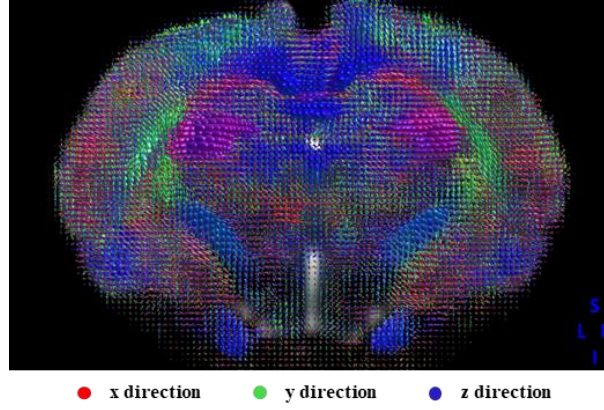


Figure 3.18: FOD dataset represented with arrows that characterize the fiber orientation. Orientation is defined by arrow color and FOD magnitude by arrow size.

To compare datasets, correspondence between FODs was necessary [89]. All FOD datasets were used to create a study-specific unbiased FOD template with the MRtrix function *population_template*. To build the template, all datasets were considered representative of the population, even though clear differences arose in the ventricles size of the STZ group, as previously shown in the Figure 3.13. This tool used each FOD dataset to output the deformation field that transforms a specific dataset into the general template. These warps were afterwards used to spatially normalize FOD datasets and transform them into the new template space. The same warp was applied to masks, labelled atlases and to the diffusion-weighted images as well, for visualization purposes. Transformations were enabled by the MRtrix function *mrtransform* [89]. Registration outcomes are shown in the Figure 3.19.

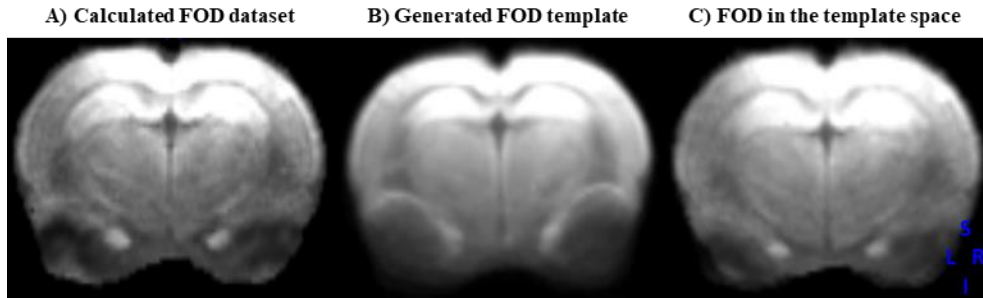


Figure 3.19: Registration of FOD datasets (A) to a template generated from original data (B). In C) the FOD datasets was transformed into the generated template space.

To finally achieve 3D reconstruction, MRtrix provided a tool with multiple algorithms available, named *tckgen*. From algorithms using deterministic methods such as FACT or path-integral methods, to different choices of probabilistic methods, the tool enabled the generation of streamlines and provided user-controlled parameters. The algorithm chosen was the iFOD2 that allowed for smoother streamlines with a 2nd order integration [124]. Here, a streamline was more probable to follow a path where the FOD amplitude was large whereas it may rarely traverse orientations where the FOD was small.

Four different local tractographies were computed with each ROI label as a seed. The seed could be instead selected as a set of coordinates, which would not be ideal for an automated process for a larger sample. The remaining parameters, such as the number of streamlines, the step size, the FOD amplitude cutoff for terminating tracks and the minimum length of streamlines, were chosen based on a trial-and-error approach, which was conclusively ROI-dependent. The algorithm seeded streamlines randomly within the given label mask until the desired number of streamlines was reached, as long as other criteria met the parameters inputted.

Following tracks generation, a good track isolation required tracking editing techniques that use region masks to include or exclude streamlines from the tractogram. In practical terms, using *tckedit*

MRtrix tool, inclusion regions and exclusion regions were defined, displaying all streamlines that traverse inclusion regions and excluding any streamlines that traverse exclusion regions. Although it is a knowledge-based technique, unwanted contributions can be reduced by placing more seeds. Naturally, editing tracks depends on the ROI as well. While the corpus callosum had such a great amount of fiber connections and requires more filtering, the cingulum was much straighter forward to isolate. The more the branching patterns and orientations a region shows, the more difficult it is to isolate it from other regions inherently associated anatomically. In this case, manual intervention was necessary.

With each tract of interest well defined, it was possible to compute statistics on the streamlines included. *mrstats* from MRtrix provided a histogram of the lengths of each streamline of each tract. Even though streamline-based metrics were limited to the parameters selected in the track generation process, they apply equally to all datasets and thus, they were relatively unbiased. Additionally, AFD was finally estimated for each tract, using the *afdconnectivity* function from MRtrix.

Length of streamlines and AFD were averaged for each track of interest for each dataset. A plot of the average AFD divided by the average length of streamlines were computed for each track of interest, including all 8 datasets. The AFD was normalized because the datasets of the different time points were not the same rats. The normalized AFD was expected to decrease in the STZ group over time because of white matter degeneration confirmed by the microstructural results, and to be constant or to increase in the CTL group. In addition, at each time point, AFD would be higher in the CTL group than in the STZ group.

4. Results

This chapter is divided into the Section 4.1 that describes the results obtained from testing the pipeline optimization strategies; the Section 4.2 that describes the final results from the statistical tests, computed after applying the successful optimization procedures to the existing pipeline; and the Section 4.3 that describes the results from the additional analysis strategies. In fact, the Sections 4.1 and 4.3 describe how the final longitudinal study was improved in terms of reliability and reproducibility.

4.1. Optimization strategies to the existing pipeline

The alterations proposed to the existing pipeline are described in detail in the Section 3.4 and the way they affect the processing pipeline is herein described quantitatively or by visual inspection. Several times the subprojects relied on the preliminary results to evaluate the potential improvements. Once these improvements were verified and considered an additional value to the analysis, the methodology was integrated in the pipeline described in the Section 3.3. For each strategy proposed, a final statement declares whether the methodology was implemented in the existing pipeline.

4.1.1. Improvement of white matter labels in the template atlas

After manually changing the 255-label template atlas, the final version had 276 tissues and more accurate white matter regions. The before (A) and after states (B) of the template atlas are shown in the *Figure 4.1*. The mathematical difference between both (C) is equivalent to the overall changes made.

In the anterior slice of the original rat brain template atlas, red arrows show voxels without an assigned label. The improvement consisted in filling in these voxels, especially near white matter regions, such as the internal capsule and the fimbria (arrow on the left hand-side) and the corpus callosum, cingulum and the RSC (arrow on the right hand-side). The blue circle evidences the separation into cingulum and corpus callosum, that have led to important findings as different tracts in previous studies [8], [9], [19], [34]. In the posterior slice, red arrow points at one of the several new labels drawn, namely the hippocampal fissure. The blue circle shows the separation between corpus callosum and external capsule, which is different from the human brain and often confounded.

Main changes were made on the corpus callosum and fimbria. The improved template atlas allowed for an improved atlas in the diffusion space of each dataset and thereby more reliable labels of the ROIs. Ultimately, diffusion metrics were less affected by partial volume effect and became more representative of the microstructure. This new template atlas was therefore integrated in the registration pipeline.

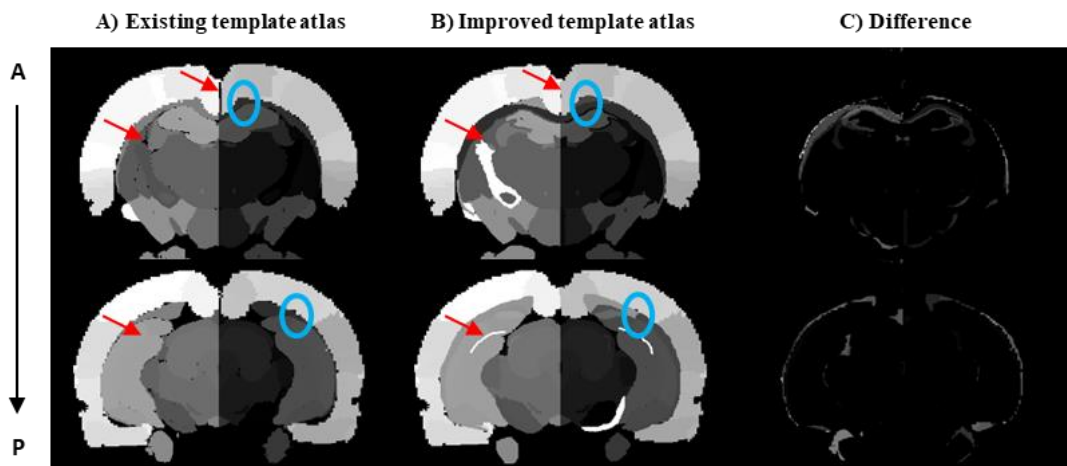


Figure 4.1: Differences between the initial and improved template atlas with particular focus on the white matter regions in two coronal planes (rows). Red arrows and blue circles highlight the main differences between both.

4.1.2. Semi-automatic brain extraction

For anatomical extraction of the brain, bet2 and 3dSkullStrip software were evaluated by trial and error and the different stages of the optimization method are represented in the *Figure 4.2*. The first column corresponds to the whole head anatomical image and the second and third columns correspond to the extracted brain resulting from bet2 and 3dSkullStrip tools, respectively.

In the first attempt to use these tools, data were unedited in terms of intensity or distortion correction. Both tools showed a poor segmentation of brain tissue in the inferior part of the brain, possibly caused by an accentuated drop in the signal from top to bottom since the coil was placed on top of the head. In order to improve the signal in the inferior portion of the brain, the gross variability in intensity distribution was removed and tools were tested using the corrected image. Their performance showed that whereas bet2 was extracting muscle tissue above and laterally, 3dSkullStrip was clipping too much the edges. Conversely, bet2 was able to envelop the bottom of the brain, while 3dSkullStrip stopped the surface expansion in the midline of the brain.

All results considered, it was more important to remove non-brain tissue, as evidenced by the blue circle than to capture the spinal trigeminal tracts, pointed out by the red arrow. Therefore, the 3dSkullStrip performance was more appropriate in this case and indeed reduced the time consumption in this pipeline stage. It was integrated in the pipeline after image reconstruction.

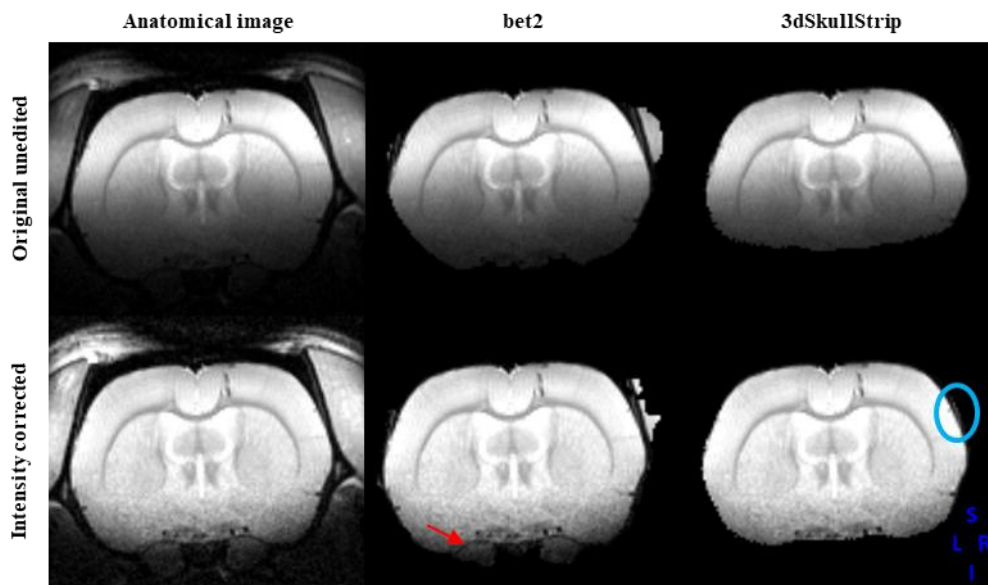


Figure 4.2: Comparison between two different tools (columns) for brain extraction before (upper row) and after (lower row) intensity correction of anatomical data. The red arrow and blue circle represent the advantages of the corresponding tool.

Regarding brain extraction in diffusion data, the 3dAutomask tool was tested, as shown in the *Figure 4.3*. The original unedited diffusion image of one rat at 13 weeks after injection is represented in A). The most significant parameter in this tool was the intensity threshold level (thr) and thus, three increasing threshold levels in B), C) and D) showed a gradual removal of the head tissues around the brain (blue circles), at the expense of a poor extraction of the bottom of the brain.

To make up for this, an increasing amount of dilation steps were used, in E), F) and G) with the highest threshold level (thr=0.65). Apparently, it improved the extraction of the bottom of the brain, while keeping less non-brain tissue than lower threshold levels. When compared with the manually obtained extracted brain in H), both images seem reasonably similar (green circles), except for the presence of a thin layer of non-brain tissue around the extracted brain.

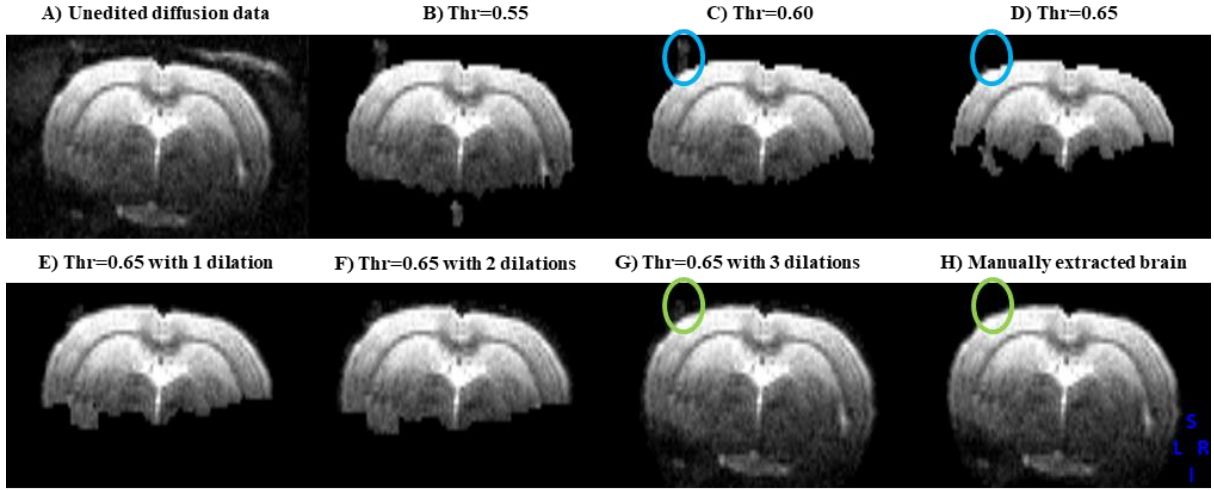


Figure 4.3: Comparison between different parameters for the brain extraction in diffusion data. The circles represent the main differences between parameters.

To understand how impactful the layer resulting from unsupervised brain extraction (thr=0.65 and 3 dilation steps) can be, the image in G) underwent all the processing pipeline described in the Section 3.3. until tensors metrics were calculated. The Figure 4.4 shows the comparison between the denoised eddy-corrected images (A and B) and the MK parametric map (C and D) resulting from the pipeline computed the manually edited mask and the mask from G).

In the corpus callosum, different values of the diffusion signal in the exact same voxel were found using both masks, which means that noise and distortion corrections accounted for the voxels outside the brain to normalize the diffusion image. This had an effect in DTI and DKI measurements, with a difference in MK of roughly 0.18, which is highly significant considering the usual differences in MK between groups and time points within a ROI.

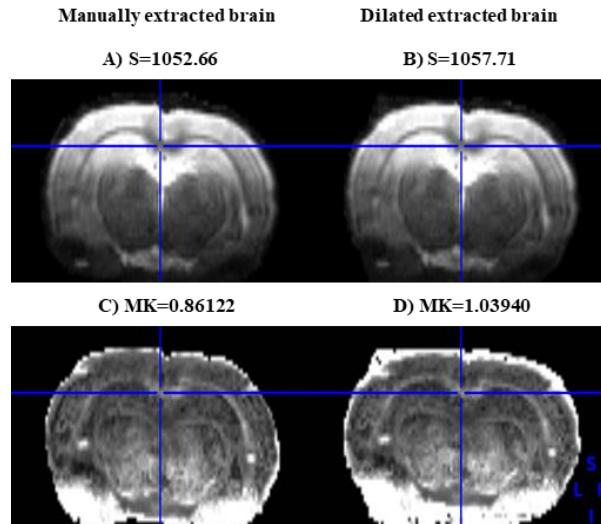


Figure 4.4: Comparison between manual extraction and the 3dAutomask tool with thr=0.65 and 3 dilations in the corrected diffusion signal (upper row) and the MK parametric map (lower row) in the corpus callosum.

Therefore, for this method to be integrated into the existing pipeline, there was still need for post-processing of the extracted brain, to ensure the head tissues were removed from the analysis and the parametric maps were as reproducible as possible. It was still less time-consuming to combine the 3dAutomask tool with thr=0.65 without dilation and manually fill in the bottom of the brain. As seen in D) in the Figure 4.3, there was no overlapping of non-brain tissue on top of the head. This semi-automatic approach was therefore implemented in the existing pipeline.

4.1.3. Bias field correction

The difference between the original unedited anatomical image (A) and the bias field corrected image (B) is represented in the *Figure 4.5*. In the original anatomical data, it is clear a gradient of signal attenuation as a function of distance from the coil, i.e. less signal in the bottom of the brain. In turn, the corrected image shows deep brain structures with similar intensities to the cortex. With a better contrast between structures in both anterior and posterior planes, this additional step affected positively the registration and therefore was integrated within the existing pipeline.

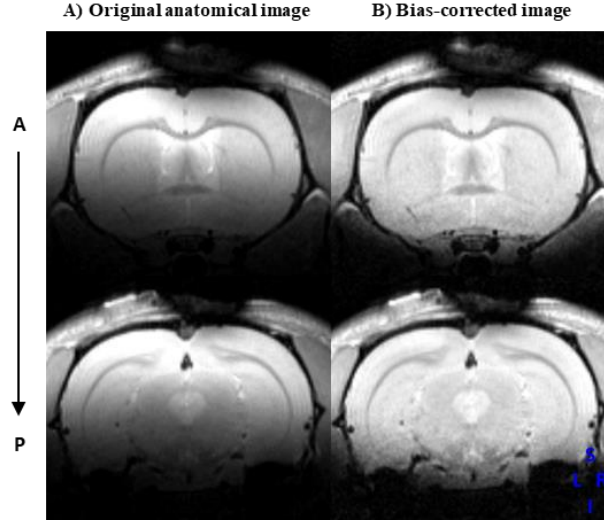


Figure 4.5: Difference between the original anatomical image and after bias field correction in two coronal planes (rows).

4.1.4. FA atlas-based registration of dMRI data

As an attempt to minimize the effects of enlargement of ventricles in the metrics, the registration procedure was repeated with different image modalities for posterior diffusion co-registration and compared with the standard anatomical registration used by the existing pipeline for each ROI. In the first stage of this strategy, only linear registration was computed to compare four different methods (FA, CCFAx, CCFAy and CCFAz linear registration) between them and with anatomical registration. The average ratio of voxels kept in each ROI after the white matter filter is shown for each method in the *Table 4.1* for CTL and STZ rats, being R a measure of the alignment between labels and the underlying structures. A higher ratio means a lower amount of voxels that contain CSF and therefore a potentially better alignment. In the *Figure 4.6* the differences between methods are shown for each ROI.

R		Anatomical Registration	Linear Registration			
			FA	CCFAx	CCFAy	CCFAz
CC	STZ	0.9537	0.9517	0.9489	0.9662	0.9195
	CTL	0.9743	0.9765	0.9763	0.9830	0.9626
CG	STZ	0.9937	0.9961	0.9976	0.9980	0.9678
	CTL	0.9906	0.9941	0.9964	0.9994	0.9800
Fimbria	STZ	0.6650	0.7073	0.7506	0.6879	0.7683
	CTL	0.8834	0.9055	0.9330	0.8748	0.9167
Fornix	STZ	0.9625	0.9640	0.9609	0.9604	0.9515
	CTL	0.9485	0.9668	0.9603	0.9705	0.9563

Table 4.1: Average R calculated after 5 different linear registration procedures for each ROI in each study group. CC: corpus callosum, CG: cingulum.

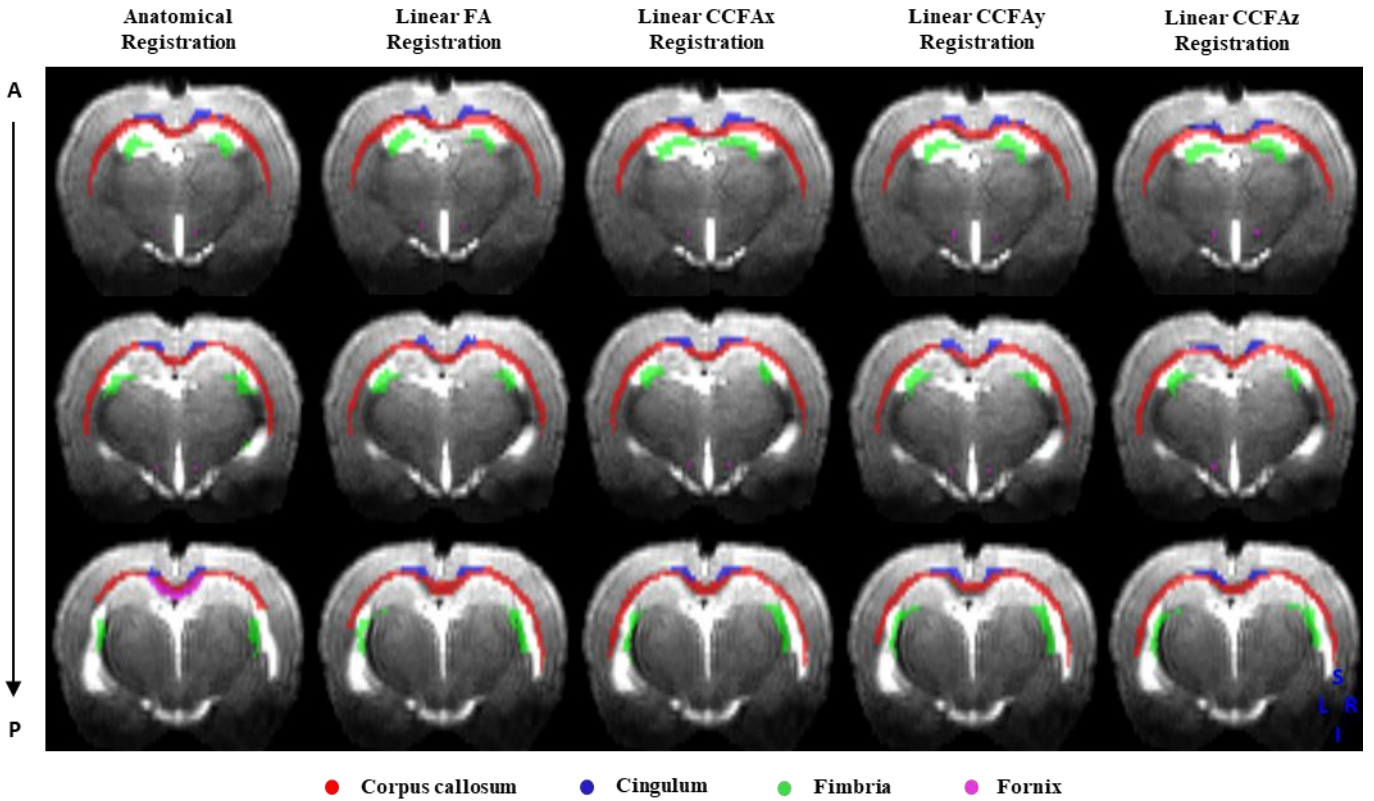


Figure 4.6: Comparison between the ROIs extracted from atlases resulting from different registration procedures (columns) in a STZ dataset in three coronal planes (rows).

The cingulum was the ROI whose voxels were generally less excluded after filtering and the one with less differences between CTL and STZ groups throughout all methods. Even though CCFAy was the best linear registration method for both study groups, the ratio difference between CCFAy and anatomical registration was only 0.4% in the STZ group and 0.8% in CTL group. Thereby, since the cingulum was barely affected by partial volume effect, there was no need to change the protocol in this case.

The fornix did not change considerably from one method to another, with the highest ratio difference of 1.3% between methods in the STZ group. The best apparent methods at pushing the fornix label out of the CSF were the linear FA registration in the STZ group and the linear CCFAy registration in the CTL group. Nevertheless, it remained unclear whether any of the procedures did improve the spatial normalization of the structure, since there was no consistency across methods. The fornix might not have been affected by partial volume effect, but only challenging to register because of its small size and low signal. Incoherent changes in the fornix shown by the preliminary results supported the decision to continue using conventional anatomical registration to obtain this ROI's label.

The corpus callosum was highly affected by the hypersized ventricles, since the STZ group always had a lower ratio than the CTL group across the methods. The CCFAy was the map with higher R, which was partially expected, since this ROI links the two hemispheres and therefore it mainly diffuses in the x- and y-directions. Accordingly, CCFAy and CCFAx had a ratio difference in module of only 1.7% in the STZ group. Considering that CCFAy was the only method better than the anatomical registration with a ratio difference of 1.2%, it was the method chosen for this ROI to undergo non-linear registration.

Lastly, as expected, the fimbria was clearly the most affected ROI by ventricle enlargement, with the largest ratio difference between groups of 21.8% in the anatomical registration. This means that in the STZ group, an average of 82 in 186 voxels was being dramatically left out of the analysis because of misalignment issues. Strong improvements were shown by CCFAz in the STZ group and CCFAx in the CTL group. In this case, it was noteworthy that even the CTL group underwent partial volume effect without having enlarged ventricles, because of the simple fact that the fimbria is closer to the ventricles

than any other ROI considered in this study. The ratio difference in the STZ group between CCFAz and CCFAx was 1.8%, whereas in the CTL group was 1.6%. After taking a close inspection to the overlaid labels in diffusion data, the CCFAz was the method selected to undergo non-linear transformation.

Hence, the corpus callosum and the fimbria were the most affected ROIs by misalignment caused by enlarged ventricles. Non-linear registration was performed with the respective affine matrix as a starting estimate for CCFAy and CCFAz data, respectively. The comparison between linear and non-linear registration in each ROI is shown in the *Table 4.2* for CTL and STZ groups and in the *Figure 4.7*. The cingulum and the fornix were not further considered in the analysis.

R			Anatomical Registration	Registration	
				Linear	Non-linear
CCFAy	CC	STZ	0.9537	0.9662	0.9843
		CTL	0.9743	0.9830	0.9847
CCFAz	Fimbria	STZ	0.6650	0.7683	0.8199
		CTL	0.8834	0.9167	0.8524

Table 4.2: Average R calculated after linear and non-linear registration of the method selected for the corpus callosum (CC) and the fimbria in each study group.

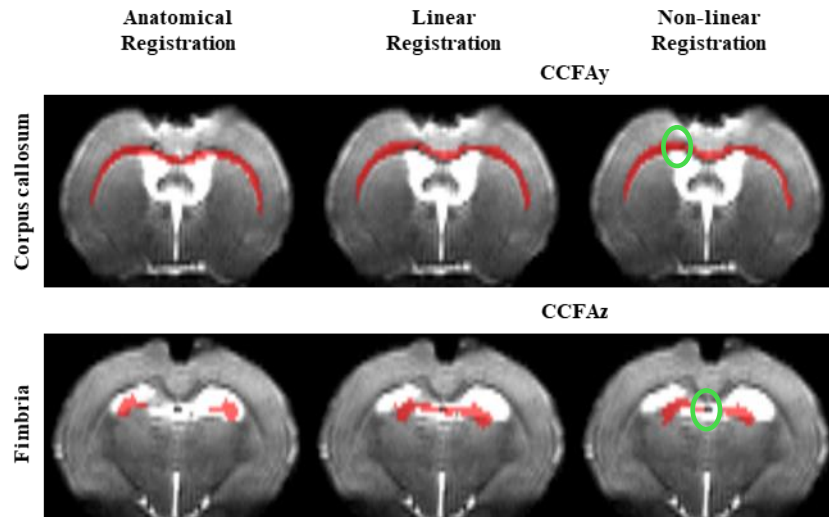


Figure 4.7: Comparison between the ROIs (rows) extracted from atlases resulting from linear and non-linear registration (columns) of the method selected in the first stage in a STZ dataset.

Except for the CTL group in the fimbria, all non-linear methods overpassed linear registration. In the STZ group, the fimbria had a ratio difference between linear and non-linear registration of 5.2% and the corpus callosum of 1.8%. Visual inspection confirmed a preference for the non-linear procedure in both ROIs, as seen in the green circles.

Since non-linear CCFAy and CCFAz registration showed improved ratios in the corpus callosum and the fimbria, respectively, statistical tests were performed to have a quantification of such improvements. From the preliminary results, t -tests showed more significant differences and therefore only these were computed herein. The comparison between differences in metrics obtained in labels from anatomical registration and from the potential improved registration procedure is presented in the *Table 4.3* for the corpus callosum and in the *Table 4.4* for the fimbria. In these tables, p -values are representative of the differences between groups at each time point.

<i>p</i> -values <i>t</i> -test			Anatomical Registration	Non-linear CCFAy Registration
CC	D_a	2 weeks	0.0048	0.0181
	$D_{e,\parallel}$	6 weeks	0.0460	>0.05
	FA	13 weeks	>0.05	0.0002
	AD	13 weeks	0.0237	0.0035
	MK	13 weeks	0.0395	0.0006
	AK	13 weeks	0.0352	0.0013
	RK	13 weeks	>0.05	0.0034
	f	13 weeks	>0.05	0.0429

Table 4.3: Comparison between *t*-tests computed in the preliminary results and with CCFAx in the corpus callosum (CC). *p*-values quantify differences between groups at each time point in diffusion metrics.

<i>p</i> -values <i>t</i> -test			Anatomical Registration	Non-linear CCFAz Registration
Fimbria	MD	2 weeks	0.0322	0.0081
	RD	2 weeks	0.0061	0.0008
	D_a	2 weeks	0.0146	0.0172
	FA	13 weeks	0.0040	0.0057
	MD	13 weeks	>0.05	0.0154
	RD	13 weeks	0.0124	0.0022
	MK	13 weeks	0.0033	0.0096
	RK	13 weeks	0.0072	0.0234
	f	13 weeks	0.0237	0.0379

Table 4.4: Comparison between *t*-tests computed in the preliminary results and with CCFAz in the fimbria. *p*-values quantify differences between groups at each time point in diffusion metrics.

p-values with lower orders of magnitude are highlighted in green in these tables and with higher orders of magnitude in red. In all cases, there are new differences in metrics that were not significant in the preliminary results. In the corpus callosum, there was one difference in a metric that lost power with non-linear registration. However, not only most significant changes were improved by one or two orders of magnitude, but new significant changes were evident as well. Overall, it seemed that the alignment of the corpus callosum was optimized with non-linear CCFAy registration, leading to increased statistical power in the results. The results in the fimbria were equally great, with one difference in a metric that lost power after non-linear CCFAz registration, but with several metrics differences being improved. In the most dramatic case of partial volume effect, the ratio of voxel kept in analysis increased from 66.5% to 82.0%. Therefore, CCFAy and CCFAz template atlases were added to the registration pipeline, where optimization was guaranteed.

4.1.5. Evaluation of the initial values in the WMTI-Watson model

Several initial values were set in the estimation of the WMTI-Watson model. Each combination of initial parameters corresponded to a different iteration that provided a single vector of parameter values for the “fitting” and “unfitting” voxels. The parameter values obtained are shown in the histograms in the Figure 4.8 for a total of 3750 iterations. The first row is the distribution of parameters in the “fitting” voxels while the second row is the distribution in the “unfitting” voxel.

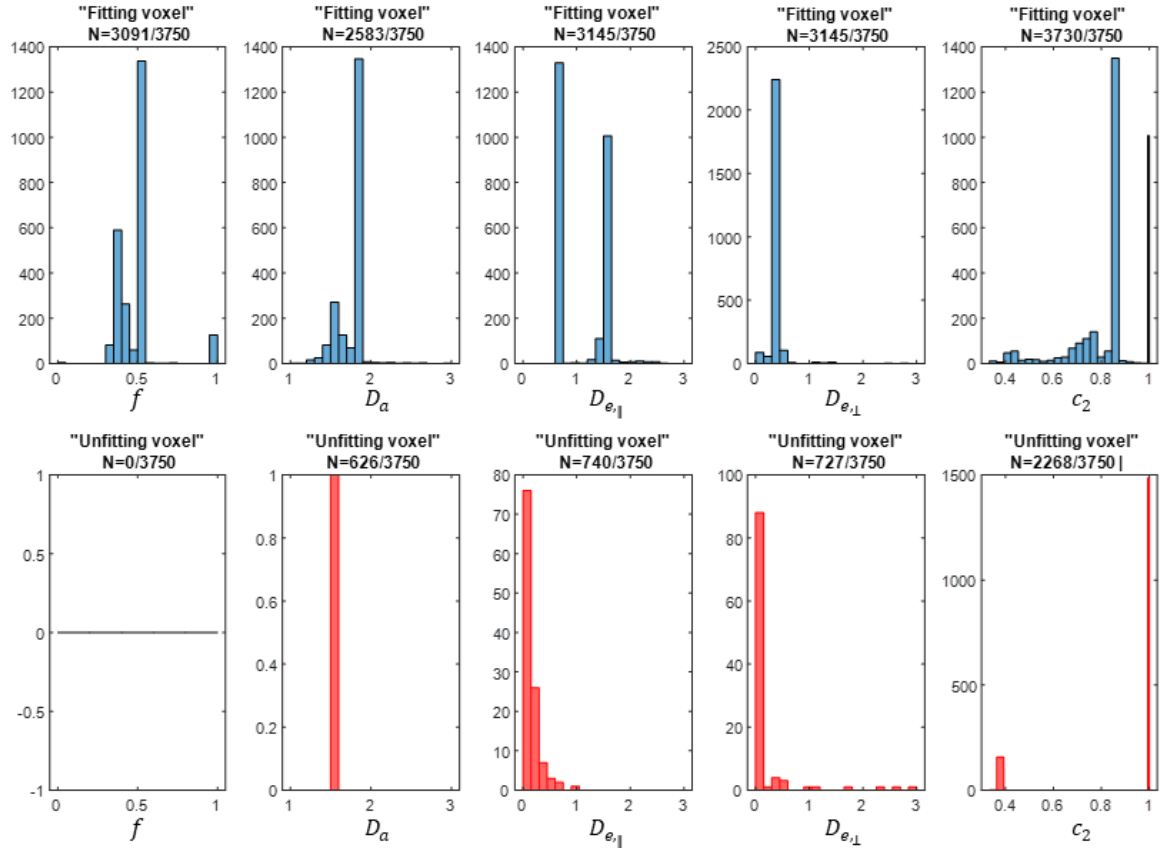


Figure 4.8: Histograms of each WMTI-Watson model parameter (columns) in two different voxels (rows) with 3750 combinations of initial values. The window of each parameter comprises parameter values considered to be biophysically reasonable.

In the “fitting” voxel, most iterations, i.e. most combinations of initial parameters, led to the same range of solutions. These were, as expected, within the acceptable range of biophysical values that pass the criteria for the model to work. However, way less combinations led to that range of solutions in the “unfitting” voxel. The iterations that actually worked in this voxel, i.e. where parameters were within the biophysically acceptable values, led to a distribution different from the one in the “fitting” voxel. This means that the parameters cannot be represented as a function of the initial guesses because no combination of values improves the estimation and therefore the problem must lie within the data.

When an optimization solver completes its task, it sets an *exitflag*, whose integer value encodes the reason the solver has stopped. While successful outcomes set a positive *exitflag*, unsuccessful outcomes set a negative. When this value is equal to zero, it means that the fitting has reached its computational limit. Accordingly, the *exitflags* of each iteration for each voxel are shown in the Table 4.5. It is noteworthy that there were no successful iterations within the “unfitting” voxel.

Exitflags		-2	0	1
“Fitting” voxel	Number of iterations	1294	879	1577
“Unfitting” voxel		1803	1947	0

Table 4.5: Number of iterations with each *exitflag* value for each voxel

Despite having several diffusion encoding directions that allow for the overestimation of the model, there might be an additional bias in data provided that different b-values were used in acquisition with different sampling directions each. Whereas a 14 T magnetic field might improve the signal amplitude, it also increases vibration in turn. The fast EPI acquisition contributes to a high image distortion as well and in general, rat data quality is not as accurate as desired.

Moreover, the FOV was narrow because of the rat head size, which decreased the SNR. For instance, SNR in the “fitting” voxel is roughly 16 whereas in the “unfitting” voxel is 9. This might explain the reason that more than half of the voxels of the ROIs are not accounted for in the analysis. Since changing the initial values was shown to have little impact in the parameters’ values in the “unfitting” voxel, nothing can be done within this project regarding the high exclusion of values in model estimation unless different image resolution is pursued. Thus, any strategy was applied to the existing pipeline and this issue can only be addressed by changing data acquisition parameters.

4.2. Statistical analysis of diffusion metrics using the optimized pipeline

Herein, the results of the statistical tests described in the Section 3.5 are shown. The tests were computed on diffusion metrics extracted after implementing the proposed optimization methodologies defined in the Section 3.4 and tested in the Section 4.1. The strategies confirmed to show satisfactory results in terms of efficiency of computation, data quality and reliability of metrics were included.

4.2.1. Tensor-derived metrics results

The most relevant significant differences in the mean values of the metrics derived from the DTI and DKI tensors are shown in the *Figure 4.9*. Other differences were significant, but the metrics represented in these boxplots were considered to capture the fundamental significant differences in these metrics. All the metrics boxplots and significant p -values are shown in the Appendix A.

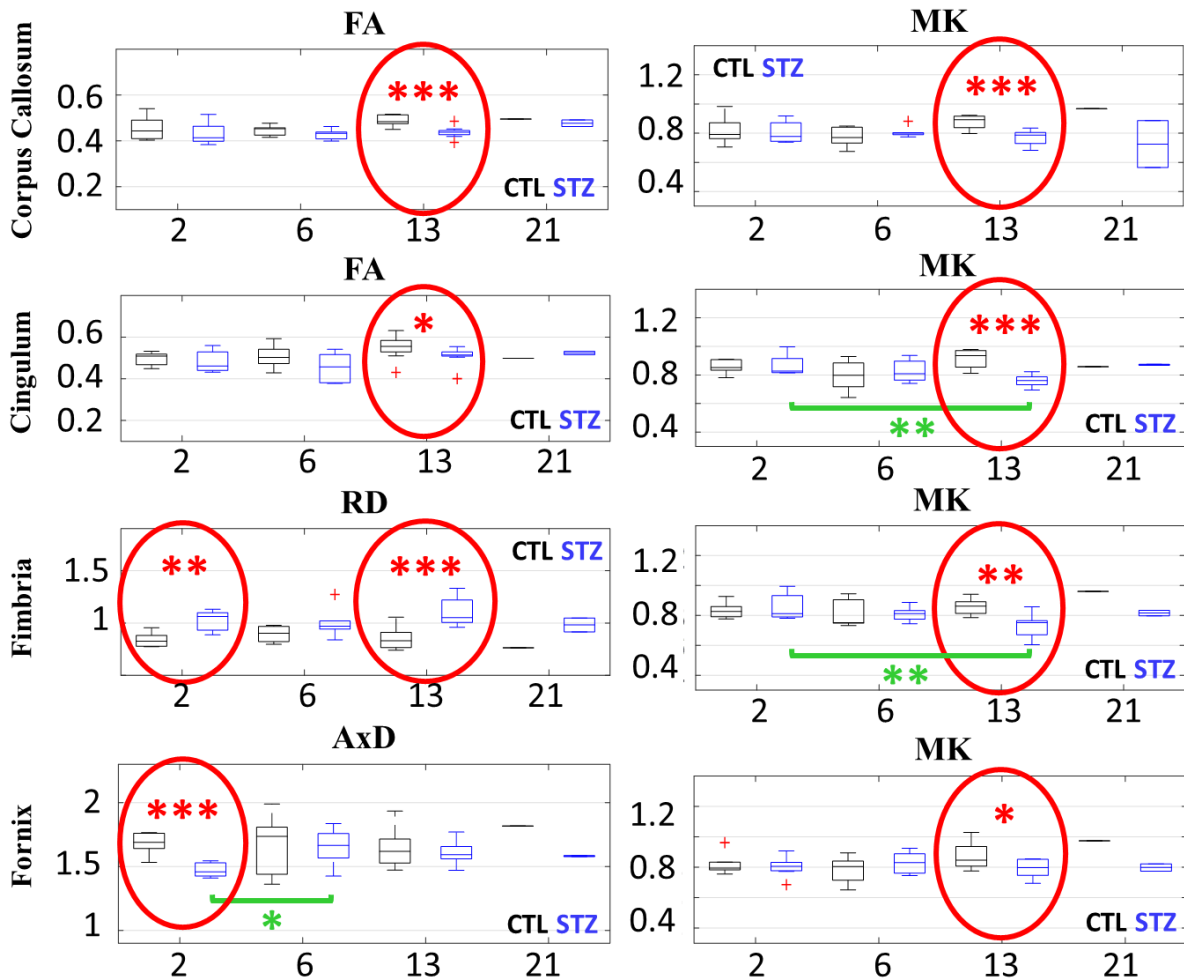


Figure 4.9: Boxplots of DTI and DKI derived metrics. Significant differences between study groups at each time point are shown in red and within groups over time in green. *: $p < 0.05$, **: $p < 0.01$ and ***: $p < 0.001$.

It is noticeable that there were more significant differences between groups at each time point than over time. Nevertheless, while at 2 weeks and 13 weeks after injection, there were differences between groups, at 6 weeks there were no differences between groups at all.

The differences between groups at 2 weeks after injection were only showed in the fimbria and fornix. Interestingly, there were only significant differences in the fimbria at 2 weeks in the radial direction, whereas in the fornix significant differences were found in the axial direction. In the fimbria, the STZ group had higher RD at 2 and 13 weeks than the CTL group, and in the fornix the STZ group had lower AD at 2 weeks than the CTL group. At 13 weeks after injection, in addition to the fimbria and the fornix, the corpus callosum and the cingulum showed significant differences as well. In the STZ group, FA was significantly lower in these ROIs than in the CTL group. Across the whole brain, there were significant differences between groups in the MK at 13 weeks. STZ rats showed a significantly lower MK than the CTL rats. Moreover, MK metrics were significantly lower over time in the STZ group between 2 weeks and 13 weeks after injection in the cingulum and the fimbria.

4.2.2. WMTI-Watson model metrics results

The most significant differences in the mean values of the metrics derived from the estimation of the WMTI-Watson biophysical model are shown in the *Figure 4.10* and *Figure 4.11*. Other differences were significant, but the metrics shown in these boxplots were considered to capture the fundamental differences in these metrics. All the metrics boxplots and significant p -values are shown in the Appendix A.

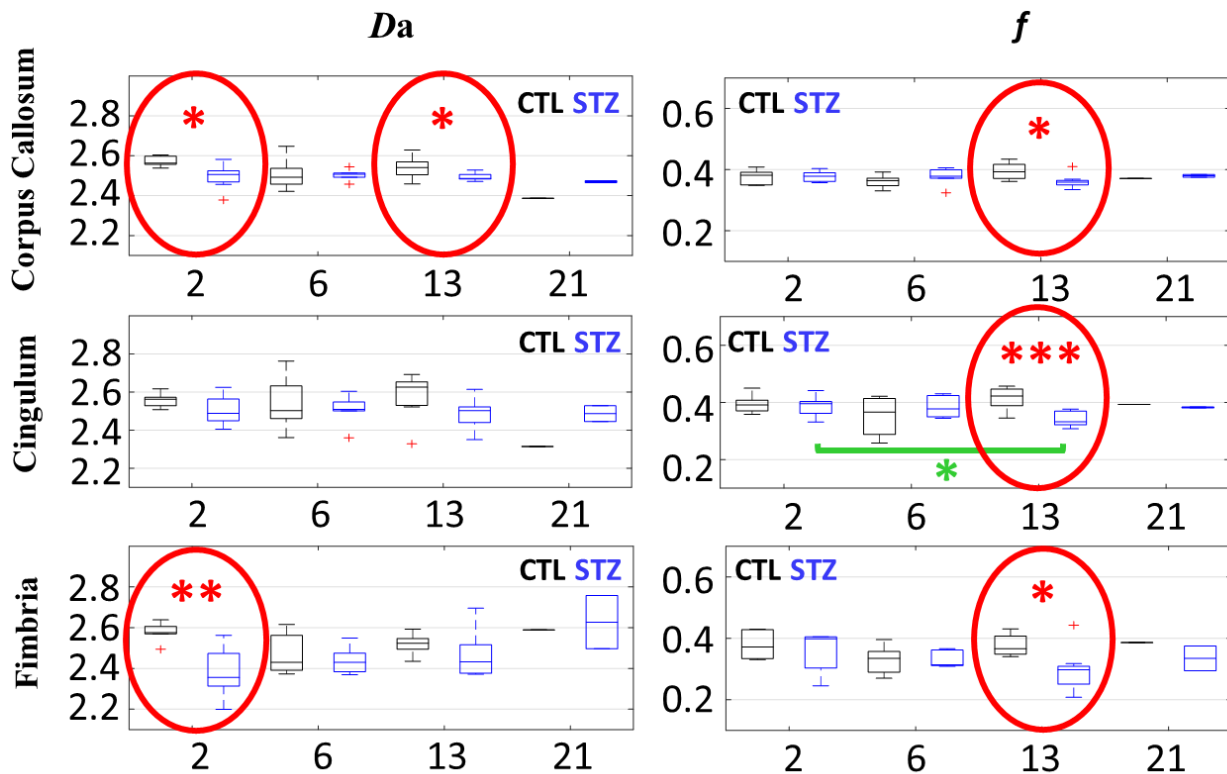


Figure 4.10: Boxplots of WMTI-Watson model parameters. Significant differences between study groups at each time point are shown in red and within groups over time in green. *: $p < 0.05$, **: $p < 0.01$ and ***: $p < 0.001$.

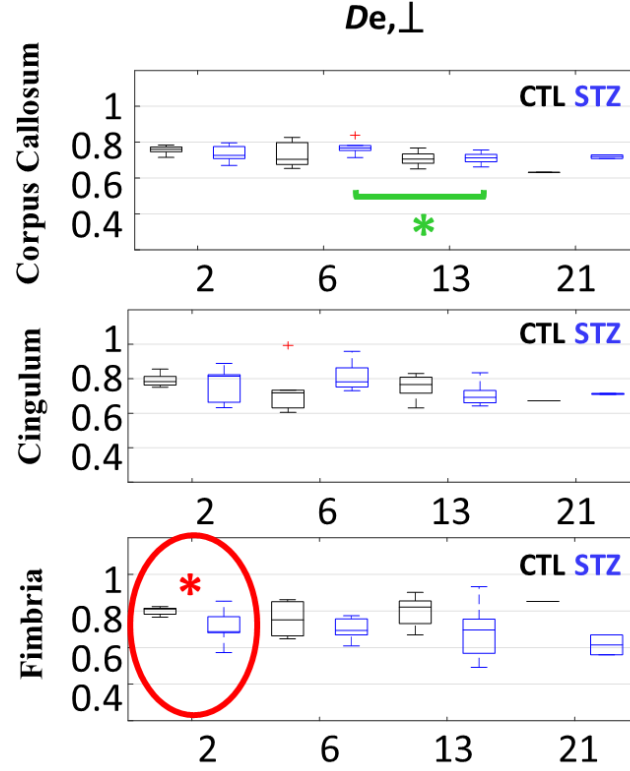


Figure 4.11: Boxplots of WMTI-Watson model parameters. Significant differences between study groups at each time point are shown in red and within groups over time in green. *: $p < 0.05$.

There were less significant differences in the model derived parameters, which might be due to the high amount of voxels being excluded from analysis by the filter in the Equation 5.2. as assessed in the Section 4.1.5. As in the previous metrics, there were more significant differences between groups than over time and no significant differences in metrics were reported at 6 weeks. At 2 weeks, the STZ group had lower D_a than the CTL group in the corpus callosum and in the fimbria.

At 13 weeks, D_a in the STZ group was also lower than the CTL group in the corpus callosum, but not at 6 weeks after injection. In contrast, there were only changes in f at 13 weeks across all the ROIs except for the fornix. f was lower in the STZ group than in the CTL group. In addition, between 2 weeks and 13 weeks there was a significant decrease in f in the STZ group. Finally, $D_{e,\parallel}$ was significantly lower in the STZ group than in the CTL group in the fimbria at 2 weeks after injection, and between 6 weeks and 13 weeks it decreased significantly in the corpus callosum.

4.3. Additional diffusion analysis strategies

Herein are shown the results from the new approaches to analyse diffusion data presented in the Section 3.6. These were complementary strategies to the information obtained in the previous section and were not subjected to the conventional statistical analysis. Rather than improving the processing pipeline, it provides the study with additional information about the microstructure that is expected to complement the spatio-temporal pattern found in the white matter diffusion metrics. In case these results supported the analysis, these methodologies could be improved in the domain of new projects.

4.3.1. Gray matter analysis for correlation with white matter metrics

According to the preliminary results, MK decreases significantly over time in the STZ group and it is often significantly higher in the CTL group than in the STZ group. This was an expected tendency because MK quantifies the complexity of the structure, i.e. a higher MK corresponds to a more developed tract microstructure. This in turn corresponds to a lower MD. As to evaluate how gray and white matter are spatially and temporally affected in terms of microstructure, scatter plots of the MK in the white matter vs MD in the gray matter were computed and they are shown in the *Figure 4.12*. Only three of the six relations were found to be relevant.

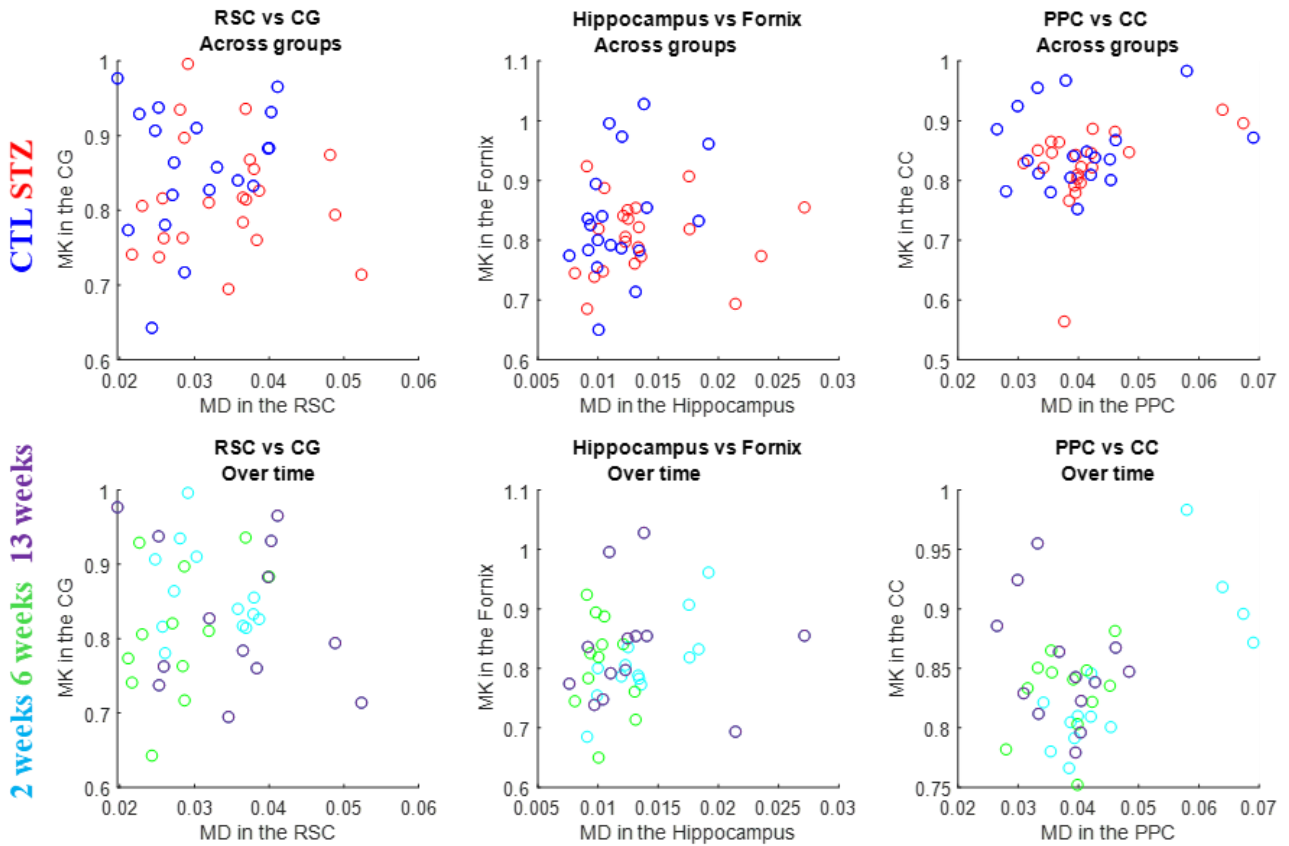


Figure 4.12: Scatter plots of the relationship between degeneration in the white matter and gray matter. This analysis was carried out across groups (upper row) and over time (lower row) between regions known to be relevant to AD and anatomically connected. CG: cingulum, CC: corpus callosum.

Regarding results across groups, it is noticed that higher MK in the white matter corresponds to lower MD in the gray matter in the CTL group in the first two relationships. Generally, the CTL group has a higher MK and therefore a lower MD, while the STZ group has a lower MK and a higher MD. However, a few datasets do not follow this tendency as they belong to different time points after injection. At 2 weeks, toxicity has not immediately affected all rats and at 6 weeks, there is recovery in STZ rats which might explain why some of the datasets have such a high MK or such a low MD. In addition, a higher MK can also represent inflammation as was reported in the treated group in previous studies.

Over time, the relationship between the cingulum and the RSC is representative of the expected results. At 2 weeks after injection, the cingulum shows a high MK and RSC a low MD, while at 6 weeks the cingulum shows a high MK and RSC shows an even lower MD. This refers to the potential recover period reported in the literature. At 13 weeks after injection, lower MK of the cingulum corresponds to higher MD of the RSC, which represent STZ datasets. Interestingly, the dataset with lower MD is a CTL rat at 13 weeks, meaning a situation of full development.

In the fornix vs hippocampus, the relationship is not as clear at 13 weeks, but in general results are similar and consistent with the results shown in previous sections and with the view that the hippocampus is one of the firstly affected regions in AD. In the corpus callosum versus PPC, at 2 weeks the relationship is nothing as expected, with CTL and STZ rats having high MK and high MD. This might be meaningful regarding the time and speed at which each tract is affected. In fact, the corpus callosum only showed differences in DTI and DKI metrics later in the timeline.

The spatial pattern of these results is consistent with the interpretation of the preliminary results of diffusion metrics. With such a huge amount of data available, the information about the gray matter is highly promising. Statistical tests could be computed to reach correlations between regions in space and time, providing a new understanding of the progression of AD-like features in the icv-STZ model. A model of the microstructure that could extend to the gray matter would be useful in the interpretation of changes that were here shown to be a two-edged knife.

4.3.2. Tractography for quality assessment of metrics

In this context, tractography was performed in order to isolate the 3D tracts of interest and analyse the spatio-temporal pattern of AFD in each tract. After computing FODs and performing FOD registration to the created template, tracks were generated and edited. The automatic generation of tracts was complemented with manual editing and the resultant tracts of interest are shown in the *Figure 4.13*.

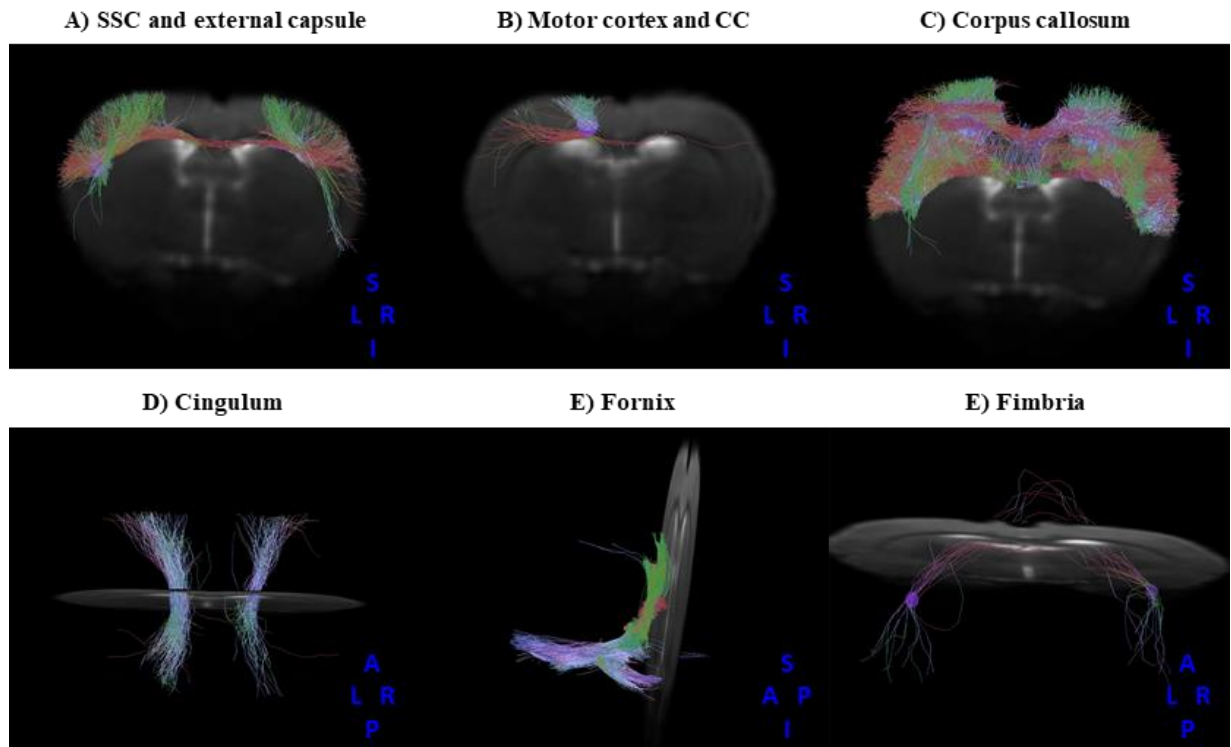


Figure 4.13: Isolation of tracks of interest after track generation using ROI-editing techniques and manual correction. SSC: somatosensory cortex, CC: corpus callosum.

Because of the wide structure of the corpus callosum, three different views were shown to facilitate its interpretation. In A), there are seeds in the corpus callosum and external capsule, which is an extension of this white matter tract, at both hemispheres. Here, it is clear the connection between the basal ganglia and the somatosensorial cortex through the corpus callosum and the external capsule. In B) is shown another known connection between the motor cortex and the corpus callosum, more posterior than A). C) is the complete corpus callosum tract used for metrics estimation. It connects both sides of

the brain with multiple ramifications into the cortex. D), E) and F) are the other tracts of interest used in the analysis. The cingulum in D) viewed from top consists in two bundles of fibers that traverse the brain from front to back, right above the corpus callosum. E) is the fornix from a lateral perspective, which forms a C-shaped structure and is connected to the fimbria in F) in the midline of the brain. SSC: Somatosensory cortex.

AFD was estimated in the tracks of interest and averaged for each dataset. Plots of the averaged AFD normalized by the average streamlines' length are shown in the *Figure 4.14*.

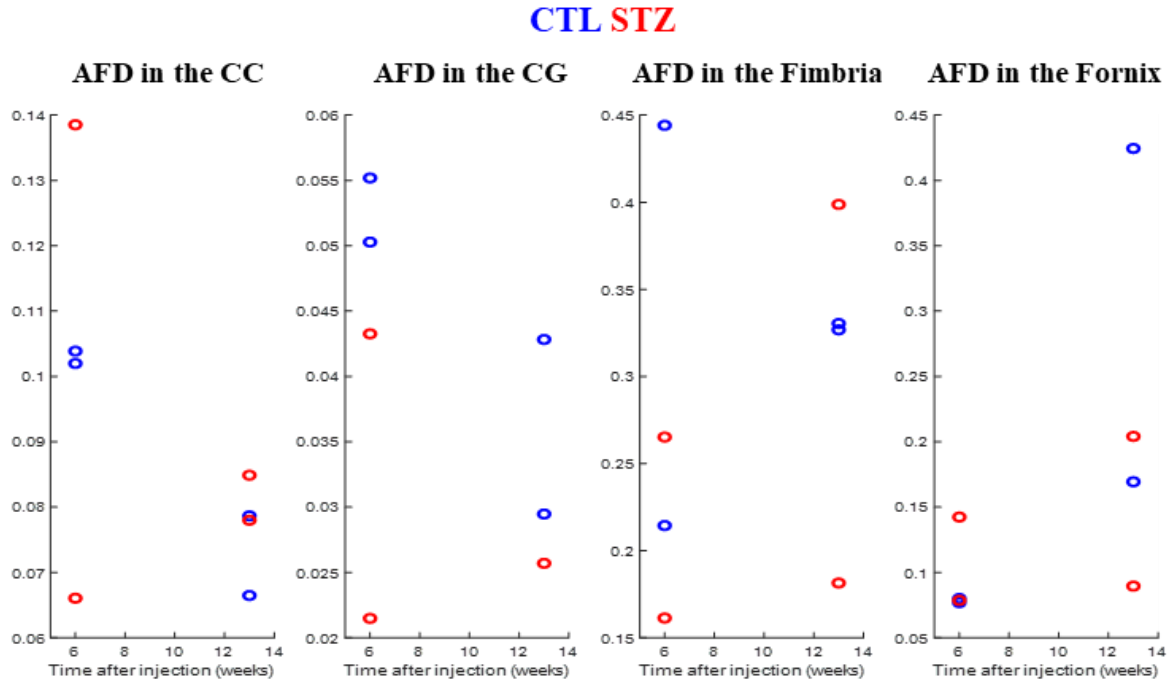


Figure 4.14: Plots of the normalized AFD in each tract of interest at each time point. CC: corpus callosum, CG: cingulum.

The cingulum is the track with AFD closer to expected because the AFD in the STZ group is lower than in the CTL group at all time points. However, the AFD in the CTL group is decreasing with time. The fornix might also be representative because the AFD in the CTL group increases abruptly, but the corpus callosum and the fimbria show random tendencies. AFD datasets were clearly not consistent with each other nor with the diffusion metrics. This may be due to problems with the processing while creating the FOD template or during registration of FOD datasets. It was extremely hard to have an automatic procedure to isolate tracts and, in some cases, manual editing was necessary. Especially because of partial volume effect, the corpus callosum and the fimbria were very different from one dataset to another, as mirrored in the AFD plots.

Even though none of these metrics were conclusive and track editing has been time-consuming, the isolation of tracks was successful considering that this project started with no previous knowledge and a completely new processing pipeline had to be learnt. In the future, tracks should be obtained exclusively manually. The metrics extracted from them will clarify whether the processing methodology is being correctly followed or if adjustments to the FOD estimation or track generation should be considered. Naturally, a larger sample is required to provide statistical validation, however this is counterproductive since a larger sample asks for a more automatized procedure. A lot of work needs to be done in this regard and, even though the results of the pipeline were not quite as planned, this assessment can be helpful to further develop the methodology. Tractography would be an excellent tool to avoid partial volume effect in the estimation of tensors and model metrics if instead of using labels extracted from atlases, tracks were used as 3D binary masks.

5. Discussion

5.1. White matter microstructural patterns

In this project, white matter microstructure was assessed longitudinally in icv-STZ rats. Voxel-based analysis was computed by calculating DTI and DKI tensors whose extracted metrics are sensitive to the underlying changes of the tracts of interest. In addition, parameters were derived from the WMTI-Watson biophysical model of diffusion. The spatio-temporal pattern of these metrics in each ROI was compared between STZ and CTL groups by statistical analysis, where most of the significant differences were found between groups at given time points, rather than over time. Regardless, it was possible to infer how degeneration of white matter might be evolving after icv-STZ injection and the results were consistent with previous studies of this animal model.

Tensors metrics showed significant differences between groups in the fimbria and fornix as early as 2 weeks after injection. Whereas differences in the radial direction suggest inflammation or demyelination in the fimbria, changes in the axial direction suggest intra-axonal injury of the fornix. From the model, STZ rats showed lower intra-axonal diffusivity at 2 weeks in the fimbria and corpus callosum, which is indicative of axonal damage. In addition, lower perpendicular extra-axonal diffusivity in the STZ group at 2 weeks suggests lower extra-cellular crowding in the fimbria. This result was counter-intuitive because of the potential inflammation of this tract suggested by tensor metrics.

At 6 weeks, there were no reports of group differences in any of the metrics, which corresponds to a well-established trend in the icv-STZ model. The presence of a recover period normally follows early acute damage and precedes definite chronic axonal loss. Accordingly, at 13 weeks tensors metrics showed intense significant differences in all ROIs, mainly manifested by lower anisotropy and complexity in STZ rats. This suggests fiber dispersion and degeneration, respectively, in all tracts after the recover period. Importantly, the STZ group showed lower complexity over time in all ROIs between 2 weeks after injection and 13 weeks. Model parameters confirmed axonal loss with lower water volume fraction at 13 weeks. Thus, the corpus callosum and the cingulum have shown to be affected later in the disease, while the fimbria and fornix were primarily affected, as reported in other studies [8], [9].

This project confirms that while axonal injury was reported by DTI and DKI sensitive measures, the modelling of white matter provided specificity to the underlying changes, allowing for more precise interpretations of changes within the icv-STZ brain microstructure. Axonal injury was specifically translated into intra-axonal damage at 2 weeks after injection and into axonal loss at 13 weeks after injection, which is consistent with the non-monotonic changes reported in the icv-STZ model [10]. The *Figure 5.1* shows the final timeline of the patterns found.

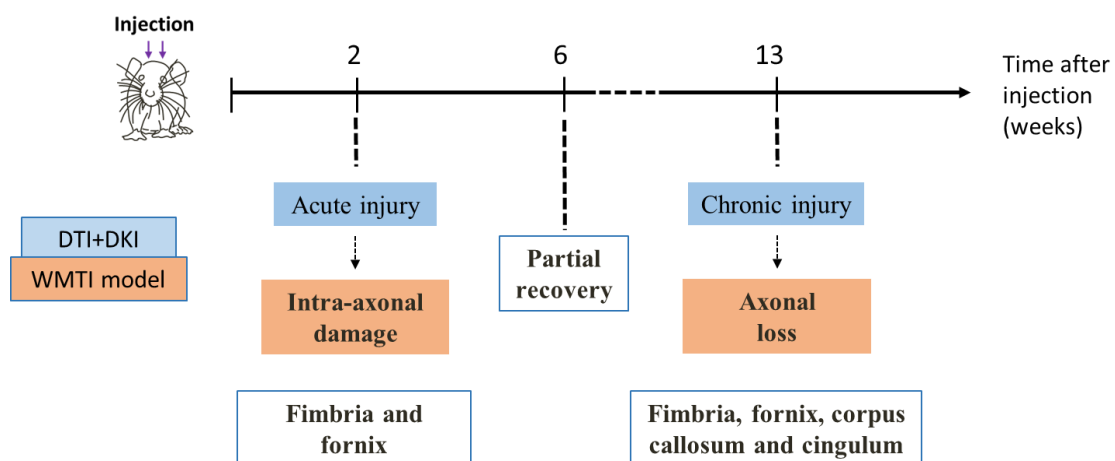


Figure 5.1: Interpretation of spatio-temporal pattern of diffusion metrics obtained by DTI, DKI and the biophysical model.

Unfortunately, the “21 weeks” time point was not statistically powerful by the time of analysis and a tendency of future results was not clear. New datasets have been acquired and will undergo image processing and analysis soon. Diffusion metrics between groups are expected to be highly different at this time point as degeneration has been confirmed at 13 weeks after injection. However, longitudinal changes may not arise because both groups start being affected by ageing which might confound microstructural metrics.

5.2. Consistency with previous studies

In parallel with this project, analysis of functional connectivity of the rat brain was computed as well. At 2 weeks after injection, significantly lower brain connectivity in the STZ group was found between the hippocampus and the ACC [125]. It is noteworthy that the fimbria and fornix are connected to the hippocampus and also showed differences at this time point in the microstructural assessment. In addition, gray matter analysis showed degeneration of the hippocampus early in the disease. Accordingly, a previous study has reported neuronal loss at the septum at 4 weeks, which has cholinergic projections to the hippocampus [8]. NFT changes were found in the hippocampal area at 12 weeks, followed by the presence of diffuse A β plaques at 24 weeks in a recent study [9].

Regarding the potential recovery at 6 weeks, a study of the cognitive performance of the icv-STZ model has shown early sudden deficits at 4 weeks after injection, followed by a compensatory process up to 12 weeks and a slow progressive chronic decline from 12 weeks on. In the functional connectivity analysis, there was also no group differences affecting the default mode network at this time point [125]. This was considered a critical point in which pathological processes could not be compensated any longer [9] and was confirmed by this study of the white matter microstructure.

Effectively, at 13 weeks after injection, the PPC showed lower connectivity with the visual cortex in the STZ rats than CTL rats [125]. PPC is anatomically connected to the corpus callosum which showed lower diffusivity at this time point as well. Moreover, the functional connectivity between the ACC and the RSC, regions linked to the cingulum, showed to vary differently over time. STZ rats showed decreased ACC-RSC connectivity between 2 and 13 weeks after injection, while this connectivity increased in CTL rats. Furthermore, other studies have reported thinning of the corpus callosum and cingulum in later time points [8], [9]. Gray matter analysis did not reveal a relationship between degeneration of the corpus callosum and atrophy of the PPC at any of the time points. Nevertheless, STZ and CTL groups showed different patterns in this relationship which might indicate that the PPC was atrophied before the corpus callosum was degenerated at 13 weeks. Contrarily, a relationship between cingulum degeneration and RSC atrophy was pronounced, even though the STZ rats have not shown significant microstructural differences in the cingulum at 2 weeks.

There are several relations between the project here reported and other studies that refer to different biomarkers. Not only this fact supports the credibility of this experimental animal model, but it also marks the importance of studying the individual impact of each hallmark on the progression of neurodegeneration.

5.3. Optimization strategies

Despite being useful in the interpretation of microstructural changes, as aforementioned, the WMTI-Watson model might not have reached its full potential because of insufficient data quality. Estimation performance might have been compromised by the presence of imaging artefacts incapable of being removed by the processing pipeline. These artefacts affected the fitting of the model's equations in such a way that nearly 60% of the white matter voxels had unphysical values and were excluded from statistical analysis to avoid influencing the results. This means that there might be other significant differences within model parameters or the existing differences might be even more powerful.

Along with the WMTI-Watson model unfitting, statistical results were partially affected by ventricle enlargement, typical of neurodegenerative diseases, which was one of the principal issues within the processing pipeline. Simultaneously, the strategy proposed for overcoming the spatial misalignment caused by the oversized ventricles was the most successful of the pipeline alterations. The fimbria was dramatically affected by partial volume effect with CSF, with 33% of the fimbria label voxels being removed from diffusion metrics analysis because they did not pass the white matter filter imposed by diffusion metrics intervals. A different registration approach effectively reduced this value to 18% in the STZ group. The corpus callosum benefited as well from this methodology, as the white matter filter reduced the voxels removed from 5% to 2% in the STZ group. Non-linear transformation of CCFA data had a direct impact in the statistical power of longitudinal changes between and within groups by providing lower p -values by at least one order of magnitude in most of existing differences in metrics. Thus, the improvements in the misalignment issues allowed for more reliable metrics.

Another technique that might be able to minimize partial volume effect is tractography. Within this project there was not enough time to use the reconstructed tracts to recalculate diffusion metrics and compare with the ROI-based analysis. Nevertheless, the tracts representing the ROIs of this study were semi-automatically isolated and validated by the anatomical connections encountered. Even though AFD measures were not consistent with the main results, the pipeline needs further development and a larger sample is required. Once the pipeline is approved, tractography might bring along new opportunities for analysis of the microstructure and connectivity.

Apart from the exploratory analysis of the model that did not allow for its estimation optimization, all other strategies proposed were successful and therefore implemented in the pipeline to obtain the final results. Namely, correspondence between atlas labels and the underlying structure was improved, time-consuming steps of the pipeline were semi-automated ensuring the same performance as manual processing and noise induced by MRI inhomogeneities was reduced.

6. Conclusion

The icv-STZ model was once again validated with the use of MRI derived biomarkers as it has shown brain alterations consistent with the ones previously reported. It constitutes an excellent model of sporadic AD because it reflects alterations commonly found in the human brain. The time and speed at which tracts are affected was different and at later time points more tracts were affected. While rats have rarely been assessed with DWI because of the lower image resolution and presence of noisy artefacts, this pipeline was able to extract measures longitudinally and spatially distributed as predicted. The model parameters combined with tensors metrics offer a unique set of tools for a fairly specific interpretation of changes in diffusion data.

With a relatively large sample, this project takes part in a soon-to-be interdisciplinary study of the rat brain that will allow to establish the pattern of white matter degeneration, reduced functional connectivity, amyloid deposition, brain atrophy and cognitive impairment in function of time after injection and brain location. Apart from DWI assessment, rs-fMRI data have been acquired and processed as aforementioned, FDG-PET data have already been acquired and histological staining are currently being processed. Cognitive performance assessment will be done as well to correlate all the information about any type of alterations occurring in rat brain. This will hopefully lead to significant progress in the understanding of the very first pathological changes within the brain and their propagation over time until clinical evidence arises, in rats developing AD-like features after brain glucose metabolism disruption. Once the early mechanisms are well characterized and investigations clarify the primary cause of the cascade, detection will be possible before symptoms are evident, opening a window for early treatment and AD incidence reduction.

Overall, the engineering approach was considered helpful for this study as most of pipeline strategies adjustments were valuable for estimating more reliable diffusion metrics. Two projects here initiated might also be further developed for correlation with all data in current acquisition and/or processing within the study. It is recommended to update the processing pipeline occasionally with the most state-of-art techniques to keep up with other studies and provide trustworthy information for the knowledge of AD and neurodegenerative diseases.

This traineeship met the requirements for the project here presented, as the main task of obtaining the longitudinal pattern of white matter microstructure in the icv-STZ rat was completed. Further advances to the processing pipeline were accomplished and the project outcomes were presented to the public at several occasions, as shown in the Appendix B in the Section 8.2.

7. References

- [1] R. A. Sperling *et al.*, “Toward defining the preclinical stages of Alzheimer’s disease: Recommendations from the National Institute on Aging-Alzheimer’s Association workgroups on diagnostic guidelines for Alzheimer’s disease,” *Alzheimer’s Dement.*, vol. 7, no. 3, pp. 280–292, 2011.
- [2] “Alzheimer’s Association Report: Alzheimer’s disease facts and figures,” Elsevier Inc., 2017.
- [3] S. Julia, Z. Arvanitakis, W. Bang, and D. A. Bennett, “Mixed brain pathologies account for most dementia cases in community-dwelling older persons,” *Neurology*, vol. 69, no. 24, 2007.
- [4] S. Festing and R. Wilkinson, “The ethics of animal research,” *EMBO Rep.*, vol. 8, no. 6, pp. 519–520, 2007.
- [5] S. Hoyer, “Glucose metabolism and insulin receptor signal transduction in Alzheimer disease,” *Eur. J. Pharmacol.*, vol. 490, no. 1–3, pp. 115–125, 2004.
- [6] R. Nitsch and S. Hoyer, “Local action of the diabetogenic drug, streptozotocin, on glucose and energy metabolism in rat brain cortex,” *Neurosci. Lett.*, vol. 128, pp. 199–202, 1991.
- [7] K. Plaschke *et al.*, “Insulin-Resistant Brain State after Intracerebroventricular Streptozotocin Injection Exacerbates Alzheimer-like Changes in Tg2576 A β PP-Overexpressing Mice,” *J. Alzheimer’s Dis.*, vol. 19, pp. 691–704, 2010.
- [8] A. Kraska *et al.*, “In Vivo Cross-sectional Characterization of Cerebral Alterations Induced by Intracerebroventricular Administration of Streptozotocin,” *PLoS One*, vol. 7, no. 9, pp. 1–9, 2012.
- [9] A. Knezovic *et al.*, “Staging of cognitive deficits and neuropathological and ultrastructural changes in streptozotocin-induced rat model of Alzheimer’s disease,” *J. Neural Transm.*, vol. 122, no. 4, pp. 577–592, 2015.
- [10] S. Shoham, C. Bejar, E. Kovalev, and M. Weinstock, “Intracerebroventricular injection of streptozotocin causes neurotoxicity to myelin that contributes to spatial memory deficits in rats,” *Exp. Neurol.*, vol. 184, no. 2, pp. 1043–1052, 2003.
- [11] N. Lester-coll, E. J. Rivera, S. J. Soscia, K. Doiron, J. R. Wands, and S. M. De Monte, “Intracerebral streptozotocin model of type 3 diabetes: Relevance to sporadic Alzheimer’s disease,” *J. Alzheimer’s Dis.*, vol. 9, pp. 13–33, 2006.
- [12] J. H. Heo, S. R. Lee, and S. T. et al Lee, “spatial distribution of glucose hypometabolism induced by intracerebroventricular streptozotocin in monkeys,” *J. Alzheimer’s Dis.*, 2011.
- [13] D. Le Bihan, “Molecular diffusion nuclear magnetic resonance imaging,” *Magn. Reson. Q.*, vol. 7, no. 1, pp. 1–30, 1991.
- [14] J. H. Jensen, J. A. Helpert, A. Ramani, H. Lu, and K. Kaczynski, “Diffusional Kurtosis Imaging : The Quantification of Non- Gaussian Water Diffusion by Means of Magnetic Resonance Imaging,” *Magn. Reson. Med.*, vol. 1440, pp. 1432–1440, 2005.
- [15] D. Le Bihan, C. Poupon, C. A. Clark, S. Pappata, N. Molko, and H. Chabriet, “Diffusion Tensor Imaging: Concepts and Applications,” *Magn. Reson. Imaging*, vol. 13, pp. 534–546, 2001.
- [16] E. Fieremans, J. H. Jensen, and J. A. Helpert, “White matter characterization with diffusional kurtosis imaging,” *Neuroimage*, vol. 58, no. 1, pp. 177–188, 2011.
- [17] I. O. Jelescu and M. D. Budde, “Design and Validation of Diffusion MRI Models of White Matter,” *Front. Phys.*, vol. 5, 2017.
- [18] J. Duda, P. J. Basser, C. Pierpaoli, A. Aldroubi, and S. Pajevic, “In vivo fiber tractography using DT-MRI data,” *Magn. Reson. Med.*, vol. 44, no. 4, pp. 625–632, 2002.
- [19] Y. L. Chang, T. F. Chen, Y. C. Shih, M. J. Chiu, S. H. Yan, and W. Y. I. Tseng, “Regional cingulum disruption, not gray matter atrophy, detects cognitive changes in amnesic mild cognitive impairment subtypes,” *J. Alzheimer’s Dis.*, vol. 44, no. 1, pp. 125–138, 2015.
- [20] I. O. Jelescu, T. M. Shepherd, and D. S. et al Novikov, “White matter tract integrity, amyloid burden and structural atrophy in normal aging and mild cognitive impairment: a PET-MRI study,” *ISMRM 23rd Annu. Meet. Exhib. Toronto, Canada*, vol. 509, 2015.
- [21] M. A. A. Binnewijzend *et al.*, “Resting-state fMRI changes in Alzheimer’s disease and mild

- cognitive impairment,” *Neurobiol. Aging*, vol. 33, no. 9, pp. 2018–2028, 2012.
- [22] P. J. Basser, J. Mattiello, and D. LeBihan, “Estimation of the effective self-diffusion tensor from the NMR s,” *J. Magn. Reson.*, vol. 103, pp. 247–254, 1994.
 - [23] P. J. Basser, J. Mattiello, and D. LeBihan, “MR Diffusion Tensor Spectroscopy Imaging,” *Biophys. J.*, vol. 66, pp. 259–267, 1994.
 - [24] C. R. Jack, D. S. Knopman, W. J. Jagust, and R. C. et al Petersen, “Update on hypothetical model of Alzheimer’s disease biomarkers,” *Lancet Neurol*, vol. 12, no. 2, pp. 207–216, 2013.
 - [25] C. R. Jack, D. S. Knopman, W. J. Jagust, and L. M. et al Shaw, “Hypothetical model of dynamic biomarkers of the Alzheimer’s pathological cascade,” *Lancet Neurol*, vol. 9, no. 119, p. 60, 2010.
 - [26] P. Edison *et al.*, “Amyloid, hypometabolism, and cognition in Alzheimer’s disease. And [11C]PIB and [18F]FDG PET study,” *Neurology*, vol. 68, no. 7, 2007.
 - [27] G. W. Small, L. M. Ercoli, and D. S. Silverman et al, “Cerebral metabolic and cognitive decline in persons at genetic risk for Alzheimer’s disease,” *Proc. Natl. Acad. Sci. USA*, vol. 97, no. 11, pp. 6037–6042, 2000.
 - [28] M. Bobinski *et al.*, “The histological validation of post mortem magnetic resonance imaging determined hippocampal volume in alzheimer’s disease,” *Neuroscience*, vol. 95, no. 3, pp. 721–725, 2000.
 - [29] G. M. Shankar and D. M. Walsh, “Alzheimer’s disease: Synaptic dysfunction and A β ,” *Mol. Neurodegener.*, vol. 4, no. 1, pp. 1–13, 2009.
 - [30] D. J. Selkoe, “Alzheimer’s disease results from the cerebral accumulation and cytotoxicity of amyloid beta-protein,” *J. Alzheimer’s Dis.*, vol. 3, no. 1, pp. 75–80, 2001.
 - [31] P. I. Moreira, A. I. Duarte, M. S. Santos, A. C. Rego, and C. R. Oliveira, “An integrative view of the role of oxidative stress, mitochondria and insulin in Alzheimer’s disease,” *J. Alzheimer’s Dis.*, vol. 16, no. 4, pp. 741–761, 2009.
 - [32] D. Attwell and S. B. Laughlin, “An energy budget for signalling in the grey matter of the brain,” *J. Cereb. Blood Flow Metab.*, vol. 21, pp. 1133–1145, 2001.
 - [33] W. W. Seeley, R. K. Crawford, J. Zhou, B. L. Miller, and M. D. Greicius, “Neurodegenerative Diseases Target Large-Scale Human Brain Networks,” *Neuron*, vol. 62, no. 1, pp. 42–52, 2009.
 - [34] I. L. Choo *et al.*, “Posterior cingulate cortex atrophy and regional cingulum disruption in mild cognitive impairment and Alzheimer ’ s disease,” *Neurobiol. Aging*, vol. 31, no. 5, pp. 772–779, 2010.
 - [35] E. Fieremans, A. Benitez, J. H. Jensen, M. F. Falangola, A. Tabesh, and R. L. et al Deardorff, “Novel White Matter Tract Integrity Metrics Sensitive to Alzheimer Disease Progression,” *J. Neuroradiol*, vol. 34, no. 11, pp. 2105–2112, 2013.
 - [36] J. Hardy, “The amyloid hypothesis for Alzheimer’s disease: A critical reappraisal,” *J. Neurochem.*, vol. 110, no. 4, pp. 1129–1134, 2009.
 - [37] S. Hoyer, “Causes and consequences of disturbances of cerebral glucose metabolism in sporadic Alzheimer’s disease: therapeutic implications,” *Front. Clin. Neurosci.*, pp. 135–152, 2004.
 - [38] K. Ono, “Alzheimer’s disease as oligomeropathy,” *Neurochem. Int.*, vol. 119, pp. 57–70, 2018.
 - [39] D. Hardy, J; Selkoe, “The amyloid hypothesis of Alzheimer’s Disease: progress and problems on the road of therapeutics,” *Science (80-.)*, vol. 297, pp. 353–357, 2002.
 - [40] S. J. C. Lee, E. Nam, H. J. Lee, M. G. Savellieff, and M. H. Lim, “Towards an understanding of amyloid- β oligomers: Characterization, toxicity mechanisms, and inhibitors,” *Chem. Soc. Rev.*, vol. 46, no. 2, pp. 310–323, 2017.
 - [41] M. H. Hinrichs, A. Jalal, B. Brenner, E. Mandelkow, S. Kumar, and T. Scholz, “Tau protein diffuses along the microtubule lattice,” *J. Biol. Chem.*, vol. 287, no. 46, pp. 38559–38568, 2012.
 - [42] S. Oddo *et al.*, “Temporal profile of amyloid- β (A β) oligomerization in an in vivo model of Alzheimer disease: A link between A β and tau pathology,” *J. Biol. Chem.*, vol. 281, no. 3, pp. 1599–1604, 2006.
 - [43] S. R.G., A. T., P. P.R., B. G.J., and Y. X.-X., “Is brain amyloid production a cause or a result of dementia of the Alzheimer’s type?,” *J. Alzheimer’s Dis.*, vol. 22, no. 2, pp. 393–399, 2010.

- [44] Z. Van Helmond, J. S. Miners, P. G. Kehoe, and S. Love, "Higher soluble amyloid β concentration in frontal cortex of young adults than in normal elderly or Alzheimer's disease," *Brain Pathol.*, vol. 20, no. 4, pp. 787–793, 2010.
- [45] T. D. Bird, "Genetic aspects of Alzheimer disease," *Genet. Med.*, vol. 10, no. 4, pp. 231–239, 2008.
- [46] H. J. Aizenstein *et al.*, "Frequent Amyloid Deposition Without Significant Cognitive Impairment Among the Elderly," *Arch. Neurol.*, vol. 65, no. 11, pp. 1509–1517, 2008.
- [47] S. S. *et al.*, "A phase 2 multiple ascending dose trial of bapineuzumab in mild to moderate Alzheimer disease," *Neurology*, vol. 73, no. 24, pp. 2061–2070, 2009.
- [48] L. Mosconi *et al.*, "Declining brain glucose metabolism in normal individuals with a maternal history of Alzheimer disease," *Neurology*, vol. 72, no. 6, pp. 513–520, 2009.
- [49] J. P. Blass, G. E. Gibson, and S. Hoyer, "The role of the metabolic lesion in Alzheimer's disease," *J. Alzheimer's Dis.*, vol. 4, no. 3, pp. 225–232, 2002.
- [50] S. C. Correia, R. X. Santos, G. Perry, X. Zhu, P. I. Moreira, and M. A. Smith, "Insulin-resistant brain state : The culprit in sporadic Alzheimer ' s disease ?," *Ageing Res. Rev.*, vol. 10, pp. 264–273, 2011.
- [51] S. Cardoso *et al.*, "Insulin is a two-edged knife on the brain," *J. Alzheimer's Dis.*, vol. 18, pp. 483–507, 2009.
- [52] D. C. Solano, M. Sironi, C. Bonfini, and S. B. Solerte, "Insulin regulates soluble amyloid precursor protein release via phosphatidyl inositol 3 kinase-dependent," *FASEB J.*, vol. 14, no. May, pp. 1015–1022, 2000.
- [53] C. M. Cheng, V. Tseng, J. Wang, D. Wang, L. Matyakhina, and C. A. Bondy, "Tau is hyperphosphorylated in the insulin-like growth factor-I null brain," *Endocrinology*, vol. 146, no. 12, pp. 5086–5091, 2005.
- [54] W. Q. Zhao, H. Chen, M. J. Quon, and D. L. Alkon, "Insulin and the insulin receptor in experimental models of learning and memory," *Eur. J. Pharmacol.*, vol. 490, no. 1–3, pp. 71–81, 2004.
- [55] L. Frölich, D. Blum-Degen, P. Riederer, and S. Hoyer, "A disturbance in the neuronal insulin receptor signal transduction in sporadic Alzheimer's disease," *Ann. N. Y. Acad. Sci.*, vol. 893, pp. 290–293, 1999.
- [56] G. S. Watson and S. Craft, "Modulation of memory by insulin and glucose: Neuropsychological observations in Alzheimer's disease," *Eur. J. Pharmacol.*, vol. 490, no. 1–3, pp. 97–113, 2004.
- [57] S. Hoyer, R. Nitsch, and K. Oesterreich, "Predominant abnormality in cerebral glucose utilization in late-onset dementia of the Alzheimer type: a cross sectional comparison against advanced late-onset and incipient early-onset cases," *J Neural Transm.*, vol. 3, pp. 1–14, 1991.
- [58] C. Balducci and G. Forloni, "Novel targets in Alzheimer's disease: A special focus on microglia," *Pharmacol. Res.*, vol. 130, pp. 402–413, 2018.
- [59] G. Mayer, R. Nitsch, and S. Hoyer, "Effects of changes in peripheral and cerebral glucose metabolism on locomotor activity, learning and memory in adult male rats," *Brain Res.*, vol. 532, no. 1–2, pp. 95–100, 1990.
- [60] A. Nazem, R. Sankowski, M. Bacher, and Y. Al-Abed, "Rodent models of neuroinflammation for Alzheimer's disease," *J. Neuroinflammation*, vol. 12, no. 1, pp. 1–15, 2015.
- [61] C. Westbrook, C. K. Roth, and J. Talbot, *MRI in Practice*, 4th ed. 1993.
- [62] R. B. Lufkin, *The MRI manual*, 2nd ed. 1997.
- [63] R. W. Brown, Y. C. N. Cheng, E. M. Haacke, M. R. Thompson, and R. Venkatesan, *Magnetic Resonance Imaging: Physical Principles and Sequence Design*, 2nd ed. 2014.
- [64] L. R. Delapaz, "Echo-planar Imaging," *RadioGraphics*, pp. 1045–1058, 1994.
- [65] A. L. Alexander, K. M. Hasan, M. Lazar, J. S. Tsuruda, and D. L. Parker, "Analysis of Partial Volume Effects in Diffusion-Tensor MRI," *IEEE Trans. Med. Imaging*, vol. 45, no. 1, pp. 770–780, 2001.
- [66] A. Einstein, "Investigations on the theory of the Brownian movement," *Dover Publ. Inc.*, 1956.

- [67] A. L. Alexander, J. E. Lee, M. Lazar, and A. S. Field, "Diffusion Tensor Imaging of the Brain," *Neurotherapeutics*, vol. 4, pp. 316–329, 2007.
- [68] A. Paydar *et al.*, "Diffusional Kurtosis Imaging of the Developing Brain," *Pediatrics*, pp. 808–814, 2014.
- [69] P. Z. Sun, Y. Wang, E. Mandeville, S. T. Chan, E. H. Lo, and X. Ji, "Validation of fast diffusion kurtosis MRI for imaging acute ischemia in a rodent model of stroke," *NMR Biomed.*, vol. 27, no. 11, pp. 1413–1418, 2014.
- [70] D. K. Jones, M. A. Horsfield, and A. Simmons, "Optimal Strategies for Measuring Diffusion in Anisotropic Systems by Magnetic Resonance Imaging," *Magn. Reson. Med.*, vol. 42, pp. 515–525, 1999.
- [71] N. G. Papadakis, L. D. Hall, and T. A. Carpenter, "A Comparative Study of Acquisition Schemes for Diffusion Tensor Imaging Using MRI," *J. Magn. Reson.*, vol. 137, pp. 67–82, 1999.
- [72] C. G. Koay, L. C. Chang, J. D. Carew, C. Pierpaoli, and P. J. Basser, "A unifying theoretical and algorithmic framework for least squares methods of estimation in diffusion tensor imaging," *J. Magn. Reson.*, vol. 182, no. 1, pp. 115–125, 2006.
- [73] A. L. Alexander, K. Hasan, G. Kindlmann, D. L. Parker, and J. S. Tsuruda, "A Geometric Analysis of Diffusion Tensor Measurements of the Human Brain," *Magn. Reson. Med.*, vol. 44, pp. 283–291, 2000.
- [74] S. Pajevic and C. Pierpaoli, "Color Schemes to Represent the Orientation of Anisotropic Tissues From Diffusion Tensor Data : Application to White Matter Fiber Tract Mapping in the Human Brain," *Magn. Reson. Med.*, vol. 42, pp. 526–540, 1999.
- [75] P. J. Basser, S. Pajevic, C. Pierpaoli, J. Duda, and A. Aldroubi, "In Vivo Fiber Tractography Using DT-MRI Data," *Magn. Reson. Med.*, vol. 44, pp. 625–632, 2000.
- [76] B. Hansen, N. Shemesh, and S. Nørhøj, "NeuroImage Fast imaging of mean , axial and radial diffusion kurtosis," *Neuroimage*, vol. 142, pp. 381–393, 2016.
- [77] S. N. Jespersen, J. L. Olesen, B. Hansen, and N. Shemesh, "Diffusion time dependence of microstructural parameters in fixed spinal cord," *Neuroimage*, vol. 182, pp. 329–342, 2018.
- [78] H. Zhang, T. Schneider, C. A. Wheeler-Kingshott, and D. C. Alexander, "NODDI: Practical in vivo neurite orientation dispersion and density imaging of the human brain," *Neuroimage*, vol. 61, no. 4, pp. 1000–1016, 2012.
- [79] I. O. Jelescu, J. Veraart, V. Adisetiyo, S. S. Milla, D. S. Novikov, and E. Fieremans, "One diffusion acquisition and different white matter models: How does microstructure change in human early development based on WMTI and NODDI?," *Neuroimage*, vol. 107, pp. 242–256, 2015.
- [80] D. S. Novikov, J. Veraart, I. O. Jelescu, and E. Fieremans, "Rotationally-invariant mapping of scalar and orientational metrics of neuronal microstructure with in vivo diffusion MRI," *Neuroimage*, 2016.
- [81] S. N. Jespersen, L. A. Leigland, A. Cornea, and C. D. Kroenke, "Determination of Axonal and Dendritic Orientation Distributions Within the Developing Cerebral Cortex by Diffusion Tensor Imaging," *IEEE Trans. Med. Imaging*, vol. 31, no. 1, pp. 16–32, 2012.
- [82] I. O. Jelescu, J. Veraart, E. Fieremans, and D. S. Novikov, "Degeneracy in model parameter estimation for multi-compartmental diffusion in neuronal tissue," *NMR Biomed.*, vol. 29, no. 1, pp. 33–47, 2016.
- [83] S. Mori and P. C. M. Van Zijl, "Fiber tracking: Principles and strategies - A technical review," *NMR Biomed.*, vol. 15, no. 7–8, pp. 468–480, 2002.
- [84] T. E. Conturo *et al.*, "Tracking neuronal fiber pathways in the living human brain," *Proc. Natl. Acad. Sci.*, vol. 96, pp. 10422–10427, 1999.
- [85] S. Mori, B. Crain, V. P. Chacko, and P. C. M. Van Zijl, "Three-dimensional tracking of axonal projections in the brain by magnetic resonance imaging," *Ann. Neurol.*, vol. 45, no. 2, pp. 265–269, 1999.
- [86] T. E. J. Behrens *et al.*, "Characterization and Propagation of Uncertainty in Diffusion-Weighted MR Imaging," *Magn. Reson. Med.*, vol. 50, no. 5, pp. 1077–1088, 2003.

- [87] T. E. J. Behrens, H. J. Berg, S. Jbabdi, M. F. S. Rushworth, and M. W. Woolrich, "Probabilistic diffusion tractography with multiple fibre orientations: What can we gain?," *Neuroimage*, vol. 34, no. 1, pp. 144–155, 2007.
- [88] J. D. Tournier, F. Calamante, D. G. Gadian, and A. Connelly, "Direct estimation of the fiber orientation density function from diffusion-weighted MRI data using spherical deconvolution," *Neuroimage*, vol. 23, no. 3, pp. 1176–1185, 2004.
- [89] D. Raffelt, J. D. Tournier, S. Crozier, A. Connelly, and O. Salvado, "Reorientation of fiber orientation distributions using apodized point spread functions," *Magn. Reson. Med.*, vol. 67, no. 3, pp. 844–855, 2012.
- [90] D. M. Healy, H. Hendriks, and P. T. Kim, "Spherical Deconvolution," *J. Multivar. Anal.*, vol. 67, pp. 1–22, 1998.
- [91] D. Raffelt, S. Crozier, and A. Connelly, "Apparent Fibre Density: a new measure for high angular resolution diffusion-weighted image analysis," *Proc. Intl. Soc. Magn. Res. Med.*, vol. 20, no. 11, p. 2010, 2010.
- [92] D. K. Jones, "The Effect of Gradient Sampling Schemes on Measures Derived From Diffusion Tensor MRI: A Monte Carlo Study," *Magn. Reson. Med.*, vol. 51, pp. 807–815, 2004.
- [93] J. Veraart, E. Fieremans, and D. S. Novikov, "Diffusion MRI noise mapping using random matrix theory," *Magn Reson Med*, vol. 76, no. 5, pp. 1582–1593, 2017.
- [94] L. C. Chang, D. K. Jones, and C. Pierpaoli, "RESTORE: Robust estimation of tensors by outlier rejection," *Magn. Reson. Med.*, vol. 53, no. 5, pp. 1088–1095, 2005.
- [95] R. Turner, D. Le Bihan, J. Maier, R. Vavrek, L. K. Hedges, and J. Pekar, "Echo-planar imaging of intravoxel incoherent motion," *Radiology*, vol. 177, no. 2, 1990.
- [96] J. C. Haselgrove and J. R. Moore, "Correction for distortion of echo-planar images used to calculate the apparent diffusion coefficient," *Magn. Reson. Med.*, vol. 36, no. 6, pp. 960–964, 1996.
- [97] P. Jezzard, A. S. Barnett, and C. Pierpaoli, "Characterization of and correction for eddy current artifacts in echo planar diffusion imaging," *Magn. Reson. Med.*, vol. 39, no. 5, pp. 801–812, 1998.
- [98] A. L. Alexander, J. S. Tsuruda, and D. L. Parker, "Elimination of eddy current artifacts in diffusion-weighted echo-planar images: The use of bipolar gradients," *Magn. Reson. Med.*, vol. 38, no. 6, pp. 1016–1021, 1997.
- [99] J. L. R. Andersson, S. Skare, and J. Ashburner, "How to correct susceptibility distortions in spin-echo echo-planar images: Application to diffusion tensor imaging," *Neuroimage*, vol. 20, no. 2, pp. 870–888, 2003.
- [100] L. Ibanez, L. Ng, J. C. Gee, and S. Aylward, "Registration patterns: The generic framework for image registration of the Insight Toolkit," *IEEE Int. Symp. Biomed. Imaging*, pp. 345–348, 2002.
- [101] J. Ashburner and K. Friston, "Multimodal Image Coregistration and Partitioning - a Unified Framework," *Neuroimage*, vol. 6, no. 3, pp. 209–217, 1997.
- [102] J. Ashburner and K. J. Friston, "Nonlinear Spatial Normalization using Basic Functions," *Hum. Brain Mapp.*, vol. 7, pp. 254–266, 1999.
- [103] C. Rorden and M. Brett, "Stereotaxic display of brain lesions," *Behav. Neurol.*, vol. 12, pp. 191–200, 2000.
- [104] S. M. Smith *et al.*, "Advances in functional and structural MR image analysis and implementation as FSL," *Neuroimage*, vol. 23, no. SUPPL. 1, pp. 208–219, 2004.
- [105] J. L. R. Andersson and S. N. Sotiropoulos, "An integrated approach to correction for off-resonance effects and subject movement in diffusion MR imaging," *Neuroimage*, vol. 125, pp. 1063–1078, 2016.
- [106] L. J. Kjonigsen, S. Lillehaug, J. G. Bjaalie, M. P. Witter, and T. B. Leergaard, "Waxholm Space atlas of the rat brain hippocampal region: Three-dimensional delineations based on magnetic resonance and diffusion tensor imaging," *Neuroimage*, vol. 108, pp. 441–449, 2015.
- [107] P. A. Valdés-hernández *et al.*, "An in vivo MRI template set for morphometry, tissue segmentation, and fMRI localization in rats," *Front. Neuroinform.*, vol. 5, pp. 1–19, 2011.
- [108] M. Jenkinson and S. Smith, "Global optimisation for robust affine registration of brain images,"

- Med. Image Anal.*, vol. 5, pp. 143–156, 2001.
- [109] M. Jenkinson, P. Bannister, M. Brady, and S. Smith, “Improved optimization for the robust and accurate linear registration and motion correction of brain images,” *Neuroimage*, vol. 17, no. 2, pp. 825–841, 2002.
 - [110] J. Andersson, M. Jenkinson, and S. Smith, “Non-linear registration aka Spatial normalisation FMRIB Technial Report TR07JA2,” 2010.
 - [111] J. Veraart, J. Sijbers, S. Sunaert, A. Leemans, and B. Jeurissen, “Weighted linear least squares estimation of diffusion MRI parameters : Strengths, limitations, and pitfalls,” *Neuroimage*, vol. 81, pp. 335–346, 2013.
 - [112] P. A. Yushkevich *et al.*, “User-guided 3D active contour segmentation of anatomical structures: Significantly improved efficiency and reliability,” *Neuroimage*, 2006.
 - [113] S. M. Smith, “Fast robust automated brain extraction.,” *Hum. Brain Mapp.*, vol. 17, no. 3, pp. 143–55, 2002.
 - [114] J. S. Cox and R. W. Hyde, “AFNI: Software for analysis and visualization of functional magnetic resonance neuroimages.,” *Comput. Biomed. Res.*, vol. 29, pp. 162–173, 1996.
 - [115] C. B. Do and S. Batzoglou, “What is the expectation maximization algorithm?,” *Nat. Biotechnol.*, vol. 26, no. 8, pp. 897–899, 2008.
 - [116] T. Simon, L. Ding, J. Bish, E. McDonald-McGinn, D., Zackai, and J. Gee, “Volumetric, connective, and morphologic changes in the brains of children with chromosome 22q11.2 deletion syndrome: an integrative study,” *Neuroimage*, vol. 25, pp. 169– 180, 2005.
 - [117] H. J. Park *et al.*, “Spatial normalization of diffusion tensor MRI using multiple channels,” *Neuroimage*, vol. 20, no. 4, pp. 1995–2009, 2003.
 - [118] D. K. Jones *et al.*, “Spatial normalization and averaging of diffusion tensor MRI data sets.,” *Neuroimage*, vol. 17, no. 2, pp. 592–617, 2002.
 - [119] D. K. Jones *et al.*, “Age effects on diffusion tensor magnetic resonance imaging tractography measures of frontal cortex connections in schizophrenia,” *Hum. Brain Mapp.*, vol. 27, no. 3, pp. 230–238, 2006.
 - [120] S. M. Smith *et al.*, “Tract-based spatial statistics: voxelwise analysis of multi-subject diffusion data.,” *Neuroimage*, vol. 31, no. 4, pp. 1487–505, 2006.
 - [121] J. Dong, I. O. Jelescu, B. Ades-aron, and D. S. et al Novikov, “diffusion kurtosis and derived white matter tract integrity metrics in the fornix differ in beta-amyloid positive versus negative groups,” *Am. J. Neuroradiol.*, 2016.
 - [122] J. D. Tournier, F. Calamante, and A. Connelly, “Determination of the appropriate b value and number of gradient directions for high-angular-resolution diffusion-weighted imaging,” *NMR Biomed.*, vol. 26, no. 12, pp. 1775–1786, 2013.
 - [123] J. D. Tournier, F. Calamante, and A. Connelly, “Robust determination of the fibre orientation distribution in diffusion MRI: Non-negativity constrained super-resolved spherical deconvolution,” *Neuroimage*, vol. 35, no. 4, pp. 1459–1472, 2007.
 - [124] J. D. Tournier, C. F., and A. Connelly, “Improved probabilistic streamlines tractography by 2,” *Proc. Intl. Soc. Magn. Res. Med.*, vol. 18, 2010.
 - [125] Y. Diao, C. T. Pereira, T. Yin, A. R. da Silva, R. Gruetter, and I. O. Jelescu, “Spatio-temporal alterations in functional connectivity in a rat model of brain glucose metabolism disruption and sporadic Alzheimer’s disease,” in *Proceedings of the Intl. Soc. Magn. Res. in Medicine*, 2019.

8. Appendices

8.1. Appendix A

After processing all data using the optimized pipeline, metrics were averaged over ROIs and displayed in boxplots over time and divided into study groups (blue: STZ, black: CTL). The patterns of the metrics were assessed by two statistical tests that compared means between study groups at each time point and over time within each study group. p -values resultant from these statistical tests were used to quantify the significance of differences in metrics. In the Section 4.2 the boxplots with the fundamental differences were presented in the *Figure 4.9*, *Figure 4.10* and *Figure 4.11*. Here, all boxplots of DTI (*Figure 8.1*), DKI (*Figure 8.2*) and model derived metrics (*Figure 8.3* and *Figure 8.4*) are shown, as well as the p -values from the t -tests (*Table 8.1*) and ANOVAs (*Table 8.2*).

For instance, the first row of the *Table 8.1* means that at 2 weeks after injection there is a very significant difference in the mean FA in the fimbria between the STZ and the CTL groups ($p < 0.01$). In the respective boxplot in the *Figure 8.1*, the mean FA in the STZ group is considerably lower than in the CTL group. In the *Table 8.2* the first row of the table means that within the STZ group, the mean MD in the cingulum is significantly different between the “2 weeks” and the “13 weeks” time points ($p < 0.05$). In the respective boxplot in the *Figure 8.1*, the mean MD in the STZ group is considerably lower over time. The same is inferred to other significant differences.

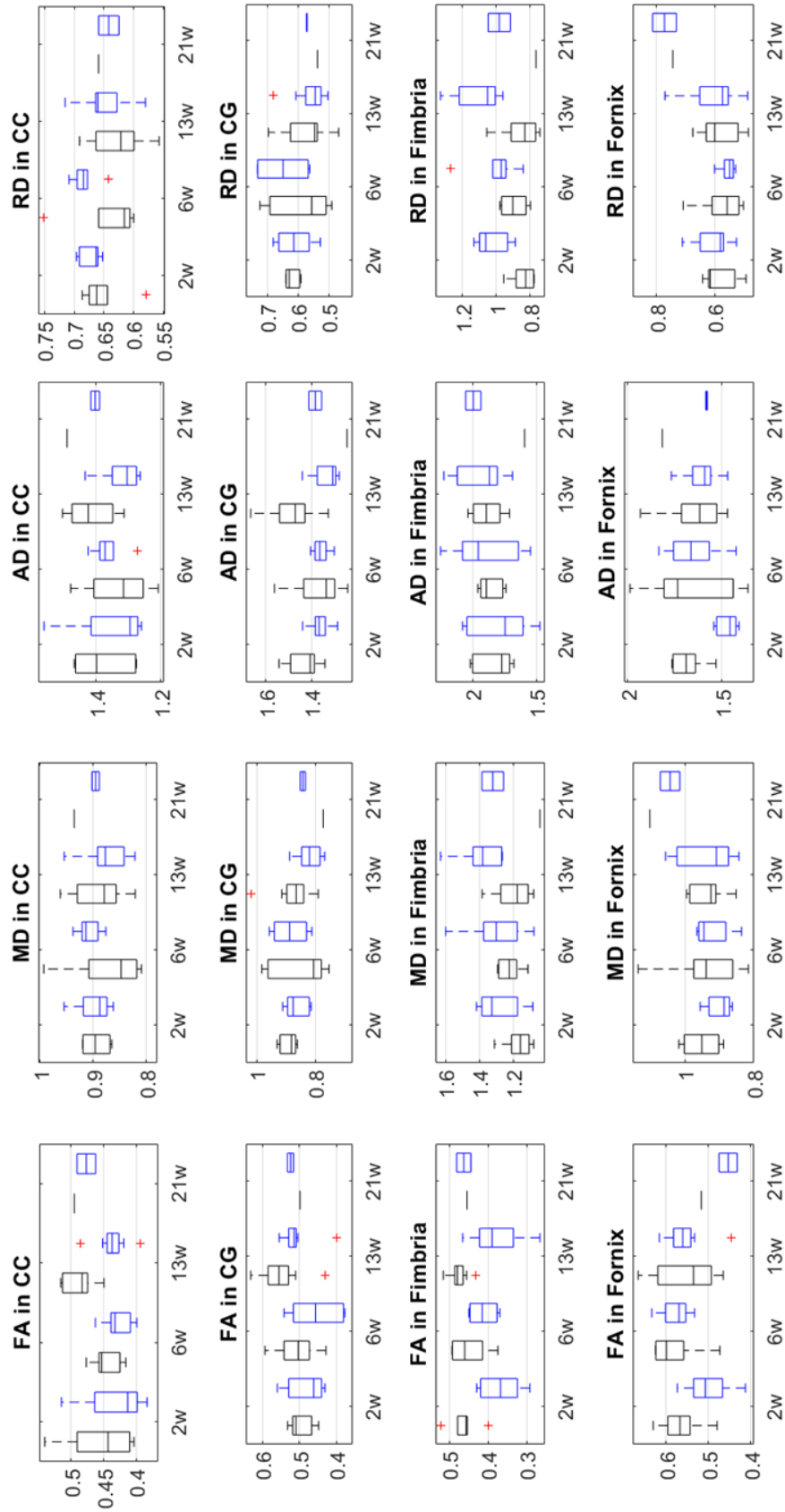


Figure 8.1: Boxplots of the metrics derived from DTI (columns) averaged by study groups and time points in each ROI (row). Significant differences between and within study groups are shown in the Table 8.1 and Table 8.2. Fundamental differences are shown in the Section 4.2.1.

CTL STZ

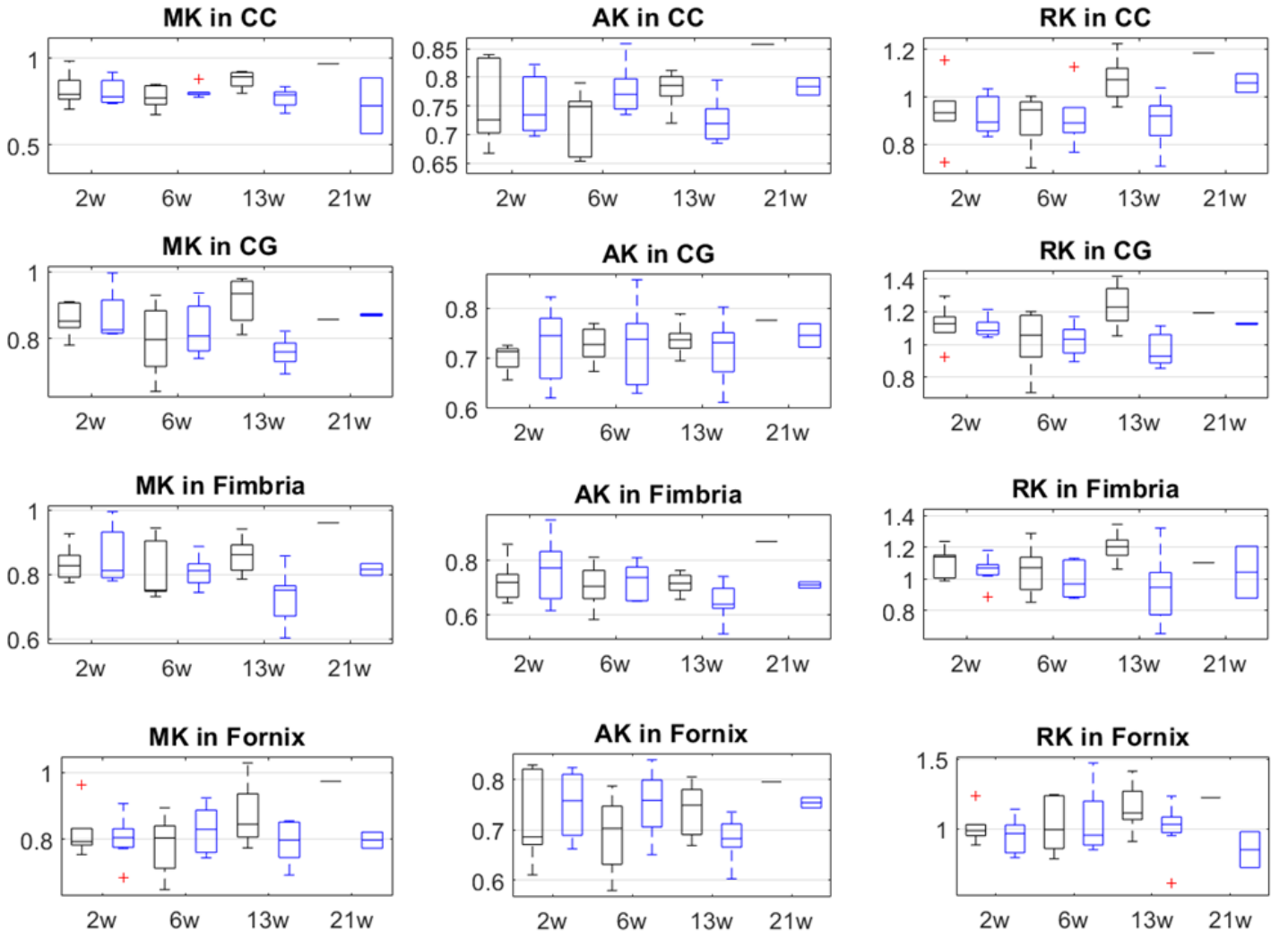


Figure 8.2: Boxplots of the metrics derived from DKI (columns) averaged by study groups and time points in each ROI (row). Significant differences between and within study groups are shown in the Table 8.1 and Table 8.2. Fundamental differences are shown in the Section 4.2.1.

Differences between STZ and CTL groups at each time point in tensors metrics			
Time point	ROI	Tensors metrics	p-value
2w	Fimbria	FA	0.0051
		RD	0.0023
	Fornix	AD	0.0003
13w	CC	FA	0.0005
		AD	0.0096
		MK	0.0005
		AK	0.0028
		RK	0.0024
		AD	0.0017
	CG	MK	2.5540e-05
		RK	0.0002
		FA	0.0008
	Fimbria	MD	0.0058
		RD	0.0006
		MK	0.0013
		AK	0.0224
		RK	0.0048
	Fornix	MK	0.0489
		AK	0.0182

Table 8.1: Significant differences ($p < 0.05$) between study groups in metrics derived from DTI and DKI in each ROI and at each time point.

Differences within each group over time in tensors metrics			
Study group	ROI	Tensors metrics	p-value
STZ	CG	MD	0.0491
		MK	0.0087
		RK	0.0273
	Fimbria	MK	0.0086
	Fornix	FA	0.0211
		AD	0.0115
		AK	0.0385
CTL	CC	MK	0.0440
		RK	0.0278
	CG	MK	0.0320
		RK	0.0402

Table 8.2: Significant differences ($p < 0.05$) over time in metrics derived from DTI and DKI in each ROI and within each study group.

CTL STZ

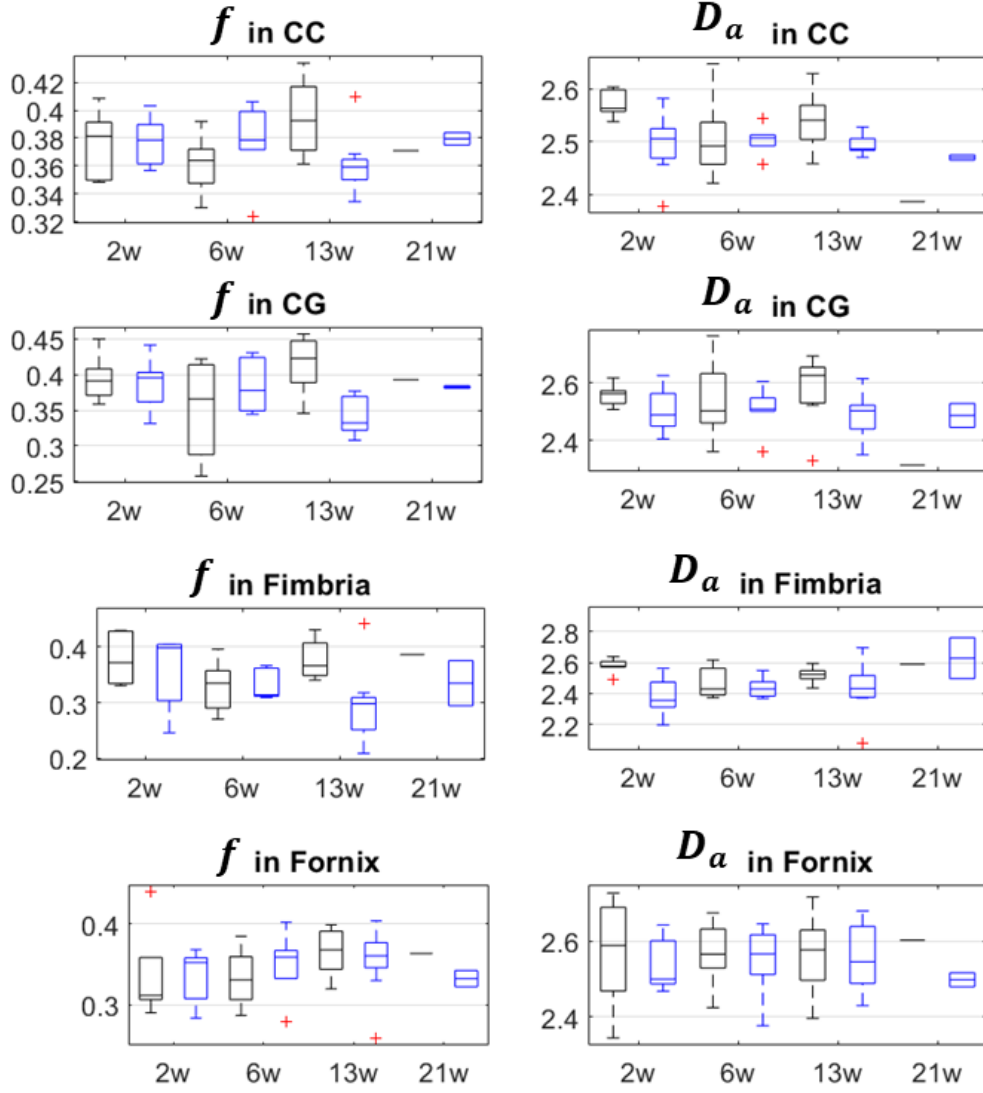


Figure 8.3: Boxplots of two metrics derived from the model (columns) averaged by study groups and time points in each ROI (row). Significant differences between and within study groups are shown in the Table 8.3 and Table 8.4. Fundamental differences are shown in the Section 4.2.2.

CTL STZ

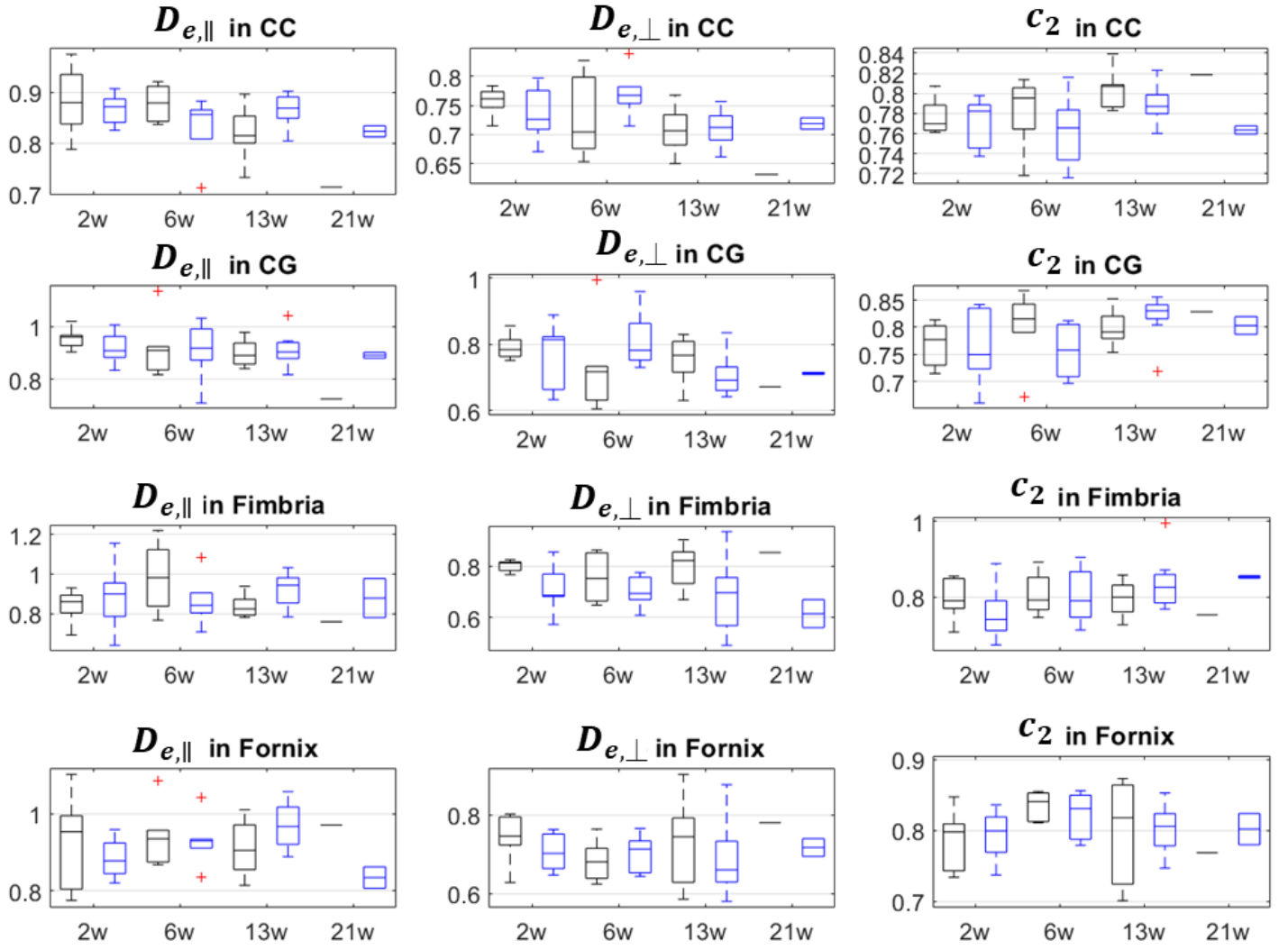


Figure 8.4: Boxplots of remaining three metrics derived from the model (columns) averaged by study groups and time points in each ROI (row). Significant differences between and within study groups are shown in the Table 8.3 and Table 8.4. Fundamental differences are shown in the Section 4.2.2.

Differences between STZ and CTL groups at each time point in model metrics			
Time point	ROI	Model metrics	p-value
2w	CC	D_a	0.0224
	Fimbria	D_a	0.0043
		$D_{e,\perp}$	0.0387
13w	CC	f	0.0109
		D_a	0.0270
		$D_{e,\parallel}$	0.0349
	CG	f	0.0004
	Fimbria	f	0.0103
		$D_{e,\parallel}$	0.0319

Table 8.3: Significant differences ($p < 0.05$) between study groups in metrics derived from the model in each ROI and at each time point.

Differences within each group over time in model metrics			
Study group	ROI	Model metrics	p-value
STZ	CC	$D_{e,\perp}$	0.0273
	CG	f	0.0233
	Fornix	$D_{e,\parallel}$	0.0252
CTL	Fimbria	D_a	0.0383

Table 8.4: Significant differences ($p < 0.05$) over time in metrics derived from the model in each ROI and within each study group.

8.2. Appendix B

In the course of this project, the work developed was published and presented at multiple occasions. A chronological list of conference abstracts is here described with brief synopsis of each.

[1] 27th Annual Meeting and Exhibition – ISMRM, 2019, Montreal, Canada

Title: Longitudinal characterization of white matter degeneration in a rat model of brain glucose metabolism and sporadic Alzheimer's disease

Date of submission: November 2018

Authors: **Catarina T. Pereira**¹, Ting Yin², Yujian Diao², Analina R. Silva², Ileana O. Jelescu²

¹Faculdade de Ciências da Universidade de Lisboa, Portugal; ²Centre d'Imagerie Biomédicale, École Polytechnique Fédérale de Lausanne, Switzerland

Presentation: Accepted for a digital-poster presentation and presented by Ting Yin in May 2019

Synopsis: Impaired brain glucose consumption is a possible trigger of Alzheimer's disease (AD). Animal models can help characterize each contributor to the cascade independently. Here we use the intracerebroventricular-streptozotocin rat model of AD in a first-time longitudinal study of white matter degeneration using diffusion MRI. Diffusion and kurtosis tensor metrics reveal alterations in the cingulum, fimbria and fornix. The two-compartment WMTI-Watson biophysical model further characterizes the cingulum damage as axonal injury and loss - consistent with previous histopathological studies. White matter degeneration induced by brain glucose metabolism disruption can bring further insight into the role of this mechanism in AD.

[2] 27th Annual Meeting and Exhibition – ISMRM, 2019, Montreal, Canada

Date of submission: November 2018

Title: Spatio-temporal alterations in functional connectivity in a rat model of brain glucose metabolism disruption and sporadic Alzheimer's disease

Authors: Yujian Diao¹, **Catarina T. Pereira**², Ting Yin¹, Rolf Gruetter¹, Analina R. Silva¹, Ileana O. Jelescu¹

¹Centre d'Imagerie Biomédicale, École Polytechnique Fédérale de Lausanne, Switzerland; ²Faculdade de Ciências da Universidade de Lisboa, Portugal

Presentation: Accepted for a digital-poster presentation and presented by Yujian Diao in May 2019

Synopsis: Impaired brain glucose consumption is a possible trigger of Alzheimer's disease (AD). Animal models can help characterize each contributor to the cascade independently. Here we perform a first-time longitudinal study of brain connectivity in the intracerebroventricular-streptozotocin rat model of AD. We report altered brain circuitry as early as two weeks in regions notoriously affected by AD (cingulate cortices, posterior parietal cortex and hippocampus), and widespread gradual breakdown of connectivity with time. The changes in brain connectivity induced by glucose metabolism disruption can bring further insight into the role of this mechanism in AD.

[3] 25th OHBM Annual Meeting, 2019, Rome, Italy

Date of submission: December 2018

Title: Longitudinal changes in microstructure and functional connectivity in a rat model of Alzheimer

Authors: **Catarina T. Pereira**¹, Yujian Diao², Ting Yin², Analina R. Silva², Rolf Gruetter², Ileana O. Jelescu²

¹Faculdade de Ciências da Universidade de Lisboa, Portugal; ²Centre d'Imagerie Biomédicale, École Polytechnique Fédérale de Lausanne, Switzerland

Presentation: Accepted for a paper-poster presentation and presented by myself in June 2019

Synopsis: Impaired brain glucose consumption is a possible trigger of Alzheimer's disease (AD). Animal models can help characterize each contributor to the cascade independently. Here we use the intracerebroventricular-streptozotocin rat model of AD in a first-time longitudinal study of white matter microstructure and brain connectivity using diffusion MRI and resting-state functional MRI, respectively. Diffusion and kurtosis tensor metrics reveal alterations in the cingulum, fimbria and fornix. The two-compartment WMTI-Watson biophysical model further characterizes the cingulum damage as axonal injury and loss - consistent with previous histopathological studies. We further report altered brain circuitry as early as two weeks in regions notoriously affected by AD (cingulate cortices, posterior parietal cortex and hippocampus), and widespread gradual breakdown of connectivity with time. These biomarkers can bring additional insight into the role of these mechanisms in AD.